CHAPTER IX

HIGH-ENERGY NUCLEAR PHENOMENA

1. INTRODUCTION

In this chapter we consider reactions induced by projectiles whose energy per particle is in the GeV or sub-GeV range. The projectiles are, for the most part, electrons and protons, although there will be some discussion of relativistic heavy-ion projectiles. The phenomena discussed includes elastic, inelastic, and quasi-elastic scattering and, in the case of relativistic heavy ions, fragmentation. The production of bosons with various values of hypercharge and their interaction with nuclei will be left to Chapter X. These areas of physics, those in this and the next chapter, are referred to as *medium-energy nuclear physics.*

High energy translates into high momentum and short wavelength. Because of the short wavelength and relatively weak interaction of the electrons, high-energy electron accelerators are effectively electron microscopes, studying the nucleus and, at sufficiently high energy, the structure of the individual nucleons. As we shall describe, through the use of electron scattering, we are able to obtain a detailed understanding of the spatial distribution of charge and current in the target nucleus. It should be emphasized that such results can be obtained only because the properties of the probe, the electron, and its interaction with the electromagnetic field in this case generated by the target nucleus as given by quantum electrodynamics are so very well known.

In more detail, the matrix elements of nuclear charge and current can be directly related to the nuclear multipole moments. These are of two types, the Coulomb and the transverse electric and magnetic. The latter also occur in the description of photon emission [see deShalit and Feshbach (74, p. 689)] with identical selection rules (deShalit and Feshbach (74, p. 670)]. The selection rules

associated with the Coulomb multipole moments are the same as those for the transverse electric multipoles. The information obtained from electron scattering is much richer than that which can be extracted from photon-induced transitions. In the latter case, there is only one independent variable, the energy transfer ω in units of $\hbar$, whereas in electron scattering there are two, the energy transfer and the momentum transfer $\mathbf{q}$ in units of $\hbar$. Of course, momentum transfer does occur in the case of photon reactions. But its magnitude is ω/c. In electron scattering the momentum transfer and the energy transfer are not coupled; q can differ from ω/c by several orders of magnitude. Electron scattering thus yields the q dependence of both the transverse and Coulomb multipole moments, and by Fourier inversion their spatial dependence. One is thus able to map the charge and current distribution experimentally and compare them with the predictions of theoretical models.

In particular, the transverse moments that measure the nuclear current distribution are, according to the shell model, sensitive to the wave functions of the valence neutrons and protons. This follows from the fact that the net current generated by the core is zero. On the other hand, note that the Coulomb moments are sensitive only to the proton distribution. Fortunately, by choosing appropriate kinematic conditions it is possible to measure separately the transverse and Coulomb moments.

These results assume that the nuclear charge and current operators are one-body operators, given by (VII.2.1)–(VII.2.4) in deShalit and Feshbach (74). This is an approximation, as there are two-body terms as well, such as those given by exchange currents and exchange charge [see Section VIII.3 in deShalit and Feshbach (74)]. Before claiming the observation of exchange currents, one must use sufficiently accurate nuclear wave functions in the evaluation of the nuclear matrix elements. For example, the independent particle description must be supplemented by configuration interactions [Chapter V in deShalit and Feshbach (74)] and by correlations (Chapter III and VII of the same reference). In some cases, those in which the spin–isospin ($\sigma\tau$) transitions dominate, the excitation of the nucleons to Δ's may be important.

Because of the high energy, the electron can excite states in the continuum, such as isobar analog states and the giant resonances. Because of the associated high momentum, one can study multipoles of high order and one can form stretched nuclear states. Because of their high energy the electrons can eject one or more nucleons from the target. The underlying process, quasi-elastic scattering, is the collision between the electron and nucleon in the nucleus. Its cross section peaks at an energy transfer ω for large enough q at $q^2/2m^* + \varepsilon$, where m^* is the nucleon's effective mass and ε is its binding energy. In a Fermi gas model the width of the quasi-elastic peak is $k_F q/m^*$ (see I.3.9). Removing a nucleon in an $(e, e'p)$ or (γ, p) experiment may permit a determination of the momentum distribution of a single-particle state and the lifetime of a deep one-hole state. At still higher energies the electron can excite the individual nucleon, forming the nucleon isobar Δ, which can decay by emitting a pion. Direct pion production without the intermediary of a Δ will also occur. These

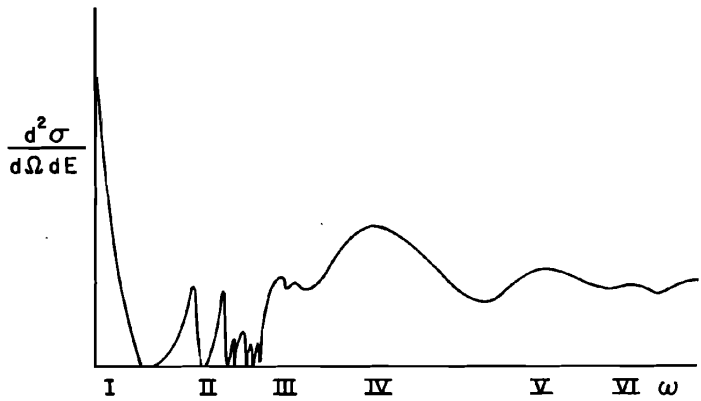

FIG. 1.1. Schematic electron energy loss spectrum. Region I, elastic scattering; II, excitation of discrete levels; III, excitation of giant resonances; IV, quasi-elastic scattering; V, pion production and Δ formation; VI, N^* formation.

various possibilities are shown in Fig. 1.1, which schematically pictures the electron spectrum at a given q.

When an electron is scattered by a nucleus, there is a high probability that it will also emit a photon. As a consequence of this energy loss, the elastic and inelastic scattering cross sections will exhibit a tail on the low-energy side, usually referred to as a radiative tail. The observed cross section will, in addition, depend on the energy resolution, ΔE, of the detector since it will count electrons that have radiated photons whose energy is less than ΔE. These effects can be calculated with great accuracy [Schwinger (49b)] and the experimental cross section unfolded to yield the radiation-free cross section. It is this corrected cross section that is usually quoted in the experimental papers. Figure 1.1 is qualitatively correct only in this sense. Otherwise, the gaps between levels as shown in Fig. 1.1 would be partially filled in. An experimental example is shown in Fig. 1.2. The radiative corrections are thoroughly described by Überall (71).

As this is being written, electron scattering studies are entering a new era in which it is anticipated important advances in our understanding of nuclei will be obtained. Up to recently, the electron accelerators had a low duty cycle. As a consequence, some experiments were difficult. The new CW ($\sim 100\%$ duty cycle) accelerators, some already available and others under construction, will make greatly improved coincidence measurements possible as well as make available tagged and thereby monochromatic γ-ray beams. In addition, there is the prospect of polarized electrons and polarized internal jet nuclear targets. With coincidence experiments one can reduce the radiative tail background enormously (see Fig. 1.3).

With these new tools it becomes possible experimentally to measure the individual multipole moment amplitudes separately. With the low-duty-cycle accelerators, a complicated model-dependent analysis is necessary. It will also

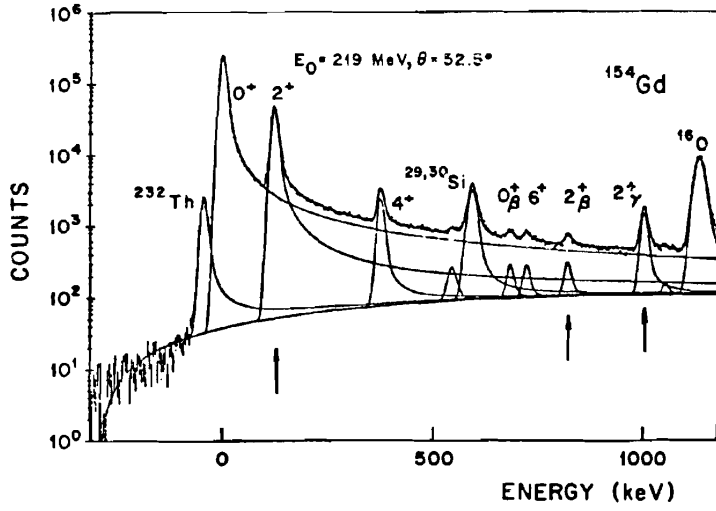

FIG. 1.2. Sample electron excitation spectrum for ^{154}Gd. The incident electron energy is 219 MeV. The scattered electron is observed at 52.5°. [From Bates Linear Accelerator proposal (84).]

become possible to observe the particle emission from giant resonances and make improved measurements on deep one-hole and stretched states.

The experimental studies undertaken with high-energy protons are very similar in character to those described above using electrons. Elastic and inelastic scattering, including excitation of discrete levels, of the giant resonances of one-hole and stretched states, Δ and pion production have been observed. Polarized beams have also been used. There is, of course, one very great difference: namely, the interactions in the proton case are "strong" and not completely known. One must rely on multipole scattering theory (Chapter II), in which proton–nucleus interaction is approximated by an optical potential V. In its simplest first-order form, V in momentum space is given by

$$V(\mathbf{k}, \mathbf{k}') = (A-1)\hat{\rho}(-\mathbf{q})\hat{t}_E(\mathbf{q}) \tag{1.1}$$

where $\hat{\rho}$ is the nucleon density operator and $\hat{t}_E(\mathbf{q})$ is the transition matrix operator for nucleon–nucleon scattering. The vector $\mathbf{q}$ is the momentum transfer ($\mathbf{k}$, initial momentum, $\mathbf{k}'$ final momentum). The function t_E is evaluated at the center-of-mass energy of the nucleon–nucleus system with due regard for the transformation from the nucleon–nucleon system (see II.7). The discussion in this chapter will rely on (1.1).

By taking matrix elements of V, the appropriate potentials for various experimental situations can be obtained. For elastic scattering

$$V_{00} \equiv \langle 0|V|0\rangle = (A-1)\langle 0|\hat{\rho}\hat{t}|0\rangle \tag{1.2}$$

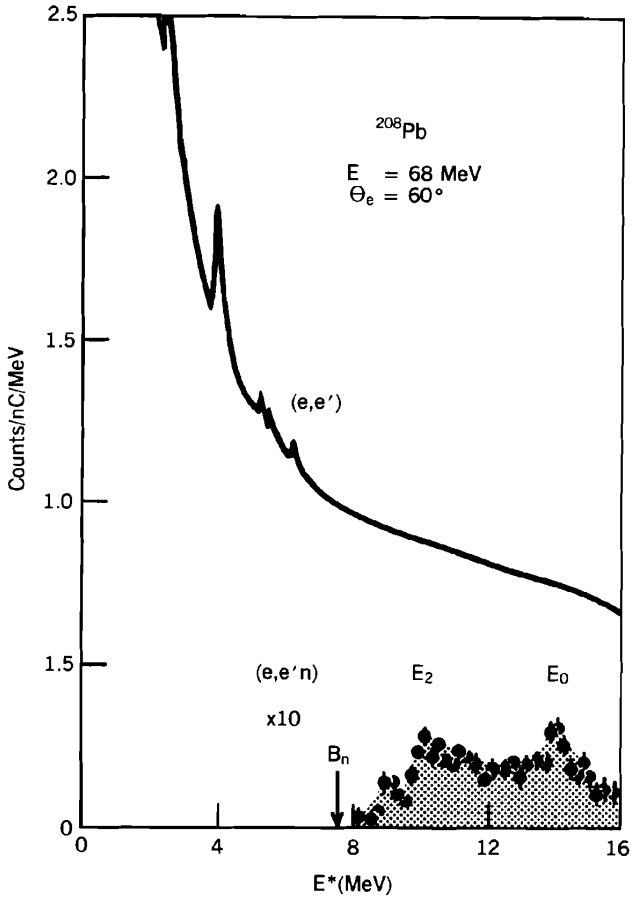

FIG. 1.3. Single arm and coincident $(e,e'n)$ spectra from ^{208}Pb. The coincidence condition removes the radiative tail, revealing the excitation of giant resonances. [From Frois and Papanicolas (87).]

where $|0\rangle$ is the ground-state nuclear wave function. For inelastic scattering to a level $|f\rangle$, the transition potential is

$$V_{f0} = (A-1)\langle f|\hat{\rho}\hat{t}|0\rangle \tag{1.3}$$

Since $\hat{t}$ depends on the spin and isospin operators, V_{00} and V_{f0} will depend on various spin and isospin components of the elastic and transition density, respectively. These combinations differ from the electron case, so that nucleon–nucleus scattering provides information which complements that obtained from electron scattering.

Equation (1.1) is a first approximation to V. Higher-order approximations

involving higher powers of $\hat{t}$ have been obtained. These depend on correlation functions.

2. ELECTRON SCATTERING

Let us begin with some kinematics. The incident electron with four momentum $k_\mu(\mathbf{k}, E)$ is scattered through an angle ϑ. We shall work in units with $\hbar = c = 1$. Its final momentum is $k'_\mu(\mathbf{k}', E')$. The three momentum transfer is $\mathbf{q}$:

$$\mathbf{q} = \mathbf{k} - \mathbf{k}'$$

while the energy transfer is ω:

$$\omega = E - E'$$

The magnitude of $\mathbf{q}$ is

$$q^2 = (k^2 - 2kk' \cos\vartheta + k'^2) \xrightarrow[k=k']{} 4k^2 \sin^2 \tfrac{1}{2}\vartheta \tag{2.1}$$

Since the electron energy will be very much greater than its rest mass, $k = E$ and $k' = E'$. In this limit

$$q^2 = \omega^2 + 4EE' \sin^2 \tfrac{1}{2}\vartheta \tag{2.2a}$$

and

$$q_\mu^2 = q^2 - \omega^2 = 4EE' \sin^2 \tfrac{1}{2}\vartheta \geqslant 0 \tag{2.2b}$$

For elastic electron scattering, the target nucleus will recoil with a momentum q, so that

$$\omega = (q^2 + M^2)^{1/2} - M \tag{2.3}$$

where M is the mass of the target (mA). Transposing M to the left-hand side of this equation and squaring yields

$$\omega = \frac{1}{2M} q_\mu^2 \tag{2.4}$$

In (2.2b) replace E' by $E - \omega = E - (1/2M)q_\mu^2$. Solving for q_μ^2 yields

$$q_\mu^2 = \frac{1}{f_{\text{rec}}}(4E^2 \sin^2 \tfrac{1}{2}\vartheta) \tag{2.5}$$

where

$$f_{\text{rec}} = 1 + \frac{2E}{M} \sin^2 \tfrac{1}{2}\vartheta \tag{2.6}$$

From (2.3)

$$q^2 = (2\omega M)\left(1 + \frac{\omega}{2M}\right) \tag{2.7}$$

and finally from (2.4) and (2.6), we obtain

$$E' = \frac{E}{f_{\text{rec}}} \tag{2.8}$$

In the foreward direction ($\vartheta = 0$), E' equals E.

A. Elastic Scattering from Spin-Zero Nuclei

The modern era in electron scattering was initiated by R. Hofstader by his studies of the elastic scattering of electrons by spin-zero nuclei. This is perhaps the most highly studied process involving electrons. Very great accuracy has been achieved. To start with , we assume that the nucleus is describable by a static (time-independent) charge distribution $\rho(\mathbf{r})$. The resulting electrostatic potential, ϕ, is the solution of the Poisson equation:

$$\nabla^2 \phi = -4\pi\rho \tag{2.9}$$

In momentum space

$$\phi = \frac{4\pi\rho(\mathbf{q})}{q^2} \tag{2.10}$$

where

$$\rho(\mathbf{q}) = \int e^{i\mathbf{q}\cdot\mathbf{r}} \rho(\mathbf{r})\, d\mathbf{r} \tag{2.11}$$

We shall discuss the Born approximation to the scattering produced by ϕ. It is of course necessary to employ the relativistic Dirac equation:[‡]

$$[\gamma_\mu(p_\mu - eA_\mu) - im]\psi = 0 \tag{2.12}$$

[‡]In the rest of this chapter $\hbar$ and c will be placed equal to unity. The four-vector p_μ has components $(\mathbf{p}, E)$, where $\mathbf{p}$ is the momentum and E is the energy. Similarly, $\mathbf{A}$ is the vector potential, $A_4 = i\phi$. Finally

$$\gamma = \rho_2 \boldsymbol{\sigma} \qquad \text{where } \rho_2 = \begin{pmatrix} 0 & -i \\ i & 0 \end{pmatrix}$$

The summation convention is used in this equation. For the situation under study, (2.1) becomes

$$(\gamma_\mu p_\mu - im)\psi = ie\gamma_4\phi\psi$$

Multiplying by $(\gamma_\mu p_\mu + im)$, we obtain

$$(p^2 - E^2 + m^2)\psi = ie(\gamma_\mu p_\mu + im)\gamma_4\phi\psi$$

or

$$(\nabla^2 + k^2)\psi = -ie(\gamma_\mu p_\mu + im)\gamma_4\phi\psi \tag{2.12'}$$

so that the scattering amplitude operator, $\hat{f}$, is

$$\hat{f} = \frac{ie}{4\pi}\int e^{-i\mathbf{k}'\cdot\mathbf{r}}(\gamma_\mu p_\mu + im)\gamma_4\phi\psi_i^{(+)}\,d\mathbf{r} \tag{2.13}$$

Or integrating by parts, we have

$$\hat{f} = \frac{ie}{4\pi}(\gamma_\mu k'_\mu + im)\gamma_4\int e^{-i\mathbf{k}'\cdot\mathbf{r}}\phi\psi_i^{(+)}\,d\mathbf{r} \tag{2.13'}$$

where $k'_4 = iE$. In the Born approximation

$$\psi_i \longrightarrow e^{i\mathbf{k}\cdot\mathbf{r}}u_i \tag{2.14}$$

so that

$$\boldsymbol{\gamma} = \begin{pmatrix} 0 & -i\boldsymbol{\sigma} \\ i\boldsymbol{\sigma} & 0 \end{pmatrix} \qquad \boldsymbol{\alpha} = \begin{pmatrix} 0 & \boldsymbol{\sigma} \\ \boldsymbol{\sigma} & 0 \end{pmatrix}$$

In this last equation $\boldsymbol{\sigma}$ are the two-row/two-column Pauli spin matrices. The matrix γ_4 is

$$\gamma_4 = \begin{pmatrix} 1 & 0 \\ 0 & -1 \end{pmatrix}$$

The γ's satisfy

$$\gamma_\mu\gamma_\nu + \gamma_\nu\gamma_\mu = 2\delta_{\mu\nu}$$

The trace of products of the γ's are [see (IX.11.22) in deShalit and Feshbach (74)]

$$\mathrm{tr}1 = 4$$

$$\mathrm{tr}\gamma_\mu\gamma_\nu = 4\delta_{\mu\nu}$$

$$\mathrm{tr}(\gamma_\mu\gamma_\nu\gamma_\lambda\gamma_\omega) = 4[\delta_{\mu\nu}\delta_{\lambda\omega} - \delta_{\mu\lambda}\delta_{\nu\omega} + \delta_{\mu\omega}\delta_{\nu\lambda}]$$

The trace of an odd number of γ's is zero. For more details, see the appendix to Chapter IX and p. 825 et seq. in deShalit and Feshbach (74).

where u_i is a four-element columnar matrix given by (5.8) and (5.9) of the Appendix to Chapter IX in deShalit and Feshbach (74). These are *positive energy* solutions of the field-free Dirac equation with spin up and spin down, respectively. Introducing (2.14) into (2.13′), one obtains

$$\hat{f} = \frac{ie}{4\pi}(\gamma_\mu k'_\mu + im)\gamma_4 u_i \phi(\mathbf{q}) \tag{2.15}$$

Employing (2.10) for $\phi(\mathbf{q})$, $\hat{f}$ becomes

$$\hat{f} = \frac{ie}{q^2}(\gamma_\mu k'_\mu + im)\gamma_4 u_i \rho(\mathbf{q}) \tag{2.16}$$

The amplitude is thus linearly related to the Fourier transform of the charge density. The scattering amplitude to a given final state is

$$f_{fi} = \frac{ie\rho(\mathbf{q})}{q^2}\langle u_f(\gamma_\mu k'_\mu + im)\gamma_4 u_i\rangle$$

To obtain the cross section, one must square the magnitude of f_{fi}, sum over all final spin states, and average over the initial ones:

$$\sigma = \tfrac{1}{2}\sum_{f,i}|f_{fi}|^2 \tag{2.17}$$

One can reduce the calculation of σ to the evaluation of a trace by using the projection operator P on the positive energy. This operator has been derived in deShalit and Feshbach (74, p. 825, et seq.). It is

$$P = \frac{1}{2iE}(\gamma_\mu k_\mu + im)\gamma_4 \tag{2.18}$$

so that (2.17) becomes

$$\frac{d\sigma}{d\Omega} = \tfrac{1}{2}\mathrm{tr}(\hat{f}^\dagger P_f \hat{f} P_i) \tag{2.19}$$

where the subscript i, for example, indicates that in (2.18), k_μ equals the incident momentum and energy. Inserting $\hat{f}$ from (2.16), (2.19) becomes

$$\frac{d\sigma}{d\Omega} = -\frac{e^2|\rho(\mathbf{q})|^2}{q^4}\frac{1}{8E^2}\mathrm{tr}[\gamma_4(\gamma_\mu k'^*_\mu - im)(\gamma_\nu k'_\nu + im)\gamma_4(\gamma_\lambda k'_\lambda + im)\gamma_4(\gamma_\omega k_\omega + im)\gamma_4] \tag{2.20}$$

The γ_4's at the beginning and end of this expression cancel. The trace can then

be readily evaluated using the results in the footnote on page 686. One obtains

$$\frac{d\sigma}{d\Omega} = \frac{2e^2|\rho(\mathbf{q})|^2}{q^4}(\mathbf{k}\cdot\mathbf{k}' + E^2 + m^2) = |e\rho(\mathbf{q})|^2 \frac{1 - \beta^2 \sin^2 \tfrac{1}{2}\vartheta}{(2\beta^2 E \sin^2 \tfrac{1}{2}\vartheta)^2} \tag{2.21}$$

where $\beta = v/c$. The charge density ρ_0 of a zero-radius-point nucleus is

$$\rho_0(\mathbf{r}) = Ze\delta(\mathbf{r})$$

so that

$$\rho_0(\mathbf{q}) = Ze$$

The resulting cross section divided by Z^2 is referred to as the *Mott cross section* σ_M:

$$Z^2\sigma_M = (1 - \beta^2 \sin^2 \tfrac{1}{2}\vartheta)\frac{(Ze^2)^2}{(2\beta^2 E \sin^2 \tfrac{1}{2}\vartheta)^2} \tag{2.22}$$

$$\xrightarrow[\beta \to 1]{} \frac{(Ze^2)^2 \cos^2 \tfrac{1}{2}\vartheta}{(2E \sin^2 \tfrac{1}{2}\vartheta)^2} \tag{2.23}$$

These results hold in the center-of-mass system or if the target mass M is infinite. In the laboratory frame, the recoil of the target must be taken into account. Repeating the calculation above in the laboratory frame leads to (2.21), which, however, must be multiplied by k'/k or ε'/ε in the zero-electron-mass limit. Then using (2.8), one obtains

$$\frac{d\sigma}{d\Omega} = \frac{1}{f_{\text{rec}}}\sigma_M|\rho(\mathbf{q})|^2 \tag{2.24}$$

This Born approximation result is valid at best for light nuclei. By a measurement of elastic electron scattering, one can in principle determine the *charge* density distribution. But there are several corrections. The most obvious is the effect of the nuclear Coulomb field on the electron wave functions. Therefore, the plane wave approximation for the electron wave functions used above is incorrect, especially for the large Z nuclei. Second, the calculation above is incomplete since it includes only the elastic scattering produced by the nuclear charge distribution. Scattering produced by the nuclear currents and magnetization are not accounted for. Finally, there are the effects of virtual inelastic scattering on the elastic scattering. These are referred to as *dispersion corrections.*

B. Coulomb Scattering

The wave functions for an electron moving in the Coulomb field of a point nucleus have been described in deShalit and Feshbach (74, pp. 915–916). As in

that review, let the Dirac wave function ψ be a two-element matrix, each element of which is a spinor

$$\psi = \begin{pmatrix} u \\ v \end{pmatrix} \tag{2.25}$$

The wave functions u and v for the state with a given angular momentum, j, are products of a radial function and a function giving the spin and angle dependence:

$$u(j,l) = \frac{G(r)}{r}\mathcal{Y}_m(j,l) \tag{2.26a}$$

$$v(j,l) = \frac{f(r)}{r}(-i\boldsymbol{\sigma}\cdot\hat{\mathbf{r}})\mathcal{Y}_m(j,l) \tag{2.26b}$$

where

$$\mathcal{Y}_m(j,l) = \sum(\tfrac{1}{2}m_s, lm_l|\,jm)\chi_{1/2}(m_s)\mathcal{Y}_{lm_l} \tag{2.27}$$

The spin wave function is $\chi_{1/2}$, while $\mathcal{Y}_{lm_l} = i^l Y_{lm}$, where Y_{lm} is a spherical harmonic.

The equations satisfied by f and G for an arbitrary radial potential $V(r)$ are

$$(E - m - V)G + \frac{df}{dr} - \kappa\frac{f}{r} = 0 \tag{2.28a}$$

$$-(E + m - V)f + \frac{dG}{dr} + \kappa\frac{G}{r} = 0 \tag{2.28b}$$

where

$$\kappa = -[1 + \boldsymbol{\sigma}\cdot\mathbf{L}] = \begin{cases} (j+\frac{1}{2}), & l = j+\frac{1}{2} \\ -(j+\frac{1}{2}), & l = j-\frac{1}{2} \end{cases} \quad \text{or} \quad \kappa = \begin{cases} l \\ -(l+1) \end{cases}$$

The exact solutions are given in deShalit and Feshbach (74, p. 916) in terms of the confluent hypergeometric function. We quote here only the behavior of G and f as $r \to 0$ and $r \to \infty$.

$$G(r \to 0) \to (\varepsilon + 1)^{1/2} N_s \cos\phi_s (2kr)^s \tag{2.29a}$$

$$f(r \to 0) \to (\varepsilon - 1)^{1/2} N_s \sin\phi_s (2kr)^s \tag{2.29b}$$

$$G(r \to \infty) \to (\varepsilon + 1)^{1/2} \cos\left[kr + \eta \log 2kr - \frac{\pi}{2}(l+1) + \delta_\kappa^{(c)}\right] \tag{2.30a}$$

$$f(r\to\infty)\to -(\varepsilon-1)^{1/2}\sin\left[kr+\eta\log 2kr-\frac{\pi}{2}(l+1)+\delta_\kappa^{(c)}\right] \tag{2.30b}$$

where

$$s=\sqrt{(j+\tfrac{1}{2})^2-(Ze^2)^2}\qquad \eta=Ze^2\frac{E}{k}\qquad \varepsilon=\frac{E}{m}$$

$$e^{2i\phi_s}=-\frac{\kappa-i(Ze^2)m/k}{s+i\eta}\qquad N_s=\frac{|\Gamma(s+1+i\eta)|}{\Gamma(2s+1)e^{-\eta\pi/2}} \tag{2.31}$$

$$e^{2i\delta_\kappa^{(c)}}=-\frac{\kappa+iZe^2m/k}{s-i\eta}\frac{\Gamma(s+1-i\eta)}{\Gamma(s+1+i\eta)}e^{\pi/2\,i(l+1-s)}$$

Using these results, Mott (29,32) expressed the cross section for the scattering of an electron by a nucleus in terms of two conditionally convergent infinite series. To first order in $Ze^2\beta$, these series can be summed [McKinley and Feshbach (48)] to yield:

$$\sigma=\left(\frac{Ze^2}{2\beta^2E\sin\frac{1}{2}\vartheta}\right)^2\left[1-\beta^2\sin^2\frac{\vartheta}{2}+\pi Ze^2\beta\sin\frac{\vartheta}{2}\left(1-\sin\frac{\vartheta}{2}\right)\right] \tag{2.32}$$

To obtain the results for positron scattering, replace Z by $(-Z)$. This result is useful for sufficiently light nuclei. For larger values of Z, numerical methods are required. Tables are given by McKinley and Feshbach (48), Feshbach (52), and Curr (55). Yennie et al. (55) improve the convergence by multiplying the Mott series by $(1-\cos\vartheta)^3$ and employing the Legendre function recurrence relation to reorder the series.

C. Effect of Finite Size of the Nucleus

The results above are obtained by using $V=-Ze^2/r$ in (2.28). Taking the charge structure of the nucleus into account requires replacing it by the solution of the Poisson equation (2.10). For spin-zero nuclei the resulting V is a function of r only. For $r>R$ (the nuclear radius) V will approach the point Coulomb value. The solutions of (2.28) are obtained in the usual fashion, that is, by joining the solutions of (2.28) to the Coulomb wave functions for $r>R$. Asymptotically, this means replacing $\delta_\kappa^{(c)}$ in (2.30) by δ_κ. Note also that the singularity exhibited by the Coulomb wave functions at $r=0$ for $j=\frac{1}{2}$ [see (2.29)] disappears when the finite size of the nucleus is taken into account. The wave function now approaches r^{l+1}. The scattering amplitude is given by Acheson (51):

$$\hat{f}=f(\vartheta)+ig(\vartheta)\boldsymbol{\sigma}\cdot\mathbf{n} \tag{2.33}$$

where

$$\mathbf{n}=\hat{k}\times\hat{k}'$$

and

$$f(\vartheta) = \frac{1}{2ik} \sum_{\kappa > 0} \kappa [e^{2i\delta_\kappa} P_\kappa(\cos\vartheta) + e^{2i\delta_{-\kappa}} P_{\kappa-1}(\cos\vartheta)] \tag{2.34a}$$

and

$$g(\vartheta) = -\frac{1}{2ik} \sum_{\kappa > 0} [e^{2i\delta_\kappa} P_\kappa^{(1)}(\cos\vartheta) - e^{-2i\delta_{-\kappa}} P_{\kappa-1}^{(1)}(\cos\vartheta)] \tag{2.34b}$$

where according to (2.28), κ equals l, and $-\kappa = -(l+1)$. The functions $P_\kappa^{(1)}(\cos\vartheta)$ are the associated Legendre functions

$$P_\kappa^{(1)}(x) = (1-x^2)^{1/2} \frac{d}{dx} P_\kappa(x)$$

The elastic cross section for an unpolarized incident electron beam averaged over the final spin is

$$\sigma = |f^2| + |g|^2 \tag{2.35}$$

The polarization produced by the scattering of an unpolarized beam is

$$\mathbf{P} = \frac{1}{\sigma} \mathrm{tr} \langle \hat{f}^\dagger \boldsymbol{\sigma} f \rangle = \frac{i(f^* g - g f^*)}{|f|^2 + |g|^2} \mathbf{n} \tag{2.36}$$

so that the polarization of the electrons is perpendicular to the scattering plane.

Simplifications do occur in the limit of $m/E \to 0$; that is, in the high-energy limit, (2.28) reduces to

$$(E - V)G + f' - \frac{\kappa f}{r} = 0$$

$$(E - V)f - G' - \frac{\kappa G}{r} = 0$$

For $\kappa = -l$,

$$(E - V)G_l + f_l' + \frac{l f_l}{r} = 0$$

$$(E - V)f_l - G_l' + \frac{l G_l}{r} = 0$$

For $\kappa = l$, we have

$$(E - V)G_{-l} + f_{-l}' - \frac{l f_{-l}}{r} = 0$$

$$(E - V)f_{-l} - G_{-l}' - \frac{l G_{-l}}{r} = 0$$

Comparing the (G_l, f_l) equations with those for (G_{-l}, f_{-l}), we see that these equations become identical if

$$G_{-l} = f_l$$
$$f_{-l} = -G_l \tag{2.37}$$

From the asymptotic forms, (2.30), with $\delta_\kappa^{(c)}$ replaced by δ_κ, it follows that [Feshbach (51)]

$$\delta_l = \delta_{-(l+1)}$$

or

$$\delta_\kappa = \delta_{-\kappa} \qquad \frac{m}{E} \to 0 \tag{2.38}$$

This result holds for the Coulomb phase shift (2.31), from which one finds that

$$e^{2i[\delta_{-\kappa}^{(c)} - \delta_\kappa^{(c)}]} \simeq 1 - \frac{Ze^2 m}{k\kappa} \tag{2.39}$$

For the energies of interest ($k \gg m$), the error is indeed small. Equation (2.38) is obviously computationally useful. Inserting (2.38) into (2.34*b*) and using

$$P'_\kappa - P'_{\kappa-1} = \kappa(P_\kappa + P_{\kappa-1}) \tan \tfrac{1}{2}\vartheta$$

we obtain

$$g(\vartheta) = (\tan \tfrac{1}{2}\vartheta) f(\vartheta)$$

so that

$$\sigma = \sec^2 \tfrac{1}{2}\vartheta |f(\vartheta)|^2 \tag{2.40}$$

and

$$\mathbf{P} \to 0 \tag{2.41}$$

Therefore, the polarization produced by the scattering tends to zero as the energy increases.

In the high-energy limit it is useful to obtain an eikonal approximation for the wave function. We return to (2.12′) to the Schrödinger equation from

$$(\nabla^2 + k^2)\psi = U\psi$$

where

$$U = -ie(\gamma_\mu p_\mu + im)\gamma_4 \phi \tag{2.42}$$

The eikonal solution to the Schrödinger equation has been given in Chapter II

[Eq. (II.5.7)]:

$$\psi = \exp\left\{i\left[kz + \int_{-\infty}^{z} dz'(\sqrt{k^2 - U} - k)\right]\right\}u$$

or

$$\simeq \left\{\exp i\left[kz - \frac{1}{2k}\int_{-\infty}^{z} U\, dz'\right]\right\}u \tag{2.43}$$

In this equation u is a spinor. Consistent with the eikonal approximation, we drop the m term in (2.42) and replace the operator p_u by k_u. This introduces a new condition for the validity of the results to be obtained below:

$$\frac{\nabla\phi}{k\phi} \ll 1 \tag{2.44}$$

This condition is very well satisfied for an extended nuclear charge density. Note that this last approximation need not be made. The analysis that follows can be carried through with $\gamma_\mu k_\mu \phi$ replaced by $\gamma_\mu k_\mu \phi + (1/i)\boldsymbol{\gamma}\cdot\nabla\phi$. With these approximations, ψ becomes

$$\psi \simeq \left\{\exp\left[i\left(kz + \frac{ie}{2k}(\gamma_\mu k_\mu)\gamma_4 \int_{-\infty}^{z} \phi\, dz\right)\right]\right\}u \tag{2.45}$$

Rewriting $(\gamma_\mu k_\mu)\gamma_4 = i(E + \boldsymbol{\alpha}\cdot\mathbf{k})$, one needs to evaluate

$$e^{i(\boldsymbol{\alpha}\cdot\mathbf{k})A}$$

where A does not involve spinor operators. One finds that

$$e^{i(\boldsymbol{\alpha}\cdot\mathbf{k})A} = \cos kA + i\boldsymbol{\alpha}\cdot\hat{\mathbf{k}}\sin kA$$

This is to operate in u. We assume that because the electron energy is high, u satisfies

$$\boldsymbol{\alpha}\cdot\hat{\mathbf{k}}u = u \tag{2.46}$$

so that

$$e^{i(\boldsymbol{\alpha}\cdot\mathbf{k})A} = e^{ikA}$$

Finally, then

$$\psi \simeq \left\{\exp\left[i\left(kz - \frac{k+E}{2k}\int_{-\infty}^{z} e\phi\, dz'\right)\right]\right\}u$$

$$\simeq \left\{\exp i\left(kz - \int_{-\infty}^{z} e\phi\, dz'\right)\right\}u \tag{2.47}$$

One can now insert this result into the exact equation (2.13) to obtain the scattering amplitude. The discussion from here on follows that of Ch. II [see after (VII.5.7)] and need not be repeated here.

A further approximation to (2.47) is often made. It recognizes the fact that because of the Coulomb attraction, the electron momentum increases as it approaches the nucleus. To estimate this, expand the integral in (2.47) as follows:

$$\int_{-\infty}^{z} \phi \, dz' \sim \int_{-\infty}^{0} \phi \, dz' + z\phi(z = 0, \boldsymbol{\rho}) + \cdots$$

Hence, for a given impact parameter ρ, the effective value of k is

$$k_{\text{eff}}(\boldsymbol{\rho}) = k\left(1 - \frac{e\phi(0, \boldsymbol{\rho})}{k}\right) \tag{2.48}$$

In many applications of this result, a still cruder approximation is used:

$$k'_{\text{eff}} \sim k\left(1 - \frac{e\phi(0, 0)}{k}\right) \tag{2.47'}$$

For the case of a homogeneous charge distribution of radius R,

$$\phi = -\frac{Ze}{R}\left(\frac{3}{2} - \frac{1}{2}\frac{r^2}{R^2}\right), \qquad r < R$$

this becomes

$$k'_{\text{eff}} \sim k\left(1 + \frac{3Ze^2}{2kR}\right)$$

We turn next to effects of the structure of the nucleons. The protons have a finite size [see deShalit and Feshbach (74, p. 110)]. As a consequence, we must replace (VIII.2.1) of that reference by the charge density:

$$\hat{\rho}_{\text{ch}}(\mathbf{r}) = \sum_i f(\mathbf{r} - \mathbf{r}_i) \tag{2.49}$$

where the function f replaces the point charge $\delta(\mathbf{r} - \mathbf{r}_i)$. The sum is over the protons only. The charge density then becomes

$$\rho_{\text{ch}}(\mathbf{r}) = \langle \psi | \hat{\rho}(\mathbf{r}) | \psi \rangle = Z \int \rho_N(\mathbf{r}_0) f(\mathbf{r} - \mathbf{r}_0) \, d\mathbf{r}_0 \tag{2.50}$$

where

$$\rho_N(\mathbf{r}_0) = \int \psi^*(\mathbf{r}_0, \mathbf{r}_1, \ldots)\psi(\mathbf{r}_0, \mathbf{r}_1, \ldots) \, d\mathbf{r}_1 \, d\mathbf{r}_2 \cdots$$

The form factor $\rho_{ch}(\mathbf{q})$ is

$$\rho_{ch}(\mathbf{q}) = Z\rho_N(\mathbf{q})F(\mathbf{q}) \tag{2.51}$$

Thus to obtain the nuclear form factor ρ_N, one must divide the form factor determined from experiment $\rho_{ch}(\mathbf{q})$ by $F(\mathbf{q})$, the form factor of the proton:

$$F(\mathbf{q}) = \int e^{i\mathbf{q}\cdot\mathbf{r}} f(\mathbf{r})\, d\mathbf{r}$$

A second effect originates in the interaction of the moving anomalous magnetic moment of a nucleon with an electrostatic field. That such an interaction exists can immediately be understood by transforming to the rest frame of the nucleon. Under such a transformation the electron–nucleon electrostatic field acquires a magnetic field component that will interact with nucleon magnetic moment. An interaction with the electrostatic field can, in this case, be interpreted in terms of an effective charge possessed by the nucleon. This effect was explored by Schwinger (49a) in his discussion of the polarization resulting from the interaction of a neutron with a nucleus. We now discuss its application to electron scattering.

We being with the matrix element of the current operator for a nucleon [Bjorken and Drell (64)]:

$$\langle \mathbf{p}'\lambda'|\hat{J}_\mu(0)|\mathbf{p}\lambda\rangle = \bar{u}_{\lambda'}(\mathbf{p}')\left(F_1\gamma_\mu + \frac{\kappa}{2M}F_2\sigma_{\mu\nu}q_\nu\right)u_\lambda(\mathbf{p}) \tag{2.52}$$

where F_1 and F_2 are form factors that are functions of q_μ, κ is the anomalous magnetic moment, and λ gives the helicity. The spinors $u_\lambda(\mathbf{p})$ are four-element matrices whose helicity is indicated by λ. The derivation of (2.52) follows the procedures employed in deShalit and Feshbach (74, p. 846 et seq). The spinors are given in the Appendix to Chapter IX of that reference, Eqs. (5.8)–(5.10). They can be represented by

$$u_\lambda = \left(\frac{E+M}{2E}\right)^{1/2}\begin{pmatrix} 1 & 0 \\ \dfrac{\boldsymbol{\sigma}\cdot\mathbf{p}}{E+M} & 0 \end{pmatrix}\chi_\lambda \tag{2.53}$$

where χ_λ is $\begin{pmatrix}\alpha\\0\end{pmatrix}$ or $\begin{pmatrix}\beta\\0\end{pmatrix}$, according to the value of λ. Here M is the nucleon mass. Inserting (2.53) into (2.51) and remembering that $\bar{u} = u^\dagger\gamma_4$, one obtains for the charge operator ($\mu = 4$),

$$\langle \mathbf{p}'\lambda'|\hat{\rho}(0)|\mathbf{p}\lambda\rangle \simeq -i\chi^\dagger_{\lambda'}\left[F_1 - \left(\frac{q^2}{8M} + i\frac{\mathbf{q}\cdot\boldsymbol{\sigma}\times\mathbf{p}}{4M^2}\right)(F_1 + 2\kappa F_2)\right]\chi_\lambda \tag{2.54}$$

where $E(p)$ has been replaced by $M + p^2/2M$ and terms of order up to $1/M^2$ have been retained. The $1/M$ and $1/M^2$ terms are called the Darwin–Foldy and spin-orbit terms, respectively, and contribute to the charge density.

Following Friar and Negele (75), we replace F_1 and F_2 by the Sachs form factors G_E and G_M [see (IX.3.8) et seq. in deShalit and Feshbach (74)]:

$$G_E \equiv F_1 - \frac{\kappa q^2 F_2}{M} \tag{2.55}$$

$$G_M = F_1 + \kappa F_2 \tag{2.56}$$

Therefore,

$$\langle \mathbf{p}'\lambda' | \hat{\rho}(0) | \mathbf{p}\lambda \rangle = -i\chi^\dagger_{\lambda'} \left[\left(1 - \frac{q^2}{8M^2} \right) G_E - i \frac{\mathbf{q}\cdot\boldsymbol{\sigma} \times \mathbf{p}}{4M^2} (2G_M - G_E) \right] \chi_\lambda \tag{2.57}$$

where terms of order higher than $1/M^2$ have been dropped.

The empirical value of the parameters G_E and G_M obtained from $e-p$ and $e-d$ scattering for protons and neutrons are given on page 678 of deShalit and Feshbach (74) [Feld (69)]. They are

$$G_E^{(p)} \simeq \frac{G_M^{(p)}}{\mu_p} \simeq \frac{G_M^{(n)}}{\mu_n} \simeq \frac{4M^2c^2}{\mu_n q^2} G_E^{(n)} \simeq \left[1 + \frac{q^2}{0.71(\text{GeV/c})^2} \right]^2$$

where the superscripts p and n refer to protons and neutrons, respectively. The "dipole" form given by the q dependence corresponds to an exponential charge distribution,

$$\rho_p \sim e^{-.843r} \tag{2.58}$$

with an rms radius of 0.82 fm. The units of the constant in the exponential are GeV/$\hbar$c.

Equation (2.57) gives the nucleon charge density. For a nucleus we have

$$\rho(q^2) = \sum_i \left\langle 0 \left| \hat{e}_i e^{i\mathbf{q}\cdot\mathbf{r}_i} - i\mathbf{q} \cdot \frac{2\hat{\mu}_i - \hat{e}_i}{8M^2} \{ (\boldsymbol{\sigma}_i \times \mathbf{p}_i), e^{i\mathbf{q}\cdot\mathbf{r}_i} \} \right| 0 \right\rangle \tag{2.59}$$

where (again to order q^2/M^2)

$$\hat{e}_i = \frac{1}{\sqrt{1 + q^2/4M^2}} \left(G_E^{(p)} \frac{1 + \tau_3(i)}{2} + G_E^{(n)} \frac{1 - \tau_3(i)}{2} \right) \tag{2.60}$$

$$\hat{\mu}_i = \frac{1}{\sqrt{1 + q^2/4M^2}} \left(G_M^{(p)} \frac{1 + \tau_3(i)}{2} + G_M^{(n)} \frac{1 - \tau_3(i)}{2} \right) \tag{2.61}$$

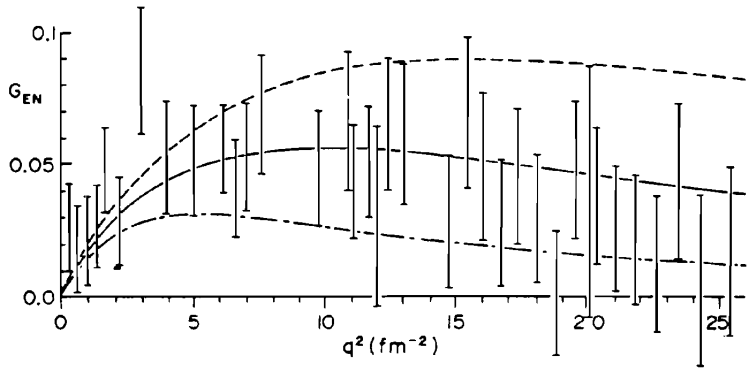

FIG. 2.1. Neutron form factor assuming an exponential neutron charge distribution compared with experimental data extracted with the use of Hamada–Johnston and boundary conditions model deuteron wave functions. Solid, dashed, and dashed–dotted curves correspond to average neutron radii equal to 0.80, 0.63, and 1.07 fm, respectively. [From Bertozzi, Friar, et al. (72).]

As Bertozzi et al. (72) have shown, the neutron charge distribution can have a considerable effect on the electron scattering. The experimental results for $G_E^{(n)}$ are shown in Fig. 2.1. The consequences for elastic scattering by ^{40}Ca and ^{208}Pb are shown in Fig. 2.2. The effects are substantial and especially large at the cross section minima and large momentum transfers.

Two other effects have been subjects of several investigations. The first of these is referred to as a dispersion correction, which arise as the result of the virtual excitation of the target nucleus by the incident electron. The electron excites the target nucleus, and then in a second interaction the nucleus deexcites, returning to its ground state if we are discussing elastic scattering. As we have seen in Chapter II, where the identical process is discussed in a multiple scattering approximation, the cross section for this process depends on the pair correlation function $C(\mathbf{r}_1, \mathbf{r}_2)$. However, calculations indicate that the dispersion effects are small [see Bethe and Molinari (71) and Friar and Rosen (74)] and little information on $C(\mathbf{r}_1, \mathbf{r}_2)$ can be obtained from these experiments.

We finally mention dynamical nuclear recoil corrections. These have been treated using the Breit (29) two-body interaction by Grotch and Yennie (69). These corrections also turn out to be small [see Sick and McCarthy (70)].

D. Model Independence

At a comparatively low energy (but still such that $k \gg m$) (m = electron mass) the product kR can be much less than 1. Under those circumstances only the $l = 0$ phase shift, δ_0 is affected by the finite nuclear size. Moreover, as we shall show, that phase shift depends only on the rms nuclear radius and does not depend on other nuclear parameters.

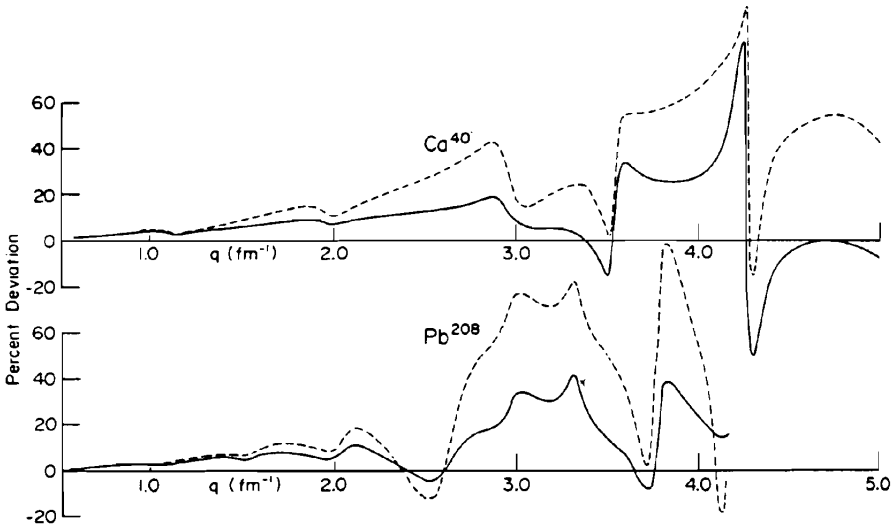

FIG. 2.2. Fractional change in electron scattering cross sections caused by including the charge density arising from the finite spatial charge distribution of the neutron for ^{40}Ca and ^{208}Pb. The dashed and solid curves denote the effect obtained using the maximal and minimal neutron form factors, respectively. [From Bertozzi, Friar, et al. (72).]

Let us compare the results obtained with two differing potentials V_1 and V_2. The Dirac wave functions satisfy (2.27):

$$(E-m-V_1)G_1+\frac{df_1}{dr}-\frac{\kappa f_1}{r}=0$$

$$-(E+m-V_1)f_1+\frac{dG_1}{dr}+\frac{\kappa G_1}{r}=0$$

We now form

$$G_2\frac{df_1}{dr}-f_2\frac{dG_1}{dr}+f_1\frac{dG_2}{dr}-G_1\frac{df_2}{dr}=\frac{d}{dr}(f_1G_2)-\frac{d}{dr}(f_2G_1)$$

$$=(V_1-V_2)(G_1G_2+f_1f_2)$$

Integrating both sides from zero to infinity yields

$$f_1G_2-f_2G_1\Big|_0^\infty=\int_0^\infty(V_1-V_2)(G_1G_2+f_1f_2)\,dr$$

Using the asymptotic forms for f and G, the left-hand side equals

$$(\varepsilon^2 - 1)^{1/2} \sin(\delta_1 - \delta_2) = -\int_0^\infty (V_1 - V_2)(G_1 G_2 + f_1 f_2)\, dr \tag{2.62}$$

Note that the difference $(V_1 - V_2)$ does not contain the long-range part of the Coulomb potential. Let

$$V_i \equiv -\frac{Ze^2}{r} + \bar{V}_i \tag{2.63}$$

Then

$$V_1 - V_2 = \bar{V}_1 - \bar{V}_2 \tag{2.64}$$

We see that two descriptions of the finite nuclear size will yield the same phase shift if

$$\int_0^\infty \bar{V}_1 (G_1 G_2 + f_1 f_2)\, dr = \int_0^\infty \bar{V}_2 (G_1 G_2 + f_1 f_2)\, dr$$

In the long-wavelength limit ($kR \ll 1$),

$$G_1 G_2 + f_1 f_2 \sim r^2 \qquad kR \ll 1 \tag{2.65}$$

Elastic electron scattering experiments satisfying $kR \ll 1$ therefore determine one parameter,

$$I = \int_0^\infty \bar{V} r^2\, dr \tag{2.66}$$

This result was obtained by Feshbach (51) employing a variational method [see also Elton (53) and Bodmer (53)]. Using the Poisson equation, $\bar{V}$ can be expressed in terms of the charge density ρ_{ch}. One can then express I in terms of ρ_{ch}, with the result that when $kR \ll 1$, elastic electron scattering experiments determine the rms radius of the charge in the nucleus:

$$r_{\text{rms}}^2 = \frac{\int r^2 \rho_{\text{ch}}\, d\mathbf{r}}{\int \rho_{\text{ch}}\, d\mathbf{r}} \tag{2.67}$$

At higher energies, when $kR \lesssim 1$ the approximation given by (2.65) is no longer valid. The methods for extracting ρ_{ch} from the elastic scattering data then employed is referred to as a *model-independent analysis.* It is, in fact, a method designed to obtain an estimate of the uncertainty in ρ_{ch} so obtained. There are two sources of error. One is, of course, the experimental error. A second has

its origin in the fact that a given experiment determines the elastic scattering up to a maximum momentum transfer, q_{max}. However, to obtain $\rho(\mathbf{r})$ from $\rho(\mathbf{q})$ from the inverse Fourier transform,

$$\rho(\mathbf{r}) = \left(\frac{1}{2\pi}\right)^3 \int \rho(\mathbf{q}) e^{-i\mathbf{q}\cdot\mathbf{r}}\, d\mathbf{q}$$

$$= \frac{1}{2\pi^2} \int_0^\infty \rho(q) \frac{\sin qr}{r} q\, dq$$

requires a knowledge of q beyond q_{max}.

There are a number of procedures that have been developed. These are reviewed by Friar and Negele (75), who described the work of Friedrich and Lenz (72), Borysowicz and Hetherington (73, 74), Friar and Negele (73, 75), Sick (74), and others. Briefly, one writes the density as follows:

$$\rho = \rho_0(r) + \sum_1^M C_i f_i(r) \tag{2.68}$$

The quantity ρ_0 is a zeroth-order approximation obtained from, for example, a density-dependent Hartree–Fock calculation or more phenomenologically from a fit using the "Fermi" charge density distribution, which in its most elaborate form is

$$\rho_{Fm} = \frac{\rho_0(1 + wr^2/c^2)}{e^{(r-c)/a_0} + 1} \tag{2.69}$$

where ρ_0, w, c, and a_0 are parameters that are chosen to give a best fit to experiment. Modern calculations generally use the Hartree–Fock for ρ_0 because among other things these give good descriptions of the surface properties of nuclei. The functions f_i are a complete set, for example [Meyer–Berkhout, K. W. Ford, et al. (59)],

$$f_i = \frac{1}{r} \sin \frac{i\pi r}{R} \Theta(r - \bar{R}) \tag{2.70}$$

where $\bar{R}$ is chosen to be in the region where ρ vanishes. The parameter M is given by

$$M = \frac{R}{\pi} q_{max} \tag{2.71}$$

since experiment does not provide data beyond q_{max}. The spatial resolution

obtained from the analysis of experiment is

$$\Delta r \sim \frac{\pi}{q_{\max}}$$

On the other hand, the resolution in momentum space is

$$\Delta q \sim \frac{\pi}{r_{\max}}$$

where $r_{\max}$ is the largest value of r for which ρ is determined. Or the largest value of r, $r_{\max}$, for which ρ can be accurately known is

$$r_{\max} \sim \frac{\pi}{\Delta q} \tag{2.72}$$

where Δq is now the experimental momentum resolution. As a consequence of this result, one can expect that the large r dependence of ρ will not be well determined by experiment. It is for this reason that the density-dependent Hartree–Fock results have been used for $\rho_0(r)$ in (2.68).

In the procedure used by Friar and Negele, one first obtains the coefficients C_i from experiment using perturbation theory, which gives a linear relation between the cross sections and the density, to obtain a first approximation to the coefficients C_i. The resulting ρ is inserted into the Dirac equation to obtain a more accurate calculation of the cross section. The C_i's are modified by perturbation theory to take care of the differences from the experimental cross sections and the entire process is repeated. For ^{208}Pb, Friar and Negele found that with 11 terms in the series, three iterations were needed. The quantity M can also be varied. It is found that once M exceeds $(R/\pi)q_{\max}$ [Eq. (2.71)], the χ^2 increases significantly. Over the last decade this method, and others surveyed by Friar and Negele (75), have been fine tuned, and with the great increase in experimental accuracy and extension to larger values of $q_{\max}$, excellent descriptions of the charge density of spin-zero nuclei has been achieved. The example in Fig. 2.3 shows the percent of deviation from experiment using the analysis just described for both the Mainz data [Rothaas (78)] and the earlier 1970 Stanford and 1972 Amsterdam data.

One should bear in mind that additional important data are provided by μ mesonic atoms and must be included in the analysis. We shall not discuss this aspect here. [See the discussions in Friar and Negele (75) and Barrett and Jackson (77).]

Some of the results for ρ_{ch} obtained with this or related analyses are shown in Figs. 2.4 and 2.5. The thickness of the line indicates the uncertainty in the experimental determination of ρ_{ch}. The dashed line gives the density-dependent Hartree–Fock results and the dotted lines show the effect of going beyond the

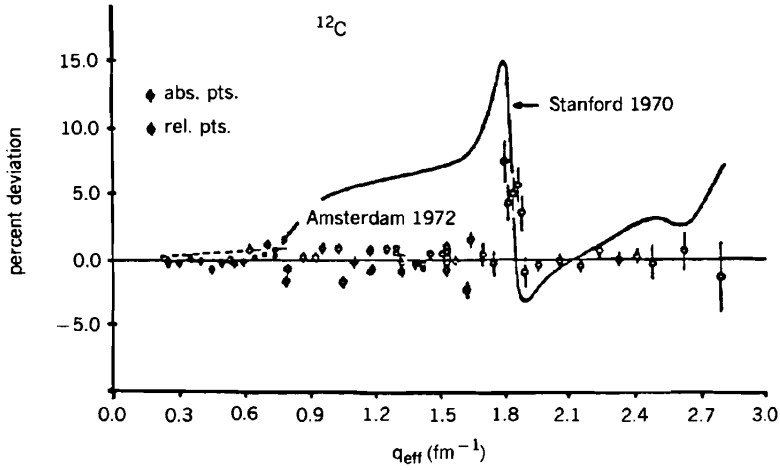

FIG. 2.3. Deviation from model-independent analysis. Solid line, Stanford data, 1970; dashed line, Amsterdam data, 1972; points, Mainz data, 1982. [From Bertozzi (82).]

mean field by using the RPA. We note a significant difference between experiment and theory for the small r. In all cases, even upon including the RPA, the theory predicts too large a density. The RPA correlations do damp the fluctuations in the interior nuclear region. [See Negele and Vautherin (72, 75), Gogny (79), Dechargé and Gogny (68), and Dechargé and Sips (83)]. We are left with the general remark that further correlations and/or two-body components of the correlation need to be included, although it is not clear whether short- or long-range correlations are needed.

An important insight is obtained by comparing the electron scattering by ^{206}Pb and ^{205}Tl [Euteneuer, Friedrich, and Voegler (78); Cavedon et al. (82)]. These two nuclei differ in their single-particle structure by a $3s$ proton. The impact of this difference is shown in Fig. 2.6, where the ratio of σ (^{205}Tl) to $\sigma(^{206}\text{Pb})$ is compared with the mean field prediction. We see a strong characteristic peak at $q = 2$ in both theory and experiment. However, agreement with the peak strength is obtained only if the single particle occupation probability is reduced by 30%. This is demonstrated once again in Fig. 2.7, where one sees the reduction in the charge density from that predicted by mean field theory [Frois et al. (83)]. It is this reduction that we see in Fig. 2.5 for ^{208}Pb. As Zamick, Klemt, and Speth (75) point out, ^{205}Tl is not obtained only by creating a proton hole in the ground state of ^{206}Pb. There are also components coming from a proton–hole in the excited states of ^{206}Pb, such as a $d_{3/2}$ hole and $d_{5/2}$ hole in the 2^+ excited state. The data demonstrating this are provided by the reaction ^{206}Pb (^{3}He, d). The correlations in this case are long range.

We conclude this section on charge scattering from spherical nuclei with Table 2.1, which lists rms radii obtained from experiment and theory [DeJager

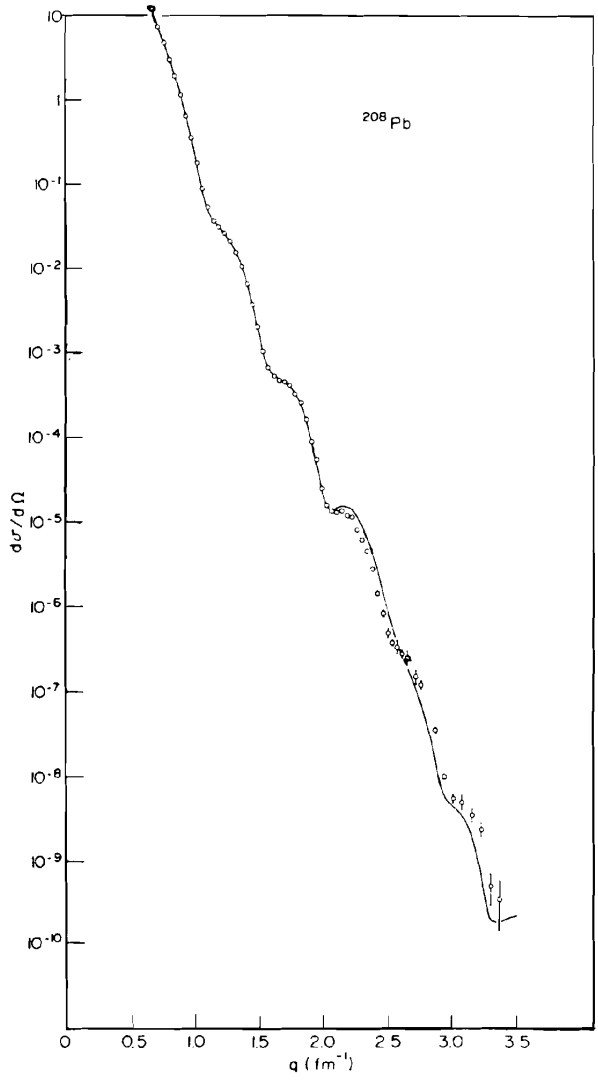

FIG. 2.4. Cross sections for elastic electron scattering from ^{208}Pb at 502 MeV compared with DME mean-field theory prediction (solid line). [From Negele (82).]

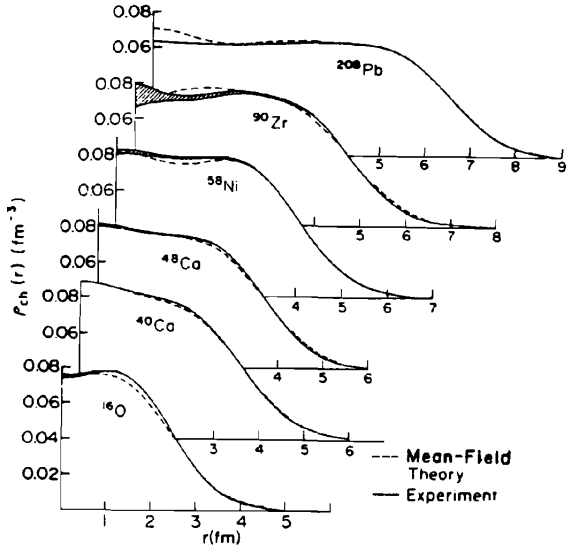

FIG. 2.5. Comparison of DME mean-field theory charge distributions in spherical nuclei (dashed lines) with empirical charge densities. The solid curves and shaded regions represent the error envelope of densities consistent with the measured cross sections and their experimental uncertainties. [From Negele (82).]

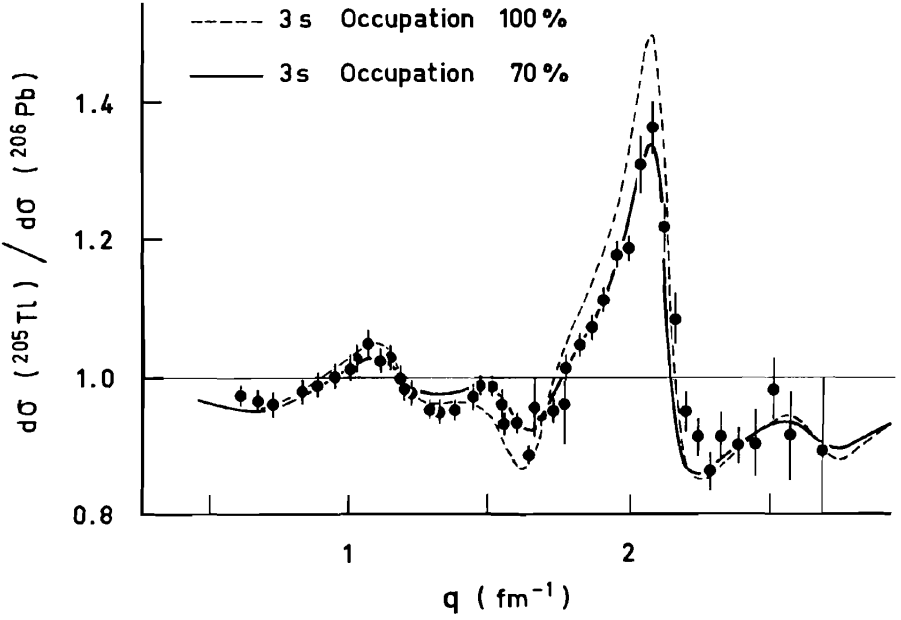

FIG. 2.6. Ratio of elastic cross sections from ^{205}Tl and ^{206}Pb. The peak at $q = 2\,\text{fm}^{-1}$ is the signature of the 3*s* orbit. The curves are mean-field predictions due to X. Campi. [From Frois and Papanicolas (87).]

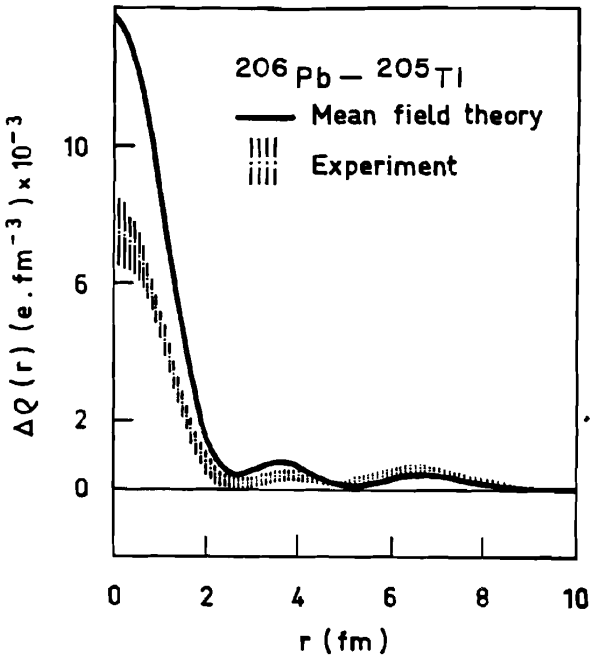

FIG. 2.7. Charge density difference of ^{206}Pb and ^{205}Tl. [From Frois and Papanicolas (87).]

TABLE 2.1

	$\langle r^2 \rangle_{ch}^{1/2}$ (fm)	
	Theory	Experiment
^{16}O	2.79	2.71 ± 0.01
^{40}Ca	3.50	3.48
^{48}Ca	3.50	3.47
^{56}Ni	3.80	4.78
^{190}Zr	4.29	4.28 ± 0.02
^{116}Sn	4.63	4.62 ± 0.01
^{200}Pb	5.49	5.50

DeVries, and DeVries (74)]. See also the more extensive table, Table 6.2, in Barrett and Jackson (77).

E. Deformed Nuclei[‡]

Elastic and inelastic scattering of electrons by deformed nuclei demonstrate the electron's power as a probe of nucleon structure. As discussed in Chapter VI of deShalit and Feshbach (74), the rotational wave function is given in terms of an intrinsic wave function χ_K and a factor depending on the Euler angles, which transforms the wave function for a body fixed to a space-fixed coordinate system. The wave function is [see (VI.4.9) in deShalit and Feshbach (74)]

$$\psi(IKM) = \sqrt{\frac{2I+1}{16\pi^2}}[D^{I*}_{MK}(\theta_K)\chi_K(\mathbf{r}'_i) + (\hat{-})^{I-J}D^{I*}_{M,-K}(\theta_K)\chi_{-K}(\mathbf{r}'_i)] \qquad K>0 \tag{2.73a}$$

while for $K=0$,

$$\psi(I,K=0,M) = \frac{1}{\sqrt{2\pi}}Y_{1m}(\theta_K)\chi_{K=0}(\mathbf{r}') \tag{2.73b}$$

As pointed out in that chapter, the ratio of the electromagnetic transition probabilities within a rotational band for a particular multipole [see (VI.6.21) and (VI.6.22) in deShalit and Feshbach (74)] do not depend on the intrinsic wave function, but only on the quantum numbers I_f, I_i, and K. This is a consequence of the fact that the wave function for each member of a rotational band contains the same intrinsic wave function χ_K. The electromagnetic transitions tests this property of the rotational wave functions at $q=0$. The electron scattering experiments extends that test to finite q, thus checking that $\chi_K(\mathbf{r})$ is the same for each member of the rotational band as a function of $\mathbf{r}$.

Inelastic scattering will play an important role since we shall compare cross sections for the excitation of different members of usually the ground-state band. The electron–nuclear interaction responsible for the transition can be treated perturbatively, but the plane wave approximation is not valid for the heavier target nuclei. The appropriate formalism is the DWA (see Chapter VI for its use in dealing with inelastic processes) in which in this case the Coulomb interaction is treated exactly, while the transition Hamiltonian is taken into account using perturbation theory.

We shall only outline the DWA for this case. The details are similar to those given in Chapter VI, with some special details because of the required Dirac algebra. The details can be found in Überall's (71) second volume. The Hamiltonian of the system is given by

$$H = H_N + H_D + H_{\text{int}} \tag{2.74}$$

[‡]Moya de Guerra (86).

where H_N is the Hamiltonian of the nucleus and H_D is the Dirac Hamiltonian,

$$H_D = (\boldsymbol{\alpha}\cdot\mathbf{p}) + \beta m \tag{2.75}$$

and for charge scattering

$$H_{\text{int}} = e\phi \tag{2.76}$$

where ϕ depends on the charge distribution in the nucleus. One then defines the diagonal and transfer part of ϕ with respect to the wave functions of the nucleus as follows:

$$\hat{\phi}_D = I\rangle\langle I|\phi|I\rangle\langle I \tag{2.77}$$

$$\hat{\phi}_{\text{tr}} = \sum_{I'} I\rangle\langle I|\phi|I'\rangle\langle I' + \text{h.c.} \qquad I \neq I'$$

By taking the matrix element of the Schrödinger–Dirac equation,

$$H\Psi = E\Psi$$

one obtains a set of coupled equations for the spinor electron wave function ψ_I:

$$[H_D + e\hat{\phi}_D]\psi_I = -\sum\langle I|\hat{\phi}_{\text{tr}}|I'\rangle\psi_{I'}$$

The DWA result for the transition $I \to I'$ is obtained by solving the approximate equations

$$[H_D + e\hat{\phi}_D]\psi_I = 0 \tag{2.78a}$$

$$[H_D + e\hat{\phi}_D]\psi_{I'} = -\langle I'|\hat{\phi}_{\text{tr}}|I\rangle\psi_I \tag{2.78b}$$

The solution of (2.78*a*) gives the elastic scattering from the nucleus, while (2.78*b*) yields the inelastic scattering. The solution of (2.78*a*) for ψ_I can be obtained in a partial wave series as in the preceding section. That series, substituted in (2.78*b*), leads to the desired wave function $\psi_{I'}$, also expressed in a partial wave series.

To obtain an insight into what can be learned from this analysis, we return to the Born approximation for the inelastic reaction in which discrete nuclear levels are excited. The cross section in the center-of-mass system is

$$\frac{d\sigma}{d\Omega} = \sigma_M \frac{1}{2J_i + 1} \sum_{M_i M_f} |\langle J_f M_f|\rho(\mathbf{q})|J_i M_i\rangle|^2 \tag{2.79}$$

where σ_M is the Mott cross section. But $\rho(\mathbf{q})$ can be expanded in a partial wave

series,

$$\rho(\mathbf{q}) = \int e^{i\mathbf{q}\cdot\mathbf{r}}\rho(\mathbf{r})\,d\mathbf{r}$$

$$= \sum_{JM} 4\pi i^J \int j_J(qr)\,Y_{JM}(\hat{\mathbf{r}})\,Y^*_{JM}(\hat{q})\rho(\mathbf{r})\,d\mathbf{r}$$

so that

$$\langle J_f M_f|\rho(\mathbf{r})|J_i M_i\rangle = 4\pi \sum_{JM} i^J Y^*_{JM}(\hat{\mathbf{q}})\langle J_f M_f|\hat{M}^{(c)}_{JM}(\mathbf{q})|J_i M_i\rangle \tag{2.80}$$

In this equation

$$\hat{M}^{(c)}_{JM}(\mathbf{q}) = \int j_J(qr)\,Y_{JM}(\hat{\mathbf{r}})\rho(\mathbf{r})\,d\mathbf{r} \tag{2.81}$$

so that (2.80) is the multipole expansion of ρ and $\hat{M}^{(c)}_{JM}$ transforms like a tensor operator of order J. Using the Wigner–Eckart theorem, one has

$$\langle J_f M_f|\hat{M}^{(c)}_{JM}(\mathbf{q})|J_i M_i\rangle = (-)^{J_f - M_f}\begin{pmatrix} J_f & J & J_i \\ -M_f & M & M_i \end{pmatrix}(J_f\|\hat{M}^{(c)}_J(\mathbf{q})\|J_i) \tag{2.82}$$

Performing the indicated sums, using the sum rules of Appendix A of deShalit and Feshbach (74), one obtains

$$\frac{d\sigma}{d\Omega} = \sigma_M \frac{1}{2J_i+1}\sum_J |(J_f\|\hat{M}^{(c)}_J(\mathbf{q})\|J_i)|^2 \tag{2.83}$$

For deformed nuclei, the matrix element of $\hat{M}^{(c)}_{JM}$ has been derived [(VI.6.9) in deShalit and Feshbach (74), where J_i is replaced by I' and J_f by I]. One obtains

$$(IK\|\hat{M}^{(c)}_J(\mathbf{q})\|I'K') = \sqrt{(2I+1)(2I'+1)}$$
$$\times \sum_\mu \left\{ \begin{pmatrix} I & J & I' \\ -K & \mu & K' \end{pmatrix}\langle K|\hat{M}^c_{J\mu}(\mathbf{q})|K'\rangle \right.$$
$$\left. + (-)^{I'}\begin{pmatrix} I & J & I' \\ -K & \mu & -K' \end{pmatrix}\langle K|\hat{M}^{(c)}_{J\mu}(\mathbf{q})|-K'\rangle \right\} \tag{2.84}$$

This result holds for K and $K' \neq 0$. When K' is zero,

$$(I, K\|M^{(c)}_J\|I', K'=0) = \sqrt{(2I+1)(2I'+1)}\begin{pmatrix} I & J & I' \\ -K & K & 0 \end{pmatrix}$$
$$\times \langle K|\hat{M}^{(c)}_{J_0}(\mathbf{q})|K'=0\rangle \begin{cases} \sqrt{2} & K \neq 0 \\ 1 & K = 0 \end{cases} \tag{2.85}$$

In these equations $\hat{M}_J^{(c)}(\mathbf{q})$ are calculated in the body-fixed coordinate system. The matrix elements $\langle K|\hat{M}_J^{(c)}(\mathbf{q})|K'\rangle$ involve only the intinsic wave functions χ_K and are independent of I and I' as long as I and I' are members of the corresponding rotational bands. Thus the electron-induced transitions between members of the two bands (which can be identically) will each involve the matrix elements of $\hat{M}_J$. These will, of course, vary with J so that differing aspects of χ_K will be probed by the inelastic scattering. Analysis of the data should then yield the $\mathbf{q}$ dependence of the matrix elements. In the case of even–even nuclei transitions from the ground state ($I' = 0 = K'$) to excited states of the same band ($I, K = 0$), only one matrix element $\langle K = 0|\hat{M}_J^c(\mathbf{q})|K' = 0\rangle$ enters for each J and I.

When the spin of the ground state is not zero, several matrix elements are involved in a given transition. Nevertheless, one can determine each of these as the following example illustrates [Bertozzi (82)]. Suppose that the energy spectrum of a nucleus is given by Fig. 2.8. The multipole matrix elements involved in a given transition are shown. The matrix elements of the multipole operators with respect to the intrinsic wave functions [see (2.8)] are identical for each of the transitions indicated. There are five transitions and four matrix elements, $M0, M2, M4$, and $M6$. One can, for example, determine the matrix elements using four of the transitions and predict the fifth, thereby testing the correctness of the wave function (2.72). Bertozzi (82) gives an example of such a test. The nucleus is ^{175}Lu with a ground state of spin of $7/2^+$. The 7/2, 9/2, 13/2, 15/2 cross sections are used to predict the 11/2 cross section. The results are shown in Fig. 2.9. The agreement is good, demonstrating the validity of the rotational model.

The cross section given by (2.83) applies as well to inelastic scattering from spherical nuclei in the Born approximation. It is traditional to use the concept of transition charge density ρ_{tr} in these cases. It is defined as follows:

$$(J_f \| \hat{M}_J^{(c)}(\mathbf{q}) \| J_i) = \int_0^\infty j_J(qr)\rho_{tr}(r)r^2\, dr \tag{2.86}$$

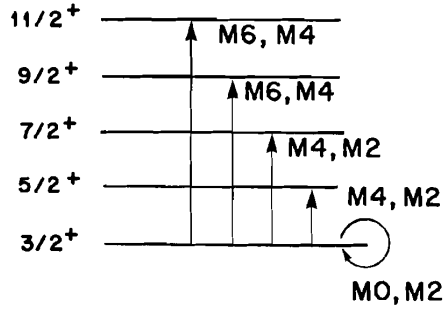

FIG. 2.8. Possible multipole excitations.

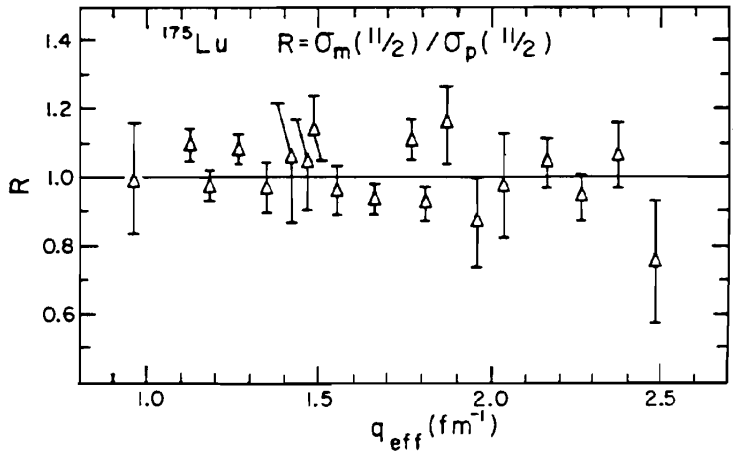

FIG. 2.9. Test of single intrinsic state assumption of the rotational model. The nucleus is ^{175}Lu. R is the ratio of the measured $\frac{11}{2}^+$ cross section to the value predicted from the measured $\frac{7}{2}$, $\frac{9}{2}$, $\frac{13}{2}$, and $\frac{15}{2}$ cross sections. [From Bertozzi (82).]

Inserting (2.82) yields

$$\rho_{\rm tr}(r) = \int d\Omega\, Y_{JM}(\hat{\mathbf{r}}) \times \left[(2J+1) \sum_{M_i,M_f} (-)^{J_f - M_f} \begin{pmatrix} J_f & J & J_i \\ -M_f & M & M_i \end{pmatrix} \langle J_f M_f | \rho(\mathbf{r}) | J_i M_i \rangle \right] \tag{2.87}$$

Since $(J_f \| \hat{M}_J^{(c)} \| J_i)$ is independent of M, we can choose M. A convenient choice is $M = 0$. For even–even nuclei, $J_i = 0$ and $\rho_{\rm tr}$ equals

$$\rho_{\rm tr}(r) = (2J+1)^{1/2} \int d\Omega\, Y_{J0}(\hat{\mathbf{r}}) \langle J0 | \rho(\mathbf{r}) | 00 \rangle \tag{2.87'}$$

where we have used

$$\begin{pmatrix} J_f & J & 0 \\ 0 & 0 & 0 \end{pmatrix} = \frac{(-)^J \delta_{J_f,J}}{\sqrt{2J+1}}$$

Obtaining $\rho_{\rm tr}$ involves determining $(J_f \| \hat{M}_J^{(c)}(\mathbf{q}) \| J_i)$ from experiment and then inverting (2.86) with the attendant difficulties discussed earlier in this chapter. A model-independent resolution is available in this case as well.

These levels can also be excited by the interaction of the electron with the nuclear currents. However, it is possible, as we shall see, using suitable kinematics and analysis to extract the charge- and current-induced cross section separately.

The transition densities obtained from inelastic scattering by several magic nuclei to the highly collective 3^- state and by ^{90}Zr to the $2^+, 4^+, 6^+, 8^+$ states are shown in Figs. 2.10 and 2.11.

The transition density for both of these cases peaks strongly at the surface. The dashed line in Fig. 2.10 gives the theoretical results obtained using an RPA description of the states involved. The general structure of the prediction does follow experiment. But there are deviations. The peak transition density can differ substantially from experiment, while for the interior the theoretical results

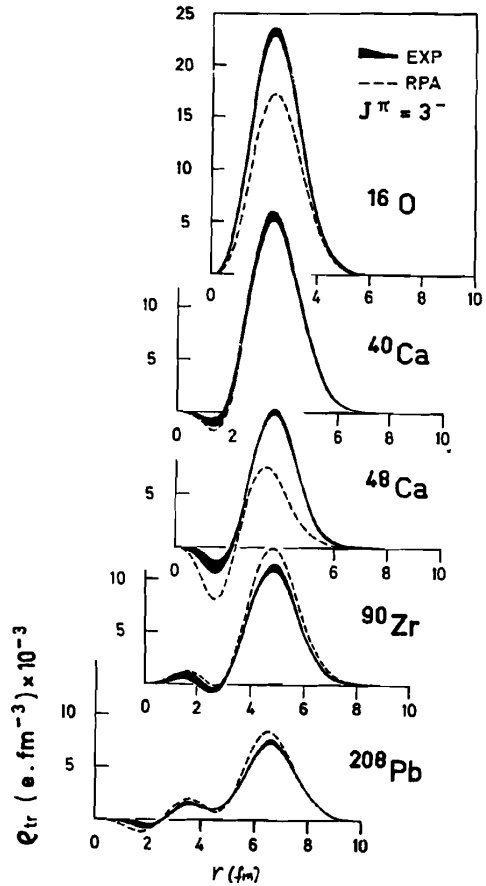

FIG. 2.10. Transition charge densities for the first collective octupole vibrations of doubly closed shell nuclei. Experimental uncertainty is given by the thickness of the solid line. The theoretical predictions are obtained in a self-consistent RPA calculation. [From Frois and Papanicolas (87).]

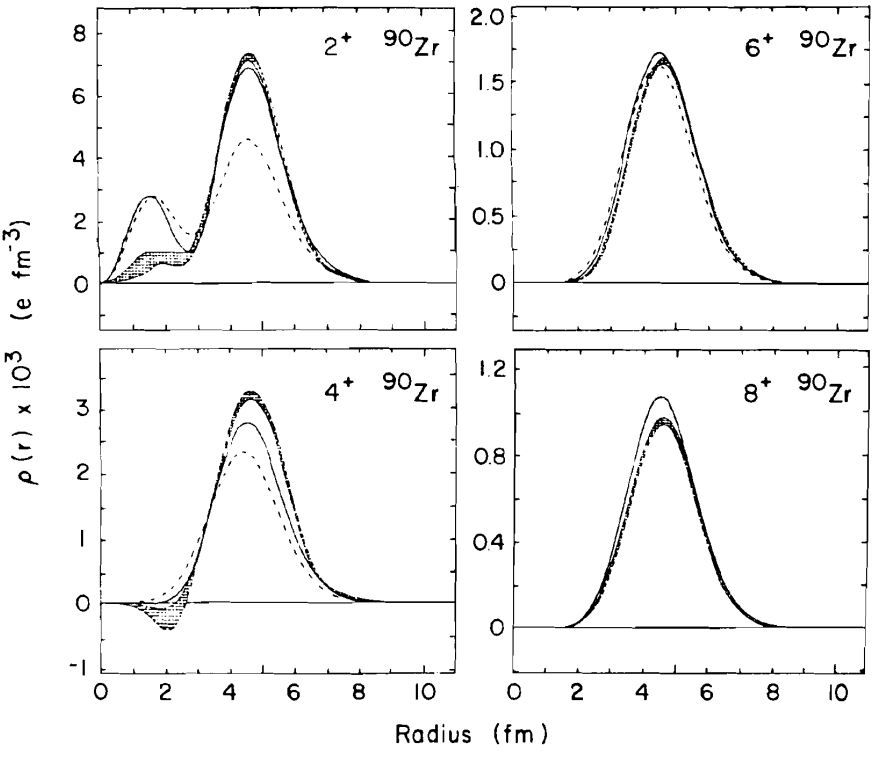

FIG. 2.11. Experimental and calculated transition densities for the 2^+, 4^+, 6^+, and 8^+ multiplet in ^{90}Zr. [From Heisenberg (87).]

oscillate more violently than the data. Figure 2.11 contains a comparison between the experimental and calculated transition charge density. In the single-particle picture, these transitions are to states in which two protons in the filled $1g_{9/2}$ orbitals are recoupled to spin 2^+, 4^+, 6^+, and 8^+. In the ground state they couple to zero. As Fig. 2.11 shows, the calculations based on this simple assumption fail substantially for the 2^+ and 4^+ but are satisfactory for the 6^+ and 8^+ states. The solid line includes the effect of core polarization (i.e., the inclusion of states in which the core is excited). As we see from the figure, core polarization does have some effect in the 2^+ and 4^+ cases, but that effect is nearly not large enough to reduce the small r fluctuations in the 2^+ case, although it does greatly improve the agreement in the main peak.

Comparing the experimental transfer charge density with theory reveals the same diseases that were seen with spherical nuclei namely the predictions in the interior deviate from experiment. This is illustrated in Fig. 2.12. In Fig. 2.12*a* the theory predicts too large a charge density in the interior. In Fig. 2.12*b* the theoretical ρ_{tr} fluctuates more strongly than its experimental values in the interior, although theory and experiment are in good agreement in the surface

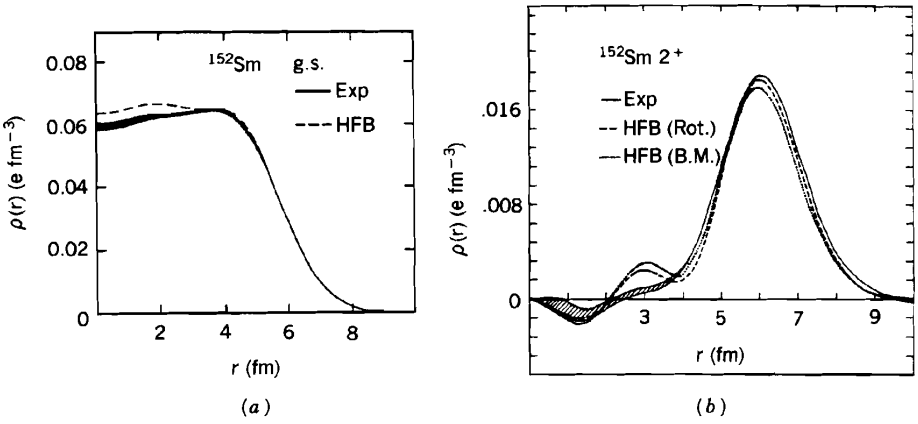

FIG. 2.12. (*a*) Charge density for ground state of ^{152}Sm; (*b*) transition charge density for excitation of the 2^+ level in ^{152}Sm. [From Bertozzi (82).]

region. This substantially good agreement for the $0^+ \rightarrow 2^+$ transition deteriorates somewhat for the $0 \rightarrow 4^+$. This is a general pattern for the rare earth nuclei and for ^{238}U according to Bertozzi.

F. A Remark on the Charge Density

The two-body density matrix $\rho(\mathbf{r}_1, \mathbf{r}_2)$ has been discussed in Ch. III (where it was called K). There it was shown [III2.88 Feshbach (62)] that it could be written as

$$\rho(\mathbf{r}_1, \mathbf{r}_2) = \sum \kappa_\alpha \omega_\alpha(\mathbf{r}) \omega_\alpha^*(\mathbf{r}_2) \tag{2.88}$$

where

$$\langle \omega_\alpha(r_1) \omega_\beta(\mathbf{r}_1) \rangle = \delta_{\alpha\beta} \tag{2.89}$$

and

$$\int \rho(\mathbf{r}_1, \mathbf{r}_2) \omega_\alpha(\mathbf{r}_2)\, d\mathbf{r}_2 = \kappa_\alpha \omega_\alpha(\mathbf{r}_1) \tag{2.90}$$

The density is

$$\rho(\mathbf{r}_1) = \rho(\mathbf{r}_1, \mathbf{r}_1) = \sum \kappa_\alpha |\omega_\alpha(r_1)|^2 \tag{2.91}$$

In the case of a Slater determinant, $\kappa_\alpha = 1$. But the many-body wave functions are generally not single Slater determinants, so that generally $\kappa_\alpha \neq 1$ but will lie between 0 and 1. One can interpret κ_α as giving the occupation probability of the orbital, ω_α. In fact, the interior deviations observed in nearly all of the

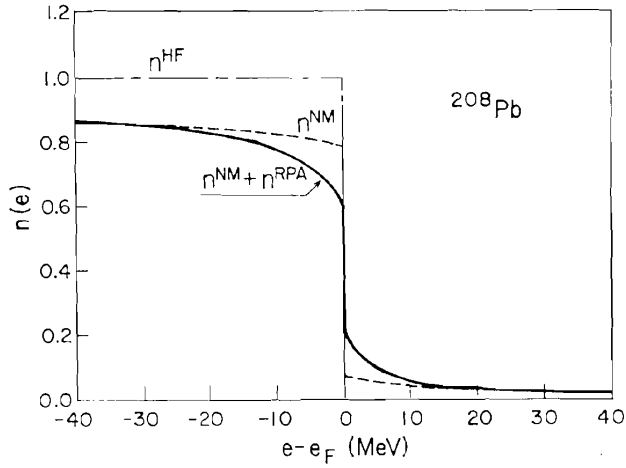

FIG. 2.13. Calculated occupation probabilities in ^{208}Pb. [From Heisenberg (87).]

nuclei, including both the spherical and deformed nuclei can be explained if the occupation probabilities of the single-particle orbitals have been chosen appropriately. Their deviation from unity is an expression of the existence of residual interactions and the consequent correlations. Pandharipande, Papanicolas, and Wambach (84) have calculated the occupation probabilities for ^{208}Pb. The results are shown in Fig. 2.13, where HF refers to Hartree–Fock, and NM to nuclear matter calculations. The overall reduction in n, the occupation number, is qualitatively in accordance with the experimental situation. But experimental uncertainties in the $3s_{1/2}$ occupation probability are, according to Heisenberg (87), too large for a definitive comparison of experiment and theory. (See Heisenberg for a discussion of the E5 transitions in ^{89}Y, ^{90}Zr, and ^{92}Mo.)

G. Current-Induced Scattering

We continue with the Born approximation. We return to Dirac equation (2.12). The vector potential A_μ is a solution of the inhomogeneous wave equation

$$\nabla^2 A_\mu + \omega^2 A = -4\pi j_\mu \tag{2.92}$$

where simple haromonic time dependence has been assumed. Then in momentum space

$$A_\mu = \frac{4\pi j_\mu}{q^2 - \omega^2} = \frac{4\pi j_\mu}{q_\mu^2} \tag{2.93}$$

$$q_\mu^2 = q^2 - \omega^2 \tag{2.94}$$

Equation (2.12′) is replaced by

$$(\nabla^2 + k'^2)\psi = -e(\gamma_\nu p_\nu + im)(\gamma_\mu A_\mu)\psi_i$$

where k' is the electron momentum with the nucleus excited, ψ the corresponding wave function, and ψ_i the elastic scattering (nucleus in the ground state) wave function. In the DWA approximation,

$$\hat{f} = \frac{e}{4\pi}\int e^{-i\mathbf{k}'\cdot\mathbf{r}}(\gamma_\nu p_\nu + im)(\gamma_\mu A_\mu)\psi_i^{(+)}$$

On introducing (2.93) and making the Born approximation [see (2.14)] we obtain

$$f_{fi} = \frac{e}{q_\mu^2}\langle u_f(\gamma_\nu k'_\nu + im)(\gamma_\mu j_\mu(\mathbf{q}))u_i\rangle \tag{2.95}$$

where

$$j_\mu(\mathbf{q}) = \int e^{i\mathbf{q}\cdot\mathbf{r}} j_\mu(\mathbf{r})\, d\mathbf{r} \tag{2.96}$$

To obtain the cross section for a nuclear transition $J_i \to J_f$ and electron spins from m_i and m_f, we must calculate

$$\frac{d\sigma}{d\Omega} = \frac{1}{2}\frac{1}{2J_i+1}\sum_{\substack{M_i,M_f\\ m_i m_f}} |\langle J_f M_f; m_f | f_{fi} | J_i M_i; m_i\rangle|^2 \tag{2.97}$$

The sum over the electron spin is obtained by using the technique following (2.17). The result is

$$\frac{1}{2}\sum_{m_i m_f} |\langle J_f M_f; m_f | f_{fi} | J_i M_i; m_i\rangle|^2 = \frac{e^2}{q_\mu^4}\frac{k'}{k}[k_\nu k'_\sigma - \delta_{\nu\sigma}k_\kappa k'_\kappa + k_\sigma k'_\nu] j_\sigma(\mathbf{q}) j_\nu^*(\mathbf{q}) \tag{2.98}$$

where the summation convention is used. Following DeForest and Walecka (66), one introduces the coordinates

$$Q_\mu = \tfrac{1}{2}(k_\mu + k'_\mu) \tag{2.99}$$

Replacing then k_μ and k'_μ by Q_μ and q_μ and bearing in mind that $Q_\mu^2 = -\frac{1}{4}q_\mu^2$, one obtains

$$\sigma = \frac{e^2}{q_\mu^4}\frac{k'}{k}\frac{1}{2J_i+1}\sum_{M_i M_f}[2(Q_\nu \bar{j}_\nu^*)(Q_\sigma \bar{j}_\sigma) + \tfrac{1}{2}q_\sigma^2 \bar{j}_\mu^* \bar{j}_\mu]$$

where

$$\bar{J}_\sigma = \langle J_f M_f | j_\sigma | J_i M_i \rangle \tag{2.100}$$

Further development of this result requires an analysis of j_ν. Toward this end we introduce the unit vectors $\mathbf{u}_\alpha$ [see (VII.4.4*f*), deShalit and Feshbach (74)], whose z axis is taken along the direction of $\mathbf{q}$:

$$\mathbf{u}_0 = \frac{1}{q}\mathbf{q} \tag{2.101}$$

Then setting up a Cartesian coordinate system with unit vectors $\mathbf{u}_x$ and $\mathbf{u}_y$, one can define

$$\mathbf{u}_1 = -\frac{1}{\sqrt{2}}(\mathbf{u}_x + i\mathbf{u}_y) \tag{2.102}$$

$$\mathbf{u}_{-1} = \frac{1}{\sqrt{2}}(\mathbf{u}_x - i\mathbf{u}_y) \tag{2.103}$$

The *three-vector* $\mathbf{j}(\mathbf{q})$ can then be written:

$$\mathbf{j} = j_0\mathbf{u}_0^\dagger + j_1\mathbf{u}_1^\dagger + j_{-1}\mathbf{u}_{-1}^\dagger$$

The continuity equation for $\mathbf{j}(\mathbf{r})$,

$$\operatorname{div}\mathbf{j} + \frac{\partial\rho}{\partial t} = 0$$

becomes in momentum space

$$q_\mu j_\mu = 0$$

or

$$\mathbf{q}\cdot\mathbf{j} = \rho q_0 = q j_0$$

Therefore,

$$\mathbf{j} = j_1\mathbf{u}_1^\dagger + j_{-1}\mathbf{u}_{-1}^\dagger + \frac{q_0}{q}\rho(\mathbf{q})\mathbf{u}_0^\dagger \tag{2.104}$$

The three-current $\mathbf{j}$ is composed of two components orthogonal to $\mathbf{q}$ (the transverse components) and one along $\mathbf{q}$ (the longitudinal component). The magnitude of the last is proportionl to $\rho(\mathbf{q})$, which must be combined with the $\gamma_4 j_4$ contribution discussed earlier in this section, giving rise to a change in the kinematic factors only. We therefore focus on the contributions coming from the transverse components. These have been discussed in Chapter VIII of

deShalit and Feshbach (74). Here we shall follow the methods that have become traditional in electron–nuclear physics. One needs the expansion

$$\mathbf{u}_\lambda e^{i\mathbf{q}\cdot\mathbf{r}} = -\sum_{J=1}^{\infty}[2\pi(2J+1)]^{1/2} i^J\left[\lambda j_J(qr)\mathbf{Y}_{J\lambda}^{(\lambda)} + \frac{1}{q}\operatorname{curl}(j_J(qr)\mathbf{Y}_{JJ})\right] \qquad \lambda = \pm 1 \tag{2.105}$$

In this equation j_J is the spherical Bessel function, and‡

$$\mathbf{Y}_{Jl}^{(M)} \equiv \sum_{mm'} (lm1m'|JM)\, Y_{lm}\mathbf{u}_{m'} \tag{2.106}$$

From (2.104) we have

$$\begin{aligned} j_\lambda(q) = \mathbf{u}_\lambda\cdot\mathbf{j}(\mathbf{q}) &= \int \mathbf{j}(\mathbf{r})\cdot\mathbf{u}_\lambda e^{i\mathbf{q}\cdot\mathbf{r}}\, d\mathbf{r} \\ &= -\sum_{J\geqslant 1}[2\pi(2J+1)]^{1/2} i^J(\lambda T_{J\lambda}^{(\mathrm{mag})} + T_{J\lambda}^{\mathrm{el}}) \end{aligned} \tag{2.107}$$

where

$$T_{J\lambda}^{(\mathrm{mag})} \equiv \int \mathbf{j}(\mathbf{r})\cdot j_J(qr)\mathbf{Y}_{JJ}^{(\lambda)}\, d\mathbf{r} \tag{2.108}$$

and

$$T_{J\lambda}^{(\mathrm{el})} \equiv \frac{1}{q}\int \mathbf{j}(\mathbf{r})\cdot\operatorname{curl} j_J(qr)\mathbf{Y}_{JJ}^{(\lambda)}\, d\mathbf{r} \tag{2.109}$$

These quantities transform like tensors of rank J. Applying the Wigner–Eckart theorem yields

$$\langle J_F M_f|T_{J\lambda}^{(\mathrm{mag})}|J_i M_i\rangle = (-)^{J_f - M_f}\begin{pmatrix} J_f & J & J_i \\ -M_f & \lambda & M_i \end{pmatrix}(J_f\|T_J^{(\mathrm{mag})}\|J_i)$$

It is now possible using (2.107) to compute

$$\begin{aligned} &\frac{1}{2J_i+1}\sum_{\substack{M_i M_f \\ \lambda,\lambda'}}\langle J_f M_f|j_\lambda|J_i M_i\rangle\langle J_f M_f|j_{\lambda'}|J_i M_i\rangle^* \\ &\quad = \frac{2\pi}{2J_i+1}\left[\sum_J |(J_f\|T_J^{(\mathrm{mag})}\|J_i)|^2 + |(J_f\|T_J^{(\mathrm{el})}\|J_i)|^2\right] \end{aligned} \tag{2.110}$$

One can now complete the evaluation of (2.97) for the cross section in the

‡The derivation of (2.105) is straightforward when one realizes that $\mathbf{Y}_{JJ}^{(\lambda)}$ and $(1/q)\operatorname{curl} j_J(qr)\mathbf{Y}_{JJ}^{(\lambda)}$ form mutually orthogonal and normalized sets of vector wave functions on the unit sphere. Thus the coefficient of $\mathbf{Y}_{JJ}^{(\lambda)}$ in expansion (2.105) is given by $\int d\Omega\, \mathbf{Y}_{JJ}^{(\lambda)\dagger}\cdot\mathbf{u}_\lambda e^{i\mathbf{q}\cdot\mathbf{r}}$. The coefficient of the second term is $1/q\int d\Omega\, \mathbf{Y}_{JJ}^{(\lambda)\dagger}\cdot\operatorname{curl}(\mathbf{u}_\lambda e^{i\mathbf{q}\cdot\mathbf{r}})$.

center-of-mass frame. After some algebra it can be cast into the following form:

$$\frac{d\sigma}{d\Omega} = \sigma_M \left[\frac{q_\mu^4}{q^4} F_L^2(\mathbf{q}) + \left(\frac{1}{2} \frac{q_\mu^2}{q^2} + \tan^2 \frac{\vartheta}{2} \right) F_T^2(\mathbf{q}) \right] \tag{2.111}$$

where σ_M is the Mott cross section evaluated at the incident energy and

$$F_L^2 = \frac{4\pi}{2J_i + 1} \sum_{J=0} |(J_f \| \hat{M}_J^{(CO)}(\mathbf{q}) \| J_i)|^2 \tag{2.112}$$

and

$$F_T^2 = \frac{4\pi}{2J_i + 1} \sum_{J=1} \{ |(J_f \| \hat{T}_J^{(el)}(\mathbf{q}) \| J_i)|^2 + |(J_f \| \hat{T}_J^{(mag)}(\mathbf{q}) \| J_i)|^2 \} \tag{2.113}$$

Note that experimentally it is possible separately to determine F_L^2 and F_T^2 as functions of $\mathbf{q}$ by suitably choosing the experimental parameters. For example, if $\vartheta \sim \pi$, the cross section is dominated by $|F_T|^2$. Varying the incident energy will then yield $|F_T(\mathbf{q})|^2$. The matrix elements in (2.112) and (2.113) reduce to those obtained from photon excitation if $q = \omega$ [see Chapter VIII in deShalit and Feshbach (74)]. Inelastic electron scattering gives a much more complete picture by providing the q dependence for $q > \omega$ and, by Fourier inversion, the spatial dependence of the current as well as the charge distribution. The selection rules are identical with those of the photon case, namely

$$\mathbf{J}_f = \mathbf{J}_i + \mathbf{J}$$

with parity changes of $(-)^J$ for $\hat{T}^{(el)}$ and $\hat{M}^{(CO)}$ and $(-)^{J+1}$ for $\hat{T}^{(mag)}$.

The current density $\mathbf{j}$, to be inserted into (2.108) and (2.109) to obtain $\hat{T}^{(el)}$ and $\hat{T}^{(mag)}$ have been discussed in Chapter VIII of deShalit and Feshbach (74). The point-charge current as given by (VIII.2.3) and (VIII.2.4) in that reference is broken up into two components, a convection spin-independent current $\mathbf{j}_c$, and a spin-dependent magnetization current, $\mathbf{j}_m$:

$$\mathbf{j} = \mathbf{j}_c + \mathbf{j}_m$$

$$\mathbf{j}_c = e \sum_i \tfrac{1}{2}(1 + \tau_3(i)) \tfrac{1}{2} [\mathbf{v}_i \delta(\mathbf{r} - \mathbf{r}_i) + \delta(\mathbf{r} - \mathbf{r}_i)\mathbf{v}_i] \tag{VIII.2.3}$$

$$\mathbf{j}_m = \frac{e\hbar}{4m} \sum_i \tfrac{1}{2} [(g_n + g_p) + \tau_3(i)(g_p - g_n)] \operatorname{curl} [\boldsymbol{\sigma}_i \delta(\mathbf{r} - \mathbf{r}_i)] \tag{VIII.2.4}$$

The velocity $\mathbf{v}_i$ is defined by

$$\mathbf{v}_i = \frac{i}{\hbar} [H, \mathbf{r}_i] = \frac{\partial H}{\partial \mathbf{p}_i} \tag{VIII.2.5}$$

where H is the full Hamiltonian, including the electromagnetic terms.

However, nucleons have a finite nonzero size and have a structure. This has two consequences. First the delta functions in (VIII.2.3) and (VIII.2.4) must be replaced by form factors [see (VIII.3.8), deShalit and Feshbach (74)].

Second, the one-body operators of the equations above must be supplemented by two-body and higher-order operators whose physical origin lies in the meson exchange currents (MEC), which were mentioned briefly in Chapter VIII of deShalit and Feshbach (74). Currents are present whenever the nucleons in the nucleus exchange pions and other mesons such as the ρ and ω in the course of generating the nuclear force between the exchanging nucleons. The currents, known as *exchange currents*, will interact with an external electromagnetic field. The various contributions to that interaction are illustrated by Fig. 2.14. In Fig. 2.14*a* the electromagnetic wave is absorbed by a pion, indicated by a dashed line as the pion is exchanged. In Fig. 2.14*b*, the electromagnetic wave is absorbed by the nucleon, which may remain a nucleon. Or the γ-ray may make a $N, \bar{N}$ pair, the latter interacting with one of the nucleons to make a pion which is then picked up by the other nucleon. Or the γ-ray may simply excite one of the nucleons, creating a nucleon isobar which then exchanges a pion with the other nucleon, reverting to the nucleon in its ground state. The final two diagrams, Fig. 2.14*d* and *e*, involve the heavy mesons designated by M and M'. The results, appropriate for transitions in complex nuclei, are summarized in the review article by Donnelly and Sick (84), to which the reader is referred for details and references. The short-range contributions described by Fig. 2.14*d* and *c* are not included. The diagram involving the nucleon intermediate state (Fig. 2.14*b*) is dropped since this term is automatically included in the convection current term. One is therefore left with contributions from Fig. 2.14*c*, the antinucleon intermediate state in Fig. 2.14*b*, and the excited nucleon intermediate state (Fig. 2.14*c*). The last will include both the Δ and Roper nucleon resonances. Importantly, to order $(1/M)$ (M = nucleon mass), ρ_{exch} is zero. In addition, the leading term is an isovector. Gauge invariance is guaranteed to the extent that wave functions used arise from nucleon–nucleon interactions involving the same diagrams (Fig. 2.14) used in calculating the exchange currents. If the wave functions and exchange currents are not consistent, there can be considerable error since the operators involved are not positive definite and therefore are sensitive to the properties of the wave functions.

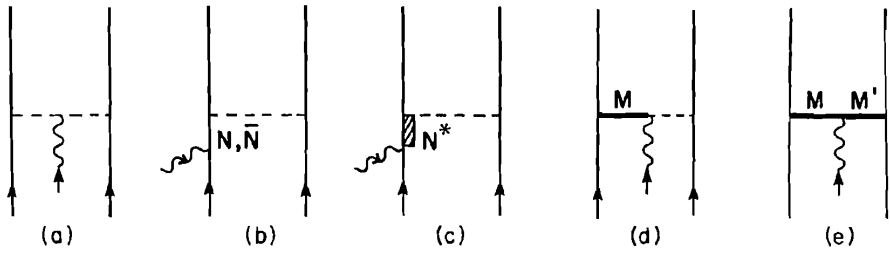

FIG. 2.14. Exchange currents.

H. Magnetic Elastic Electron Scattering

We turn now to the study of elastic magnetic electron scattering by nuclei [Donnelly and Sick (84)], from which $|F_T|^2$ of (2.111) and (2.113) may be determined as a function of the momentum transfer $\mathbf{q}$ and compared to nuclear model predictions. In contrast to the charge scattering, the magnetic scattering is sensitive to the properties of the valence nucleons since the net contribution of the core nucleons is zero in the spherical shell model description. The information on single-particle states obtained from nuclear transfer reactions is complementary since the responsible nuclear interaction differs from the electron interaction. In addition, magnetic elastic scattering is sensitive to neutron and proton distribution, as the equation for $\mathbf{j}_m$ [Eq. (VIII.2.4) in deShalit and Feshbach (74)] demonstrates.

Of course, the independent particle shell model is not correct. The deviations in the case of spherical nuclei are expressed in terms of configuration mixing, in which excited states of the core generated by the interaction with the valence nucleons are components of the total wave function. These interactions draw strength from the single-particle component, so that generally the magnetic elastic scattering crosssection is less than predicted by the extreme valence nucleon model. This fragmentation of the strength is clearly visible for deformed nuclei, where the Nilsson orbitals (which in the limit of zero deformation combine to yield a spherical orbital) play the dominant role. The magnetic elastic scattering by odd-A nuclei is sensitive to coupling of the valence particle with the deformed core. As expected, there is a reduction from the values predicted in the absence of this coupling. Much of the strength available in the spherical limit now goes into the inelastic scattering of the excited states built on the deformed ground state. Finally, in spherical cases for which the convection current $\mathbf{j}_c$, effects are dominant, the exchange current effects may be observable. We shall now illustrate these points with examples drawn from Donnelly's and Sick's (84) review. As we shall see, detailed information on the single-particle wave functions that these experiments yield is quite remarkable.

We first consider elastic magnetic scattering by a target nucleus with a spin J_0. It is assumed that the scattering caused by a single unpaired valence nucleon whose angular momentum is also J_0; the net angular momentum of the remaining nucleus equals zero. Moreover, we select those nuclei for which $J_0 = l + \frac{1}{2}$ (l = orbital angular momentum), that is, a stretched configuration. The largest multipole order is then $2J_0$. For this case the contribution of the convection current vanishes since it will be proportional to the square of the reduced matrix element $(\frac{1}{2} l J_0 \| Y_{2J_0} \| \frac{1}{2} l J_0)$. From (A.2.49) and (A.2.81) of deShalit and Feshbach (74) we have

$$(\tfrac{1}{2} l J_0 \| Y_{2J_0} \| \tfrac{1}{2} l J_0) \sim \begin{Bmatrix} J_0 & J_0 & 2J_0 \\ J_0 - \frac{1}{2} & J_0 - \frac{1}{2} & \frac{1}{2} \end{Bmatrix} \begin{pmatrix} J_0 - \frac{1}{2} & J_0 - \frac{1}{2} & 2J_0 \\ 0 & 0 & 0 \end{pmatrix}$$

The $6-j$ symbol vanishes since $\mathbf{J}_0 - \frac{1}{2} + \mathbf{J}_0 - \frac{1}{2} \neq 2\mathbf{J}_0$. As a consequence, only

the magnetization current, $\mathbf{j}_m$, contributes to $|F_T|^2$, it is, moreover, easy to show that

$$F_T \sim \int R^2(r) j_{(2J_0-1)}(qr) r^2 \, dr \tag{2.114}$$

where R is the radial function for the single-particle valence wave function. Inversion to obtain R^2 with the limitations discussed earlier with respect to the determination of the charge density is possible in principle‡

The discussion above assumes the validity of the single orbital description of the nuclear ground state. There will, of course, be configuration mixing. However, the additions to the single-particle contribution that can contribute to the $2J_0$ multipole moment transition must involve an orbital with $j \geqslant J_0$. Such an orbital with the correct parity will be available first, two shells above involving an excitation of $2\hbar\omega$. One therefore expects a very small amplitude for such a component in the ground state. Thus the form factor F_T will still be given by (2.114). The only effect on this transition of configuration mixing will be a reduction in the magnitude of F_T which can be related to the spectroscopic factor associated with that state as determined from nucleon inelastic scattering or from a transfer reaction.

For multipole moments of order less than $2J_0$, configuration mixing can have a large effect. This is particularly true when the configuration added is one that would readily be excited in an inelastic collision. Under those circumstances there will be interference between the strong single-particle term and the added configuration. The result will be to reduce the value of F_T, since some of the single-particle strength will be lost to inelastic channels. Obviously, states of the core that can be strongly excited play an important role.

Finally, experimentally the contribution of the very largest possible multipole moment will be very visible in the large q domain. The contribution of the moments of lower order will decrease rapidly for large enough momentum transfer q. However, this domination by the large multipole moment does not persist for a sufficiently large range of q at the low-q side, so that the inversion indicated by (2.114) is not feasible.

Many of these conclusions are exemplified by magnetic elastic scattering from ^{17}O. Because of the close agreement of the magnetic moment of ^{17}O with the single-particle Schmidt value, it has been thought that this was a good example of a valence nucleon (in this case a neutron in a $d_{5/2}$ state) moving in the field of an ^{16}O core. As illustrated in Fig. 2.15, we see that the single-particle

‡*Note*: Use the result

$$\operatorname{curl}(j_J \mathbf{Y}_{JJ}) = -i\left(\frac{J}{2J+1}\right)^{1/2} j_{J+1}\mathbf{Y}_{J,J+1} + i\left(\frac{J+1}{2J+1}\right)^{1/2} j_{J-1}\mathbf{Y}_{J,J-1}$$

and (A.2.49) and (A.2.81).

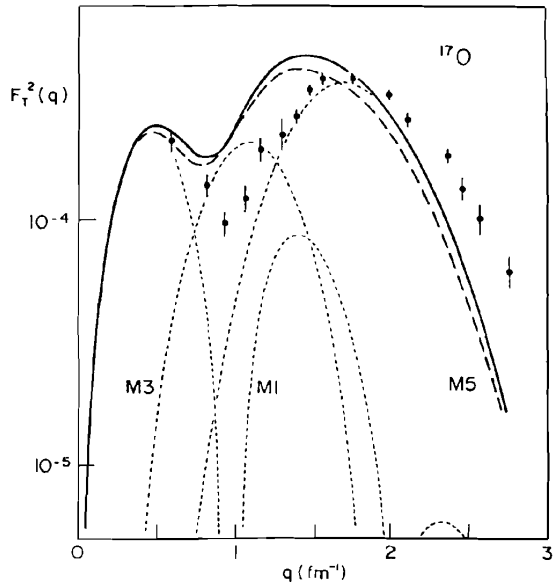

FIG. 2.15. The ^{17}O data of Hynes, Miska, et al. (79) are compared to prediction of the extreme single-particle model calculated using a harmonic oscillator wave function (solid curve). The dashed curve is calculated using a .Woods–Saxon radial wave function. [From Hynes, Miska, et al. (79).]

model greatly overestimates $|F_T|^2$ for values of q between about 0.9 and 1.8 fm^{-1} and underestimates $|F_T|^2$ for greater values of q. When configuration mixing is introduced phenomenologically [Burzynski, Baumgartner, et al. (83)], one obtains Fig. 2.16. The contribution of the MEC is estimated theoretically. The M5 and M1 components are very close to the predictions of the single-particle model. This is expected for M5 and the low-q values of M1. However, the M3 component is strongly reduced, indicating the effect of configuration mixing with core excited states. It was pointed out by Zamick (78) and examined in detail by Bohannon, Zamick, and Moya de Guerra (80) that the admixtures induced by an E2 M1 excitation of the nucleus will have a strong overlap through the M3 multipole with the single-particle orbital. This reduced the M3 moment by a factor of 2 [see also Arima, Horikawa, et al. (78)]. This excitation will not affect the M1 or M5 multipole.

Configuration mixing in terms of spherical nuclear wave function is very large for deformed nuclei. The effects described above are present, for example, for magnetic elastic scattering by ^{25}Mg. In Fig. 2.17, the results using a spherical single-particle wave function for the valence neutron are compared with the results obtained using a Nilsson orbital wave function, and with experiment. We observe a general reduction from the spherical case. The shape of the M5 form factor is not much changed, but the M3 form factor is greatly reduced.

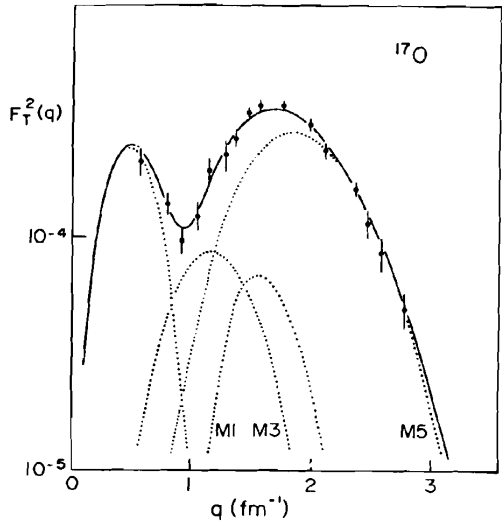

FIG. 2.16. The ^{17}O data of Hynes, Miska, et al. (79) corrected for the contribution of MEC, are compared to the fit of Burzynski, Baumgartner et al. (83) calculated using a Woods–Saxon radial wave function. [From Donnelly and Sick (84).]

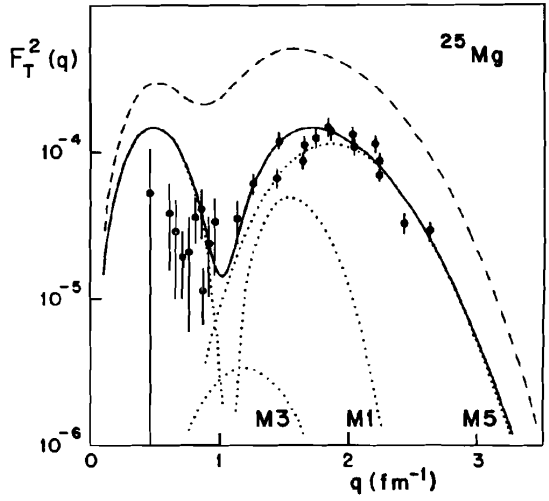

FIG. 2.17. The ^{25}Mg magnetic form factor is shown for the ESPM (dashed curve) and the Nilsson model (solid and dotted curves), all calculated using harmonic oscillator radial wave functions ($b = 1.63$ fm). [From Donnelly and Sick (84).]

The major lesson to be learned from these examples is that configuration mixing must be taken into account before a quantitative agreement between theory and experiment is possible. The wave functions are rarely describable by the naive independent-particle model. Once configuration mixing is taken into account and occasionally, the effect of exchange currents included (with a considerable error $\sim 50\%$), agreement with experiment is obtained. (Note that the comparisons with experiment are made on semilog plots.)

Parenthetically, the data on the M1 transition as well as the isoscalar and isovector magnetic moment and the Gamow–Teller matrix element as obtained from β decay and (p,n) reactions have been analyzed for nuclei in the s–d shell by Brown and Wildenthal and their colleagues [Brown (86)]. The wave functions are obtained by treating the two-body residual interaction matrix elements as empirical parameters which are determined by the ground and excited states in the s–d shell. [see Brown (86) for a review.] The resultant wave functions can then be used in the evaluation of the transition matrix elements. Very briefly, it is found possible to fit the data mentioned above by assuming an M1 operator that varies smoothly with A. The free nucleon M1 operator is [see Chapter VIII] is deShalit and Feshbach (74)]

$$M1 = g_s \mathbf{s} + g_l \mathbf{l}$$

To this operator one adds a "correction"

$$g_s[\delta_s \mathbf{s} + \delta_l \mathbf{l} + \delta_p(\sqrt{8\pi}[Y_2 \times s]^{(1)})]$$

where δ_s, δ_l, and δ_p are parameters. The third term includes configuration mixing of the type suggested by Zamick (78).

The parameters are found empirically to vary smoothly with A.

I. Quasi-Elastic Scattering

In this section the processes in which one or more nucleons are ejected from the nucleus by the incident electron are discussed. The term *quasi-elastic scattering* is used because it is thought that because of the high electron energy, nucleon knockout is the consequence of the elastic collision of the electron, with a nucleon in the nucleus having a momentum $\hbar\mathbf{k}$. As a consequence, it should be possible to determine the nucleon momentum distribution by observing the angular and energy distribution of the final electron. This hope is encouraged by the success of the analogous experiment determining the momentum distribution of the electrons in an atom. However, as we shall see, there are important limitations. It is convenient to mention one of these now. In an inclusive experiment, $(e,e'X)$, in which only the scattered electron is observed, it is possible that more than one nucleon is ejected from the nucleus. Moreover, generally the final nucleus may be left in a highly excited state. In

the multiple scattering picture of Chapter II, the nucleon initially struck by the electron will be scattered by the other nucleons in the nucleus, thereby exciting the residual nucleus and possible ejecting a second nucleon.

The kinematics implied by the simple single-nucleon knockout has been discussed in Chapter I [see (I.3.9)]. A brief review is in order. An incident electron with momentum $\hbar\mathbf{k}_1$ is scattered by a nuclear nucleon of momentum $\hbar\mathbf{k}$, thus acquiring a momentum $\hbar\mathbf{k}_2$ (see Fig. 2.18). The momentum and energy transfer to the nucleon is $\hbar\mathbf{q} = \hbar(\mathbf{k}_1 - \mathbf{k}_2)$ and $\hbar\omega$, respectively. The emerging nucleon has a momentum $\hbar(\mathbf{k} + \mathbf{q})$. Nonrelativistic conservation of energy requires

$$\frac{\hbar^2}{2m^*}(\mathbf{k} + \mathbf{q})^2 = \frac{\hbar^2 k^2}{2m^*} + \hbar\omega - \varepsilon_b \tag{2.115}$$

where ε_b is the minimum energy needed to remove the nucleon from the nucleus and m^* is the effective mass assumed to be the same for the target and the ejected nucleon. [See, however, the discussion of the effective mass in Chapter V, where we find that the effective mass is a function of momentum and energy).] Solving the equation above for $\hbar\omega$, we obtain

$$\hbar\omega = \varepsilon_b + \frac{\hbar^2}{2m^*}(2\mathbf{k}\cdot\mathbf{q} + q^2) \tag{2.116}$$

Hence $\hbar\omega$ is bounded:

$$\varepsilon_b + \frac{\hbar^2}{2m^*}(-2k_F q + q^2) < \hbar\omega < \varepsilon_b + \frac{\hbar^2}{2m^*}(2k_F q + q^2)$$

The quasi-elastic peak will thus have a width given approximately by $(\hbar^2/m^*)k_F q$. The spreading is a consequence of the Fermi motion of the target nucleon. The effects of the nucleon interactions are crudely taken into account through the use of the effective mass. Examples of the quasi-elastic peak for three target nuclei are given in Fig. 2.19. The reader can check that the width is given approximately by $(\hbar^2/m)k_F q$.

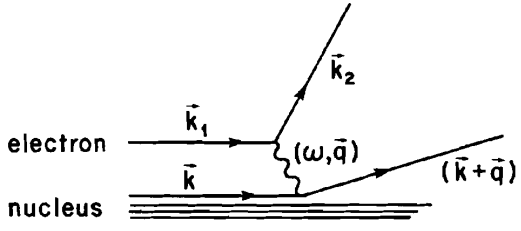

FIG. 2.18. Diagram for the $(e, e'p)$ process.

The inclusive differential cross section for the $(e, e'x)$ reaction can be obtained directly from (2.111). It is

$$\frac{d\sigma}{d\Omega_2 dE_2} = \sigma_M \left[\frac{q_\mu^4}{q^4} R_L + \left(\frac{1}{2} \frac{q_\mu^2}{q^2} + \tan^2 \frac{\vartheta}{2} \right) R_T \right] \tag{2.117}$$

where

$$R_L = \sum |\langle f | \rho(\mathbf{q}) | i \rangle|^2 \delta(E_i - E_f) \tag{2.118a}$$

and

$$R_T = \sum [|\langle f | j_1 | i \rangle|^2 + |\langle f | j_{-1} | i \rangle|^2] \delta(E_i - E_f) \tag{2.118b}$$

In these equations the sum is taken over all final states designated by f and averaged over the initial states designated by i. The delta function indicates that only those final states that conserve energy are to be included in the sum.

The sum includes an integral over the continuum in the case of particle emission. For example, for the case of proton emission, $(e, e'p)$,

$$R_L = \int \sum |\langle f_N | \rho(\mathbf{q}) | i \rangle|^2 \delta \left(\hbar\omega - \frac{\hbar^2}{2m} \kappa^2 - (E_N - E_A) - E_R \right) \frac{d\boldsymbol{\kappa}}{(2\pi)^3} \tag{2.119}$$

where $\hbar\boldsymbol{\kappa}$ is the momentum of the emitted proton and E_R is the recoil energy. The sum is now over *residual* nuclear states, which in the case of closed-shell nuclei, are one-hole states. $E_N - E_A$ is the excitation energy of those states. To obtain the *exclusive* cross section, one drops the integral, and dividing (2.117) by $d\boldsymbol{\kappa}$ one obtains an expression for $d\sigma/(d\Omega_2 dE_2)(d\Omega_\kappa dE_\kappa)$.

Employing the model illustrated in Fig. 2.18, (2.119) becomes

$$R_L = \int \sum |\langle f_N | \rho(\mathbf{q}) | i \rangle|^2 \delta \left(\frac{\hbar^2 k^2}{2m^*} + \hbar\omega - \varepsilon_b - \frac{\hbar^2 (\mathbf{k} + \mathbf{q})^2}{2m^*} \right) \frac{d\mathbf{k}}{(2\pi)^3} \tag{2.120}$$

Note the shift from $d\boldsymbol{\kappa}$ to $d\mathbf{k}$ which is possible in the model because $\boldsymbol{\kappa}$ and $\mathbf{k}$ are linearly related. But $\mathbf{k}$ refers to the initial nucleon momenta, so that R_L depends on the nucleon momentum distribution. A first overview of the quasi-elastic process is obtained by using the Fermi-gas model. Then

$$R_L = \frac{3Z}{4\pi k_F^3} \int_0^{k_f} d\mathbf{k} \theta(k_F - k) \delta \left(\frac{\hbar^2 k^2}{2m^*} + \hbar\omega - \varepsilon_b - \hbar^2 \frac{(\mathbf{k} + \mathbf{q})^2}{2m^*} \right) \tag{2.121}$$

where $\theta(x)$ is the unit function, $\theta(x) = 1$, $x > 0$, $\theta(x) = 0$, $x < 0$. The integration can be readily carried out. The results are given by deForest and Walecka (66) or Donnelly and Walecka (75). Here we note only that for large $q (> 2k_F)$, R_L is proportional to $1/q\{1 - [(\hbar\omega - \varepsilon_b)m^*/k_F q + q/2k_F]^2\}$, a parabolic function of $(\hbar\omega - \varepsilon_B)$.

Calculations by Moniz, Sick, et al. (71) using the Fermi-gas model with ε_b and k_F empirical parameters have been compared with the experimental results (the target nucleus is ^{12}C) shown in Fig. 2.19. The agreement is excellent and the empirical values of ε_B and k_F reasonable (see Fig. I.3.4). However, when the longitudinal and transverse cross sections are separately compared with experiment, this nice agreement disappears. That comparison [Ciofi degli Atti and Salmè (84)] is shown in Figs. 2.20 and 2.21. One sees (the dotted–dashed curve) that the Fermi gas model overestimates the longitudinal cross section by a large factor; agreement with the transverse cross section is good. When a more realistic nuclear model is employed (i.e., the Hartree–Fock model) and final state interactions of the emerging nucleon are included (the solid line), excellent agreement with the longitudinal cross section is obtained.

The expression (2.121) exhibits the property of *scaling* [see West (75); Sick, Day, and McCarthy (80); Sick (87)]. The δ-function factor can be rewritten as follows:

$$\delta\left(\frac{\hbar^2 k^2}{2m^*} + \hbar\omega - \varepsilon_b - \frac{\hbar^2(\mathbf{k}+\mathbf{q})}{2m^*}\right) = \delta\left(\hbar\omega - \varepsilon_b - \frac{\hbar^2 q^2}{2m^*} - \frac{\hbar^2}{m^*}\mathbf{k}\cdot\mathbf{q}\right)$$

$$= \frac{m^*}{\hbar^2 q}\delta\left(\frac{m^*}{\hbar^2 q}(\hbar\omega - \varepsilon_b) - \frac{q}{2} - k_\parallel\right)$$

$$= \frac{m^*}{\hbar^2 q}\delta(y - k_\parallel) \tag{2.122}$$

where $k_\parallel$ is the component of $\mathbf{k}$ parallel to $\mathbf{q}$ and

$$y \equiv \frac{m^*}{\hbar^2}\frac{(\hbar\omega - \varepsilon_b) - q^2/2}{q} \tag{2.123}$$

$$= \frac{m^*}{2\hbar^2}\frac{[\sqrt{2(\hbar\omega - \varepsilon_b)} - q][\sqrt{2(\hbar\omega - \varepsilon_b)} + q]}{q}$$

$$\xrightarrow[\omega\to\infty]{q\to\infty} \frac{m^*}{2\hbar^2}[\sqrt{2(\hbar\omega - \varepsilon_b)} - q] \tag{2.124}$$

Inserting (2.122) into (2.121) for R_L, we observe that qR_L is a function of y only. Thus all experiments performed at identical values of y by choosing the appropriate ω and q should, according to the Fermi model, have identical values of qR_L.

Although the results above are instructive, it is necessary to go beyond the Fermi gas model and employ a more accurate description of the nucleus. Toward that end we rewrite R_L as follows:

$$R_L = \sum\langle i|\rho^\dagger(\mathbf{q})|f\rangle\langle f|\rho(\mathbf{q})|i\rangle\delta(E_i - E_f)$$

$$= \sum\langle i|\rho(\mathbf{q})\delta(E_i - H)|f\rangle\langle f|\rho(\mathbf{q})|i\rangle \tag{2.125}$$

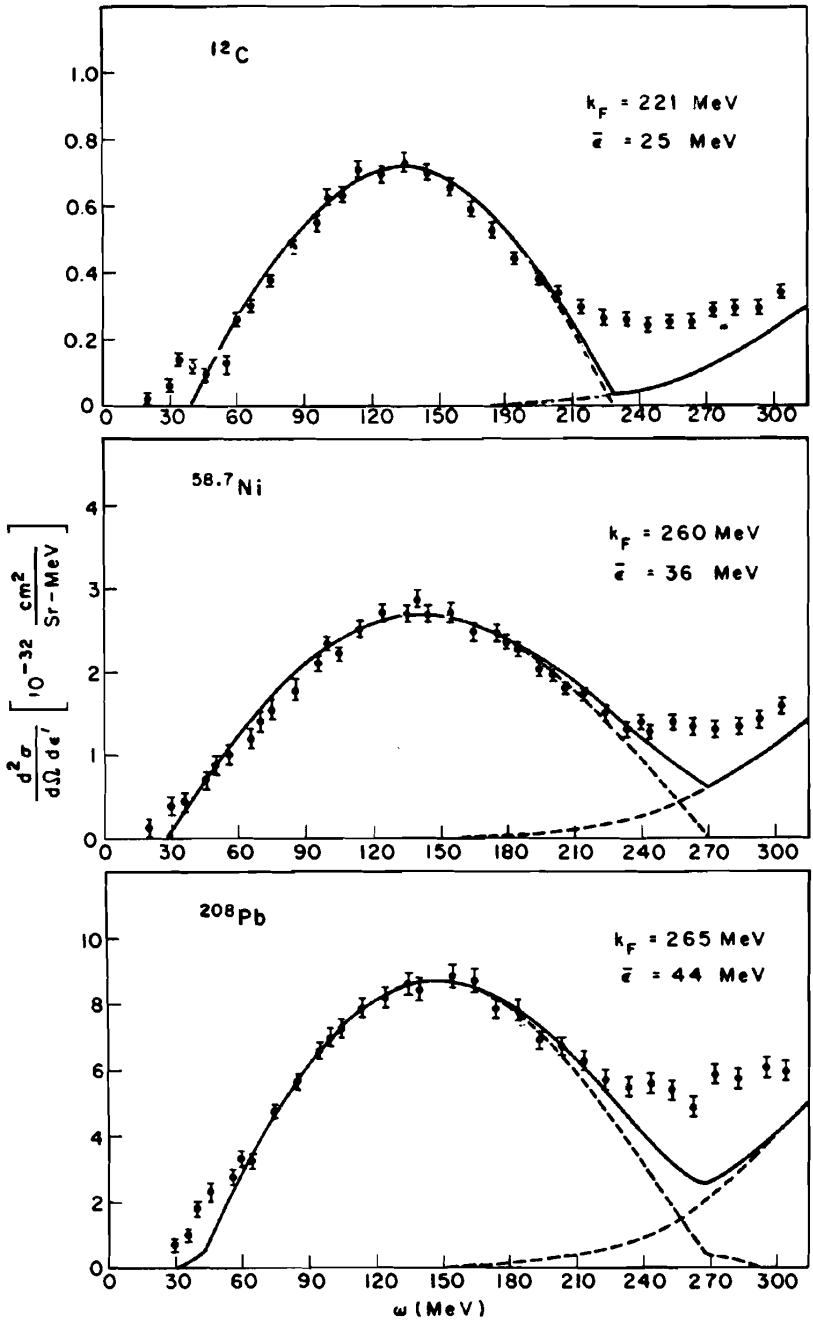

FIG. 2.19. Cross sections for quasi-elastic electron scattering. The electron's energy is 500 MeV. The scattered electron is observed at 60°. The solid lines are the results of Fermi-gas calculations with parameters indicated on the figure. [From Moniz, Sick, et al. (71).]

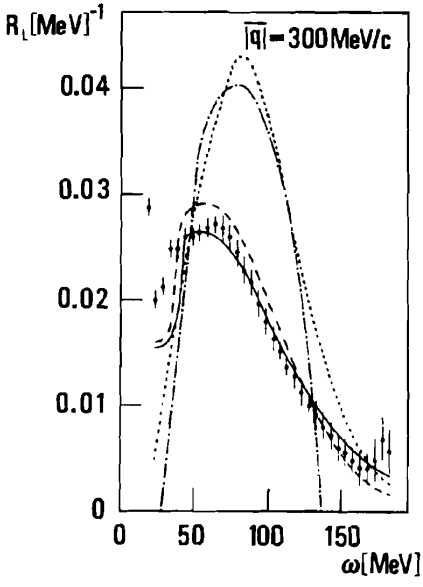

FIG. 2.20. Experimental and theoretical longitudinal response functions. Dotted curve, Hartree–Fock results without final-state interaction; dashed curve, Hartree–Fock results with final-state interaction, optical model potential real, solid curve, Hartree–Fock results with final-state interaction, optical model potential complex; Dashed–dotted curve, Fermi-gas result. [From Ciofi degli Atti and Salmè (84).]

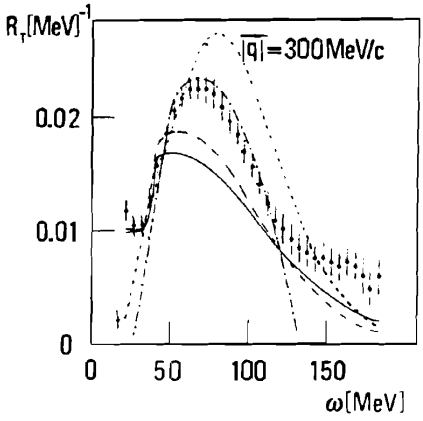

FIG. 2.21. Same as Fig. 2.20 for the transverse response function. [From Ciofi degli Atti and Salmè (84).]

The Hamiltonian can be decomposed into the Hamiltonian H_N for the residual nucleus plus the Hamiltonian H_0 for the emerging nucleon, including its interaction with the residual nucleus:

$$H = H_0 + H_N$$

where

$$H_0 = T + V$$

At this point it is convenient to make approximations that are valid in the high-energy regime. A similar set of approximations are described in Chapter II on multiple scattering. First we replace V, which is in fact a many-body operator, by an effective optical potential of the nucleon moving in the field of the residual nucleus. Second, H_N is replaced by an average energy $\bar{\varepsilon}$, the excitation energy of the residual nucleus. Finally, the initial energy E_i is taken to be the ground-state energy of the target nucleus, taken to be zero, plus the energy transferred by the incident electrons to the nuclear system $\hbar\omega$. With these assumptions, R_L becomes

$$R_L = \sum_f \langle i|\rho^\dagger(\mathbf{q})\delta(\hbar\omega - \bar{\varepsilon} - H_0)|f\rangle\langle f|\rho(\mathbf{q})|i\rangle$$

Performing the sum over the final states yields

$$R_L = \langle i|\rho^\dagger(\mathbf{q})\delta(\hbar\omega - \bar{\varepsilon} - H_0)\rho(\mathbf{q})|i\rangle \tag{2.126}$$

Using the identity

$$\mathrm{Im}\frac{1}{\hbar\omega - \bar{\varepsilon} - H_0 + i\varepsilon} = -\frac{1}{\pi}\delta(\hbar\omega - \bar{\varepsilon} - H_0) \tag{2.127}$$

one has

$$R_L = -\frac{1}{\pi}\mathrm{Im}\left\langle i\left|\rho^\dagger(\mathbf{q})\frac{1}{\hbar\omega - \bar{\varepsilon} - H_0 + i\varepsilon}\rho(\mathbf{q})\right|i\right\rangle \tag{2.128}$$

We now approximate the Green's function in this expression by its eikonal limit [see Gurvitz and Rinat (87)]:

$$\left\langle \mathbf{r}\left|\frac{1}{\hbar\omega - \bar{\varepsilon} - H_0 + i\varepsilon}\right|\mathbf{r}'\right\rangle = -\frac{im}{\hbar^2 K}e^{iK(z-z')}\delta(\mathbf{b}-\mathbf{b}')\theta(z-z')e^{(1/2iK)\int_{z'}^{z}U(\zeta,\mathbf{b})d\zeta} \tag{2.129}$$

where

$$K^2 = \frac{2m}{\hbar^2}(\hbar\omega - \bar{\varepsilon}) \qquad \text{and} \qquad U = \frac{2m}{\hbar^2}V$$

Note. To derive this result, note that

$$\left\langle \mathbf{r}\left|\frac{1}{\hbar\omega - \bar{\varepsilon} - H_0 + i\varepsilon}\right|\mathbf{r}'\right\rangle = G(\mathbf{r},\mathbf{r}')$$

satisfies

$$\left(\hbar\omega - \bar{\varepsilon} + \frac{\hbar^2}{2m}\nabla^2 - V\right)G = \delta(\mathbf{r}-\mathbf{r}') = \delta(z-z')\delta(\mathbf{b}-\mathbf{b}).$$

Let

$$G = e^{iK(z-z')}g$$

Then approximately (neglecting $\nabla^2 g$ compared to $2K\,\partial g/\partial z$)

$$2iK\frac{\partial g}{\partial z} - Ug = \frac{2m}{\hbar^2}\delta(z-z')\delta(\mathbf{b}-\mathbf{b})$$

Equation (2.129) is obtained by integrating this first-order equation.

Inserting (2.129) and

$$\rho(\mathbf{q}) = \sum_{r_i} e^{i\mathbf{q}\cdot\mathbf{r}_i} \Rightarrow Ze^{i\mathbf{q}\cdot\mathbf{r}}$$

into (2.128) for R_L, one finds that

$$R_L = \frac{mZ^2}{\pi\hbar^2 K}\,\mathrm{Re}\int d\mathbf{r}\int d\mathbf{r}'\,\rho(\mathbf{r},\mathbf{r}')e^{i\mathbf{q}\cdot(\mathbf{r}'-\mathbf{r})}e^{iK(z-z')}\delta(\mathbf{b}-\mathbf{b}')\theta(z-z')e^{(1/2iK)\int_z^z dz U(\zeta,\mathbf{b})}$$

where $\rho(\mathbf{r},\mathbf{r}')$ is the density matrix:

$$\rho(\mathbf{r},\mathbf{r}') = \int \psi^*(\mathbf{r},\mathbf{r}_2,\ldots)\psi(\mathbf{r}',\mathbf{r}_2,\ldots)d\mathbf{r}_2\cdots$$

[see (2.88) et seq.].

Carrying out the integrations over $\mathbf{b}$ and choosing the z direction to be along $\mathbf{q}$, we have

$$R_L = \frac{mZ^2}{\pi\hbar^2 K}\,\mathrm{Re}\left[\int_{-\infty}^{\infty} d\mathbf{b}\,dz\int_{-\infty}^{\infty} dz'\,\rho(z,\mathbf{b};z'\mathbf{b})e^{i(K-q)(z-z')}\theta(z-z')e^{(i/2K)\int_z^z U dz}\right] \tag{2.130}$$

Scaling no longer prevails since the final factor that reflects the final-state interaction is not a function of $K-q$. The exponent can be expanded in a series in $(K-q)/q$, so that scaling is approached when $(K-q)/q \ll 1$. The simple Fermi-gas model leading to (2.121) requires further approximation. More accurately, the quasi-elastic inclusive electron scattering probes the density matrix $\rho(z,\mathbf{b};z'\mathbf{b})$.

Problem. Using expansion, (2.88) shows that in the absence of final-state interaction effects

$$R_L = \mathrm{Re}\int d\mathbf{b}\int_{-\infty}^{\infty} dz \int_{-\infty}^{\infty} dz'\,\rho(z,\mathbf{b};z'\mathbf{b})e^{i(K-q)(z-z')}\theta(z-z')$$

$$= \sum \kappa_\lambda \,\mathrm{Re}\frac{1}{2\pi i}\int d\mathbf{b}\int_{-\infty}^{\infty}\frac{dt}{t+i\varepsilon}|\bar{\omega}_\lambda(t+K-q),\mathbf{b})|^2$$

$$= -\tfrac{1}{2}\sum \kappa_\lambda \int d\mathbf{b}|\bar{\omega}_\lambda(K-q,\mathbf{b})|^2$$

$$= -\frac{1}{8\pi^2}\sum \kappa_\lambda \int d\mathbf{s}|\Omega_\lambda(K-q,\mathbf{s})|^2$$

where

$$\bar{\omega}_\lambda(K-q,\mathbf{b}) = \int_{-\infty}^{\infty} dz\, e^{i(K-q)z}\omega(z,\mathbf{b})$$

and

$$\Omega_\lambda = \int e^{-i\mathbf{s}\cdot\mathbf{b}}e^{i(K-q)z}\omega_\lambda(z,\mathbf{b})\,d\mathbf{r}$$

In addition, scaling is no longer possible when relativistic effects are taken into account [see Alberico et al (88)]. Nevertheless, it is clearly exhibited experimentally, as one can see from Fig. 2.22. Scaling is observed for $y<0$ but is not obtained for $y>0$. Similar results have been obtained for ^{4}He, ^{12}C, ^{27}Mg, and ^{197}Au [Day et al. (88)]. The lack of scaling for $y>0$ is presumably because the reaction mechanism for large energy transfers is no longer primarily the ejection of a single nucleon.

Note. The potential U in (2.130) is obtained by fitting the elastic scattering data. It is a possibly useful property of the eikonal approximation that one can express the exponential involving U in terms of the nuclear scattering amplitude of a nucleon moving in the $\mathbf{q}$ direction. We recall from Chapter II [Eq. (II.5.8)] that the *elastic* scattering amplitude is, in the eikonal approximation, given by

$$f(\mathbf{Q}) = -\frac{1}{4\pi}\int d\mathbf{r}\,e^{i\mathbf{Q}\cdot\mathbf{r}}U(\mathbf{r})e^{-(i/2K)\int_{-\infty}^{z}U(\zeta,\mathbf{b})d\zeta} \tag{2.131}$$

Using the Fourier integral theorem, one can invert the equation to obtain

$$U(\mathbf{r})e^{-(i/2K)\int_{-\infty}^{z}U(\zeta,\mathbf{b})d\zeta} = -\frac{4\pi}{(2\pi)^3}\int d\mathbf{Q}\,f(\mathbf{Q})e^{-i\mathbf{Q}\cdot\mathbf{r}}$$

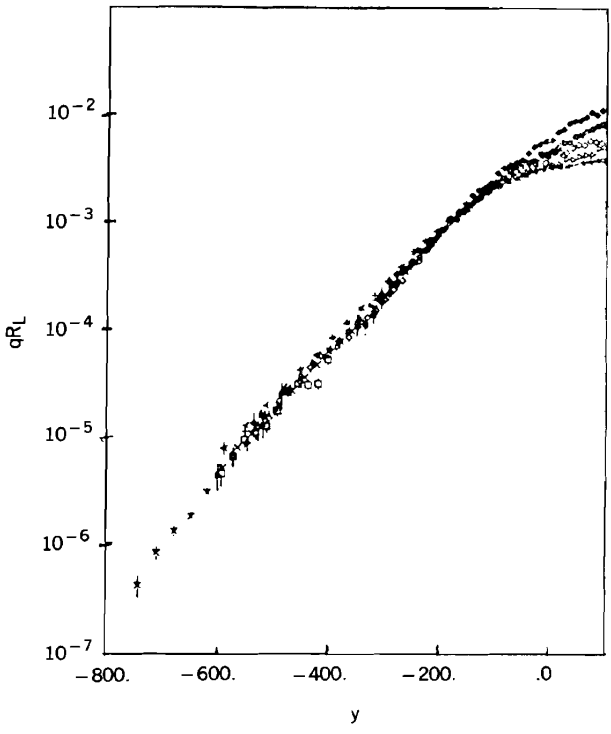

FIG. 2.22. See (2.123) et seq. [From Sick (81).]

To remove the prefactor $U(\mathbf{r})$, integrate both sides of the equation from zero to z. One obtains

$$2iK[e^{-(i/2K)\int_{-\infty}^{z}U(\zeta,\mathbf{x})d\zeta}-e^{-(i/2K)\int_{-\infty}^{0}U(\zeta,\mathbf{b})d\zeta}]=-\frac{4\pi i}{(2\pi)^3}\int d\mathbf{Q}f(\mathbf{Q})e^{-i\mathbf{Q}\cdot\mathbf{b}}\frac{e^{-iQ_lz}-1}{Q_l}$$

so that

$$e^{-(i/2K)\int_{-\infty}^{z}U(\zeta,\mathbf{b})d\zeta}=e^{-(i/2K)\int_{-\infty}^{0}U(\zeta,\mathbf{b})d\zeta}-\frac{1}{(2\pi)^2K}\int d\mathbf{Q}f(\mathbf{Q})e^{-i\mathbf{Q}\cdot\mathbf{b}}\frac{e^{-iQ_lz}-1}{Q_l}$$

where Q_l is the component of $\mathbf{Q}$ in the $\mathbf{q}$ direction. The desired quantity

$$e^{-(i/2K)\int_{z}^{z'}U(\zeta,\mathbf{b})d\zeta}=\frac{e^{-(i/2K)\int_{-\infty}^{0}Ud\zeta}-[1/(2\pi)^2K]\int d\mathbf{Q}f(\mathbf{Q})e^{-i\mathbf{Q}\cdot\mathbf{b}}(e^{-iQ_lz}-1)/Q_l}{e^{-(i/2K)\int_{-\infty}^{0}Ud\zeta}-[1/(2\pi)^2K]\int d\mathbf{Q}f(\mathbf{Q})e^{-i\mathbf{Q}\cdot\mathbf{b}}(e^{-iQ_lz'}-1)/Q_l} \tag{2.132}$$

From this equation one obtains

$$e^{-(i/2K)\int_{-\infty}^{0} U(\zeta,\mathbf{b})d\zeta} - \frac{1}{(2\pi)^2 K}\lim_{z'\to\infty}\int d\mathbf{Q} f(\mathbf{Q})\frac{e^{-iQ_l z'}-1}{Q_l} = 1$$

or

$$e^{-(i/2K)\int_{-\infty}^{0} U(\zeta,\mathbf{b})d\zeta} = 1 - \frac{i}{4\pi K}\int d\mathbf{Q} f(\mathbf{Q}_T, 0)e^{-i\mathbf{Q}\cdot\mathbf{b}} \tag{2.133}$$

where $\mathbf{Q}_T$ is the component of $\mathbf{Q}$ perpendicular to $\mathbf{q}$. Substituting in (2.132) yields the desired expression:

$$e^{-(i/2K)\int_{z}^{\infty} U(\zeta,\mathbf{b})d\zeta}$$

$$= \frac{1-(i/4\pi K)\int d\mathbf{Q}_T f(\mathbf{Q}_T,0)e^{-i\mathbf{Q}\cdot\mathbf{b}} - (1/4\pi^2 K)\int d\mathbf{Q} f(\mathbf{Q})e^{-i\mathbf{Q}\cdot\mathbf{b}}[(e^{-iQ_l z}-1)/Q_l]}{1-(i/4\pi K)\int d\mathbf{Q}_T f(\mathbf{Q}_T,0)e^{-i\mathbf{Q}\cdot\mathbf{b}} + (1/4\pi^2 K)\int d\mathbf{Q} f(\mathbf{Q})e^{-i\mathbf{Q}\cdot\mathbf{b}}[(e^{-iQ_l z'}-1)/Q_l]} \tag{2.134}$$

Another procedure valid at high energy begins with the relation

$$G = G_0 + G_0 \mathscr{T} G_0$$

where $G^{-1} = E + i\varepsilon - H$ and $G_0^{-1} = E + i\varepsilon - H_N$, $H = H_N + V$, and $\mathscr{T}$ is the transition matrix for the scattering of a proton by the $(A-1)$ nucleus. If in the second term one approximates G_0 by its energy on the energy-shell component, $\mathscr{T}$ will involve reaction amplitudes whose corresponding cross sections can be obtained from experiment.

J. The Reaction $(e, e'N)$[‡]

The reaction discussed in the preceding section is referred to as an *inclusive* reaction since only the emerging electron is observed. Effectively, therefore, all possible final states contribute to the cross section. In this section the reaction $(e, e'N)$, where N is a nucleon, is considered. This is an *exclusive* reaction since only one final system is observed. Such measurements are coincidence experiments; that is, both the final electron and ejected nucleon momenta and energy are measured. The experimental arrangement is illustrated schematically in Fig. 2.23. The shaded plane is the scattering plane containing the incident $\mathbf{k}_i$ and final momenta $\mathbf{k}_f$ of the electron. The unshaded plane contains the momentum transfer $\mathbf{q}$ and the emergent proton whose momentum makes an angle θ_p with respect to $\mathbf{q}$. The angle between the two planes is ϕ_p. In a typical experiment the energies of the emerging electron and proton are measured.

[‡]Dieperink and DeForest (75); DeForest (67); Co' et al. (87).

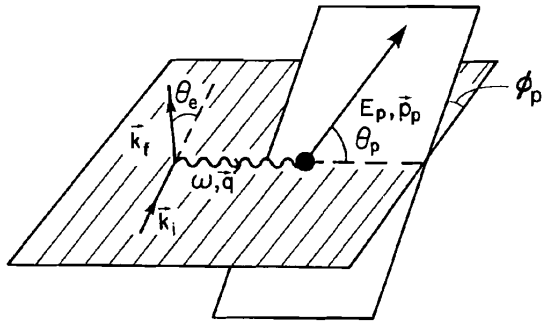

FIG. 2.23. Diagram for the $(e,e'p)$ reaction.

Their sum will not equal the incident electron energy since some of the energy has gone into the excitation of the residual nucleus. The difference

$$E_m = \hbar\omega - E_p - (E^{(f)}_{A-1} - E_A) - E_R \tag{2.135}$$

is referred to as the missing energy or the removal energy. Here E_R is the recoil energy of the residual nucleus, while $E^{(f)}_{A-1} - E_A$ is the excitation energy for the excitation of a final state E_f of the $A-1$ nucleus. If the cross section is plotted as a function of the missing energy, one will see relatively sharp peaks which can be identified with single hole state. An example is presented in Fig. 2.24.

In addition, one can also determine the cross section as a function of the missing momentum. In the Born approximation in which the emerging proton wave function is taken as a plane wave with momentum $\mathbf{p}$, the longitudinal response function, the important factor in these experiments becomes

$$R_L = \sum_f |\phi_f(\mathbf{p}_p - \mathbf{q})|^2 \delta(\hbar\omega - E_p - (E^{(f)}_{A-1} - E_A) - E_R) \tag{2.136}$$

where $\phi_f(\mathbf{p}_p - \mathbf{q})$ is the wave function of the hole state of the final nucleus in momentum space. This result suggests that determining the cross section in the energy domain where the delta function condition is satisfied will yield the momentum distribution of the hole state. Note that $\mathbf{p}_p - \mathbf{q}$ is the recoil momentum of the target nucleus. It is also referred to as the missing momentum p_m. This is illustrated in Fig. 2.25. We see the characteristic shapes of a p and an s single-particle nucleon wave function emerges. Note the differing ranges of E_m, the missing energy for the two cases. The dotted–dashed curve follows from (2.136) using the Elton–Swift (67) wave function. A better approximation to R_L uses the DWA. The matrix element $\langle f|\rho|i\rangle$ is then given by

$$\langle f|\rho|i\rangle = \sum_i \int \langle \psi_f|\Psi_i\rangle e^{i\mathbf{q}\cdot\mathbf{r}_i} \chi^{(-)*}(\mathbf{r}_p)\, d\mathbf{r}_p \tag{2.137}$$

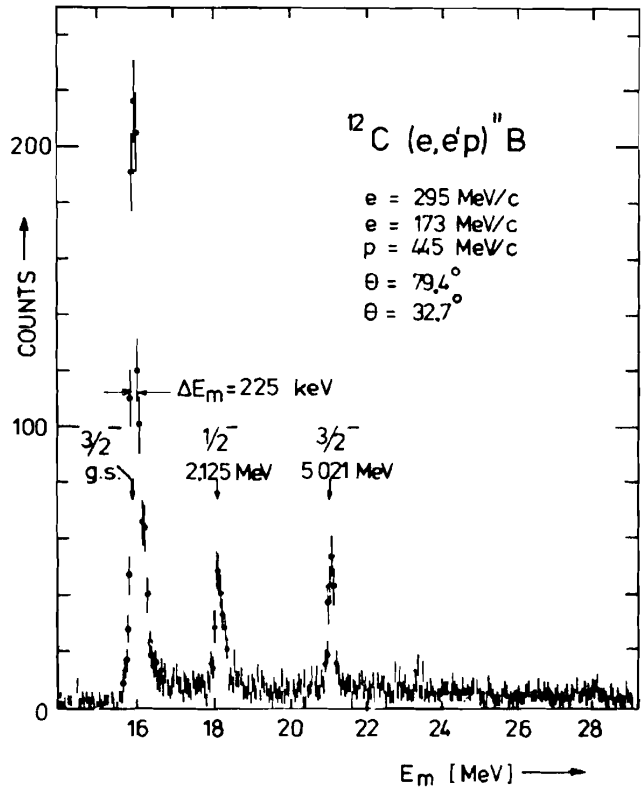

FIG. 2.24. Missing energy (E_m) spectrum of the reaction $^{12}C(e,e'p)^{11}B$ showing an energy resolution of 225 keV. Excited states in the residual nucleus ^{11}B are indicated. [From de Vries (84).]

where $\chi^{(-)*}$ is the appropriate distorted wave for the emerging proton with a final momentum of $\mathbf{p}_p$. The factor $\langle \psi_f | \Psi_i \rangle$, in which integrations over all variables but $\mathbf{r}_i$ are carried out, also appears in the DWA expression for the pickup (p,d) or $(d,{}^3\text{He})$ process [see (VII.3.4)]. However (2.137) differs from that expression in that the perturbing potential for the pickup process is a short-ranged nucleon–nucleon two-body potential v_{0i} in the notation of Chapter VII, which is to be compared with $e^{i\mathbf{q}\cdot\mathbf{r}_i}$. Therefore, substantially different properties of the overlap $\langle \psi_f | \Psi_i \rangle$ are probed in the two reactions. In the pickup reaction it is mostly the surface region of the nucleus that is involved, while in the $(e,e'p)$ case the interior plays an important role. For a detailed study of this comparison, see deWitt–Huberts (87).

There are two noteworthy results. One is that the shapes of the overlap $\langle \psi_f | \Psi_i \rangle$ wave function as determined from the $(e,e'p)$ and $(d,{}^3\text{He})$ reactions are in good agreement. Second, the predicted cross sections in both cases require

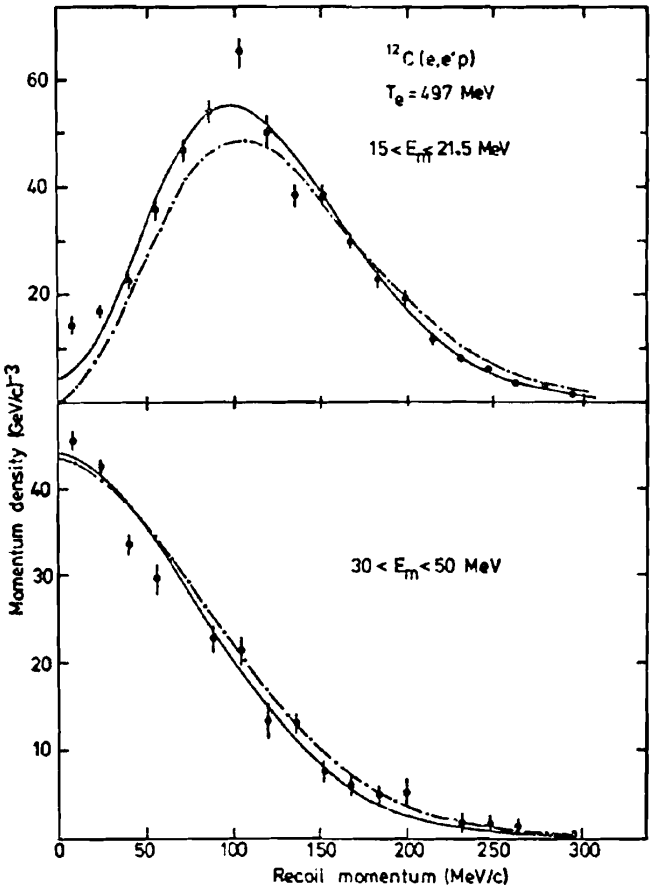

FIG. 2.25. Momentum distributions for the $(e, e'p)$ reaction on ^{12}C in two different regions of removal energy, E_m, corresponding to knock-out from the $0p$ and $0s$ shells. The calculated results using DWIA (PWIA) are given by the solid (dotted–dashed) curves and have been normalized to the experimental data. [From Dieperink and DeForest (75).]

spectroscopic factors (the probability that the overlap can be described by a single-particle wave function) considerably less than unity.

The correction resulting from the use of a distorted wave function is small. We recall from Chapter V that distorting effects of the optical potential are minimal when the proton energy is in the range 150 to 300 MeV.

Note. Assuming a valence model for the target nucleus, one can show that the exchange terms produced by the Pauli exclusion principle are zero. Let

$$\Psi_i(\mathbf{r}_p, \mathbf{r}_1, \mathbf{r}_2, \ldots) = \mathscr{A} u(\mathbf{r}_p)\psi_f(\mathbf{r}_1, \mathbf{r}_2, \ldots)$$

The wave function ψ_f is the antisymmetrized wave function for the $Z-1$ system. The function u carries the normalization. The final state

$$\Psi_f = \mathscr{A}\chi^{(-)}(\mathbf{r}_p)\psi_f(\mathbf{r}_1, \mathbf{r}_2, \ldots)$$

Antisymmetrization has not been included in (2.137) since it is automatically guaranteed by the symmetry of $\sum_i e^{i\mathbf{q}\cdot\mathbf{r}_i}$ and the antisymmetry of Ψ_i. The proof of the result that we will leave to the reader is a consequence of the condition

$$\langle u(\mathbf{r}_1)|\psi_f(\mathbf{r}_1, \mathbf{r}, \ldots)\rangle = 0$$

where the integration is carried out over $\mathbf{r}_1$.

The hole state that is formed by the proton removal is not an eigenstate of the nuclear Hamiltonian. As revealed by a high-resolution experiment, it fragments into several separate states. The hole state acts as a doorway state to these. It therefore becomes possible to apply the doorway state formalism developed in Chapter III. From (III.4.16) we have the doorway state $\mathscr{T}$ matrix

$$\langle \mathscr{T}_{fi}\rangle_{\text{doorway}} = \frac{\langle \phi_f|H_{PD}\psi_d\rangle\langle\psi_d|H_{DP}\psi_i\rangle}{E - E_d + \frac{1}{2}i\Gamma_d^{\downarrow}} \tag{2.138}$$

where we have assumed that the entire width $\Gamma_d^{\downarrow}$ is the result of fragmentation of the one-hole state. One must now take the absolute square of $\langle \mathscr{T}_{fi}\rangle$ and sum over final residual nuclear states within the width $\Gamma_d^{\downarrow}$. An energy average over narrow resonances $\psi_d^{(+)}$ is implied [see the discussion leading to (VII.5.22)]. The result is

$$|\langle \mathscr{T}_{fi}\rangle|^2 = \frac{1}{2\pi}\frac{\Gamma_d^{\downarrow}|\langle\psi_d|H_{DP}\psi_i\rangle|^2}{(E - E_d)^2 + (\Gamma_d^{\downarrow})^2/4}$$

where

$$\psi_d \simeq \psi_f^* \chi^{(-)*} \tag{2.139}$$

according to (2.137). Thus in the response function one should replace the energy delta function by

$$\frac{1}{2\pi}\frac{\Gamma_d^{\downarrow}}{(E - E_d)^2 + \frac{1}{4}\Gamma_d^2} \tag{2.140}$$

in order to obtain the results obtained when averaging over the states into which the hole state fragments. Note that Γ_d is a function of the energy. [See Orland and Schaeffer (78) for more details.] A comparison with experiment is

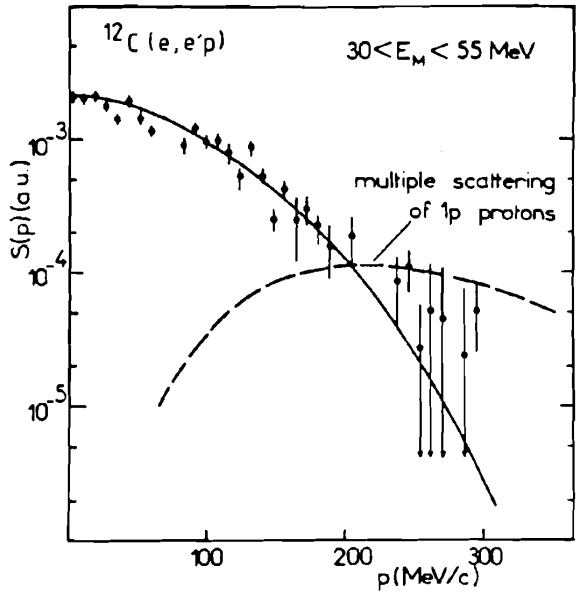

FIG. 2.26. Rescattering effects in the $^{12}C(e,e'p)$ reaction. In the separation energy region corresponding to the 1*s* shell, the contribution of 1*p* protons is estimated. [From Mougey (80).]

shown in Fig. 2.26. For a review of the experimental situation, see Mougey (80) and deWitt–Huberts (87).

This is where we will end the discussion of electron-induced reactions. Much more in the way of exclusive experiments will be done as CW electrons accelerators become operational. For example, referring to Fig. 2.23, measurement of the dependence on the angle ϕ_p will lead to further information on the nuclear matrix elements of various components of the currents. [See, e.g., (3.13) in the paper by Co' et al. (87).] and therefore to new types of response functions beyond R_L and R_T. The use of polarized electrons will yield relative phases of the nuclear matrix elements [see Donnelly (88)]. Importantly, measurement of the parity violating transitions will permit stringent tests of the "standard" theory of the electro-weak interactions. We shall not discuss the EMC effect [see Jaffe (88) and Close (88)], which appears to indicate a change in the structure of the nucleons in the nuclear environment. At least that is one interpretation. But this phenomenon is, at this moment of writing, not clearly understood experimentally and theoretically. Finally, I should mention the clear evidence for exchange currents obtained by electron scattering from ^{3}H and ^{3}He, which have not been discussed because the nuclear two- and three-body systems are not included in this volume. Nevertheless, we include two figures showing the effect of exchange currents and nucleon excitation to the Δ on the electric and magnetic form factors for ^{3}H and ^{3}He (Figs. 2.27 and 2.28).

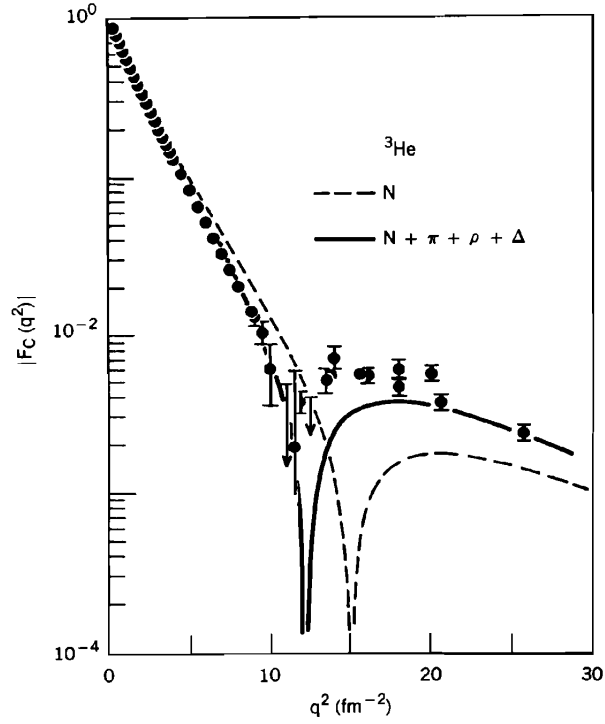

FIG. 2.27. Charge form factor of ^{3}He. The dashed curve gives the impulse approximation results. The solid curve includes the effects of meson exchange contributions. [From Hodjuk, Sauer, and Strueve (83).]

3. MEDIUM-ENERGY PROTON–NUCLEUS SCATTERING

The application of the theory of multiple scattering to the scattering of protons by nuclei was discussed briefly in Section II.8. We summarize the pertinent formulas using the KMT formalism.‡ The effective potential $V^{(1)}_{\text{opt}}(\mathbf{q}), \mathbf{q} = \mathbf{k} - \mathbf{k}'$ is given by (II.4.30)

$$V^{(1)}_{\text{opt}} = \frac{A-1}{A}\left\langle 0\left|\sum_i t_i\right|0\right\rangle = (A-1)\langle 0|t_1|0\rangle \tag{3.1}$$

‡The eikonal method is often used. However, comparison with the KMT results for 800-MeV protons (see Fig. 3.1) shows that in the lowest order the eikonal method overshoots the diffraction maxima and minima at the larger angles, especially for the polarization observables. A more careful treatment of the eikonal method beyond the first order is required. The eikonal approximation is also found to be in error in inelastic scattering [see Ray and Hoffmann (84)]. However, great improvement in the eikonal results can be obtained if higher-order corrections are made [Wallace (73a, 73b); Rosen and Yennie (64); Wallace and Friar (84)].

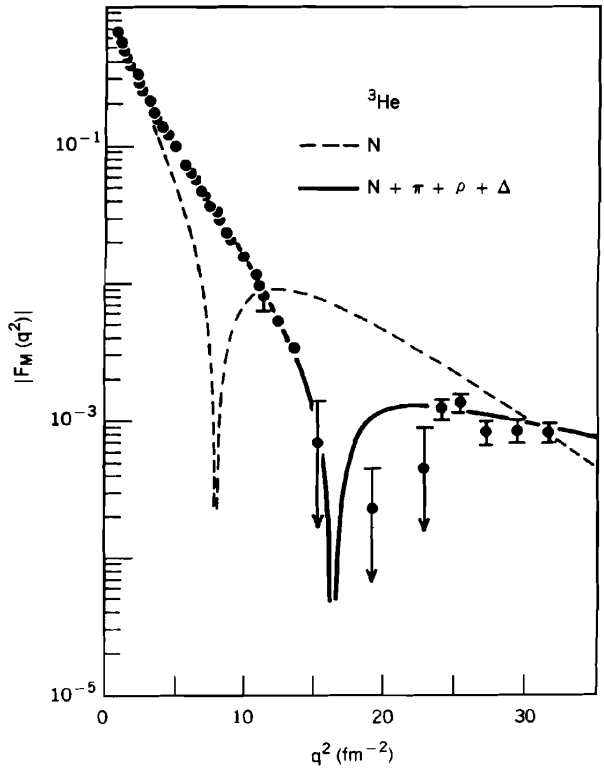

FIG. 2.28. Magnetic form factor of ^{3}He. (See caption for Fig. 2.27.)

The quantity t_i is the nucleon–nucleon transition amplitude, $|0\rangle$ is the ground state of the target, while A is the number of nucleons. In general, $V_{\text{opt}}^{(1)}$ is a nonlocal operator $V_{\text{opt}}^{(1)}(\mathbf{r}, \mathbf{r}')$. However, assuming locality [see (II.4.38)] for the transition operator t_i, $V_{\text{opt}}^{(1)}$ becomes local [Eq. (II.4.39)]. The local optical potential $v_{\text{opt}}^{(1)}$ is then [Eq. (II.4.40)],

$$v_{\text{opt}}^{(1)}(\mathbf{r}) = (A-1)\langle 0|t(\mathbf{r}-\mathbf{r}_1)|0\rangle \tag{3.2}$$

while

$$\int e^{i\mathbf{q}\cdot\mathbf{r}} v_{\text{opt}}^{(1)} d\mathbf{r} = \tilde{v}_{\text{opt}}^{(1)}(\mathbf{q}) = (A-1)\langle 0|e^{i\mathbf{q}\cdot\mathbf{r}_1}\tilde{t}(\mathbf{q})|0\rangle \tag{3.3}$$

The optical potential is to be used in a nonrelativistic Schrödinger equation. The resultant scattering amplitude is multiplied by $(A/A-1)$ [see (II.4.10)] to obtain the predicted amplitude. The superscript on $v_{\text{opt}}^{(1)}$ indicates that it is the first term in an expansion. The second term is given by (II.4.44). It depends explicitly on correlations. For most studies and except for the lightest nuclei,

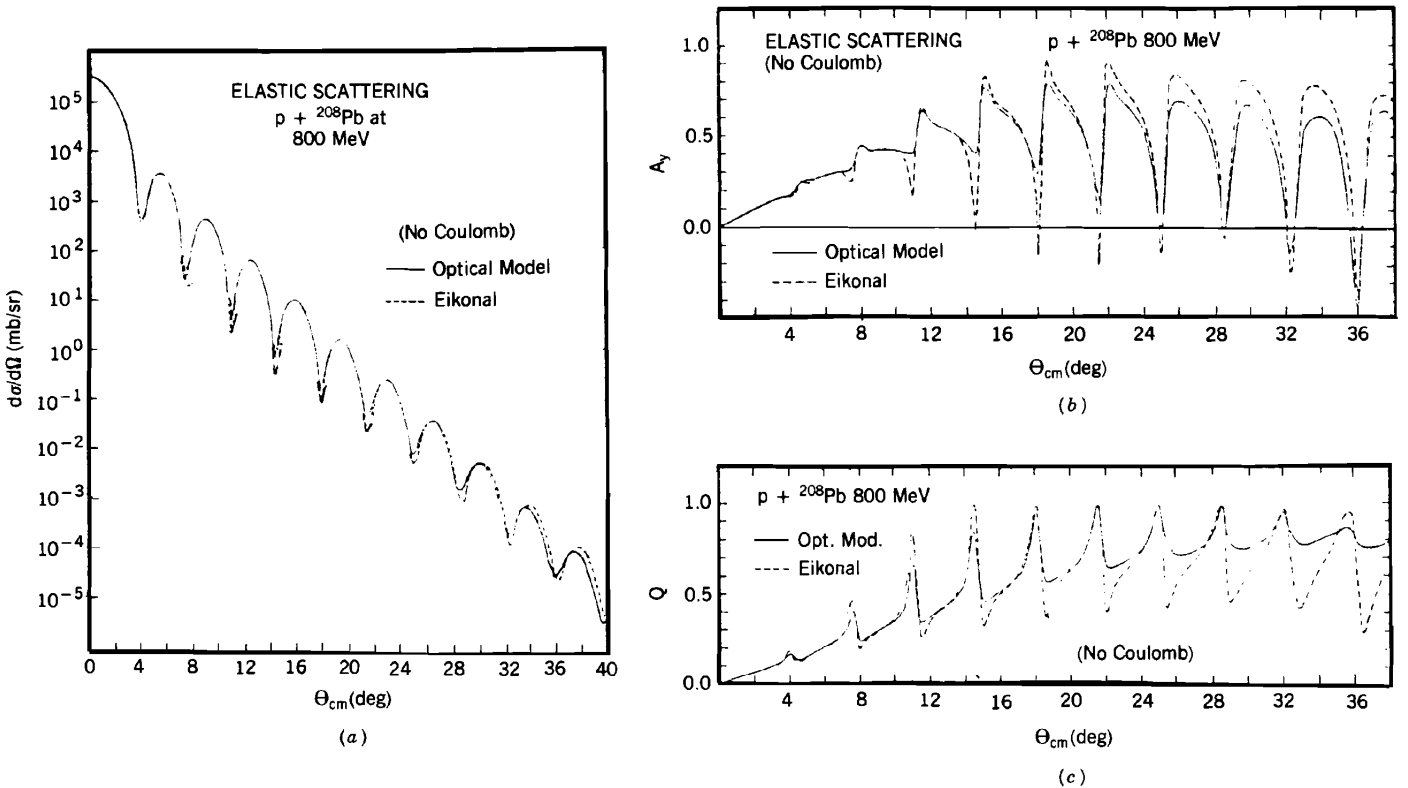

FIG. 3.1. 800-Mev $p + {}^{208}\text{Pb}$ elastic scattering: (*a*) differential cross section; (*b*) analyzing power; (*c*) spin rotation. [From Ray (83).]

this second term does not significantly affect the predicted angular distributions. However, the polarization observables are more sensitive to the correlations. The nucleon–nucleon transition matrix t_i is given in the nucleon–nucleus center-of-mass frame by (II.8.4)

$$t_i(\mathbf{k},\mathbf{k}') = A_i + B_i\boldsymbol{\sigma}_0\cdot\boldsymbol{\sigma}_i + C_i(\boldsymbol{\sigma}_0+\boldsymbol{\sigma}_i)\cdot(\mathbf{q}\times\mathbf{Q}) + D_i(\boldsymbol{\sigma}_0\cdot\mathbf{Q})(\boldsymbol{\sigma}_i\cdot\mathbf{Q}) + E_i(\boldsymbol{\sigma}_0\cdot\mathbf{q})(\boldsymbol{\sigma}_i\cdot\mathbf{q}) \tag{3.4}$$

where $\mathbf{q}=\mathbf{k}-\mathbf{k}'$ and $\mathbf{Q}=\frac{1}{2}(\mathbf{k}+\mathbf{k}')$. The subscript i refers to the struck nucleon in the target nucleus and the subscript 0 refers to the incident nucleon. The coefficients A_i, B_i, and so on, are functions of q^2 and the energy of the incident nucleon. These coefficients also depend on the isospin, for example,

$$A_i = A_+ + A_-\boldsymbol{\tau}_0\cdot\boldsymbol{\tau}_i \tag{3.5}$$

The connection between the coefficients A_i, and the coefficients A_i', and so on, appropriate to the nucleon–nucleon center-or-mass reference system is given by (II.8.5). We shall not repeat them here. One often parametrizes the coefficients A_i' as follows:

$$A' = A(0)e^{-\alpha q^2} \tag{3.6}$$

where α and A are complex functions of the energy. A table of these coefficients is given in Chapter II (Table II.8.1) for a nucleon kinetic energy L_{lab} of 1 GeV. Coefficients appropriate at other energies are given Wallace (81).‡ Note that the transformation from the nucleon–nucleon to the nucleon–nucleus reference frame is valid only at small angles. Moreover, there is an ambiguity described in the problem following (II.7.2). Finally, we remark that using the form given by (3.6) involves values of A, and so on, which for large values of q are not observable in nucleon–nucleon scattering. (See the discussion in Section II.7.) Extrapolation from nucleon–nuclear scattering to these off-the-energy-shell values is obtained by fitting the energy dependence of the coefficients $A(0)$ and α and then continuing that dependence to the required values of the energy. Another procedure, using the Breit frame, leads to (II.7.20), in which $\tilde{t}(\mathbf{k},\mathbf{k}')$ is replaced by

$$\tilde{t}\left(\frac{\mathbf{Q}(1+1/A)+\mathbf{q}}{2}, \frac{\mathbf{Q}(1+1/A)-\mathbf{q}}{2}\right)$$

evaluated at the energy $T_{\text{lab}}^{(\text{eff})} = (1/2m)(Q^2(1+1/A)^2+q^2)$. In most of the results to be reported below, only the A and C coefficients enter into $v_{\text{opt}}^{(1)}$, since the spin of the target nuclei selected is zero. The bilinear terms in spin (B, D, E, F) do contribute to the second-order terms. However, they are generally neglected in the calculation of second-order effects.

‡Note that Wallace's D is proportional to our E and his E to our D.

Despite many caveats referred to above, the agreement of the first-order multiple scattering theory with elastic scattering of protons by spin-zero nuclei at sufficiently high energy is excellent, as one can see from Fig. II.8.2. This is because the nucleon–nucleus amplitude is not sensitive to the details of the transition matrix for nucleon–nucleon scattering for relatively small values of q. The first-order potential is a product of the nucleon–nucleon $\tilde{t}$ and the nuclear $\tilde{\rho}$. Since $\tilde{t}$ is generated by a short-range force, it will change slowly with q. On the other hand, $\tilde{\rho}(\mathbf{q})$ will be sharply peaked at $q = 0$, with the consequence that only values of $\tilde{t}$ near $q = 0$ will be important. The cross section near $q = 0$ will then be a diffraction pattern given by $\tilde{\rho}(\mathbf{q})$ whose minima and maxima reflect the value of the nuclear radius. Their positions are stable against the inclusion of various effects, such as those generated by the second-order potential. Many effects are present for larger-angle scattering. In addition to correlations, there are the corrections arising from the various approximations used to obtain the simple formula (3.1) and of course the uncertainties in $\tilde{\rho}(\mathbf{q})$ and $\tilde{t}(\mathbf{q})$. A systematic treatment of the correlations, including those originating in the Pauli exclusion principle, in the center-of-mass correlation and in the spin and space correlations in the target nucleus has been given by L. Ray and G. W. Hoffmann and their associates. [See, for example, Ray (79); see also Chaumeaux, Layly, and Schaeffer (78)] Ray (79) improves upon the treatment of the Pauli correlations by Boridy and Feshbach (77) by letting k_F, the Fermi energy, be a function of r reflecting the spatial dependence of the density, which in a local density approximation is directly related to k_F. The major effect of these correlations is to increase the cross section at the diffraction maxima by an amount that increases with q and decreases with A (see Table 3.1).

The relative importance of the various correlations at the maxima is shown in Table 3.2. We see from the table that the most important correlation effect is produced by the Pauli exclusion principle. Finally, Hoffmann et al. (81) have pointed out the importance of the spin-orbit coupling that arises from the interaction of the magnetic moment of the incident proton and the Coulomb field of the target nucleus. Approximately the interaction is given by

$$H_{\text{m.d.}} = -\frac{\partial \phi}{\partial r}\frac{\mu_0 \hbar c}{2E}(\boldsymbol{\sigma}\cdot\mathbf{l}) \tag{3.7}$$

TABLE 3.1 Percent Increase in Cross Section at Diffraction Maxima

Max.	^{40}Ca	^{116}Sn	^{208}Pb
1	13	8	6
2	18	13	10
3	20	17	14
4		21	18
5			23

Source: Ray (79).

TABLE 3.2 Relative Importance of the Various Correlation Corrections[a]

	Correction (%)				
Nucleus	Pauli	SRD	PSR-I	cm	Pauli–S.O.
^{40}Ca	85	10	−2.1	11.0	−3.9
^{116}Sn	91.3	11.6	−2.4	5.2	−5.7
^{208}Pb	92.2	11.7	−2.8	3.4	−4.5

[a](1) Pauli, because of the exclusion principle; (2) SRD, short-range correlation; (3) PSR-I, interference between Pauli and short-range; (4) cm, corrections for transformation from nuclear center of mass to proton–nucleus center of mass; (5) Pauli–S.O., Pauli spin-orbit interference. Values are the percentages of the total increase in the height of the maxima in the angular distribution.

where ϕ is the nuclear electrostatic potential and μ_0 is the proton magnetic moment.[‡] The comparison with experiment of the calculated angular distribution, including only A and C terms of (3.4), second-order terms, and magnetic moment effects, are shown in Fig. 3.2. The incident protons have an energy of 800 MeV; the target nuclei are ^{16}O, ^{40}Ca, and ^{208}Pb. The proton density is taken from electron scattering while the neutron density is calculated according to the following recipe:

$$\rho_n(r) = \rho_p(r) + [\rho_n(\mathbf{r}) - \rho_p(\mathbf{r})]_{\mathrm{HFB}} \tag{3.8}$$

where the densities within brackets is taken from Hartree–Fock–Bogoliubov calculations [Dechargé et al. (81)]. Agreement is good except that as is especially noticeable in the lead case, the predicted diffraction oscillations are out of phase with experiment at the larger scattering angles.

One need not use (3.8) but rather determine the neutron density from experiment. A check on the method used is obtained by comparing the proton density difference obtained using polarized elastic scattering with that obtained using electron elastic scattering from ^{48}Ca and ^{54}Fe. In first approximation the neutron densities are the same, so that the differences in the proton densities can be obtained. The results are shown in Fig. 3.3. Agreement is quite good, especially in the region of large r when both experiments have smaller uncertainties. At smaller r the uncertainties are much larger, so that the agreement is less significant. Examples of the neutron densities determined by proton scattering in comparison with that obtained from Negele's density matrix expansion (DME) are shown in Fig. 3.4. Reasonable agreement is obtained.

[‡]Hoffmann et al. (81) use a more accurate expression which is valid relativistically and takes the nucleon form factors into account.

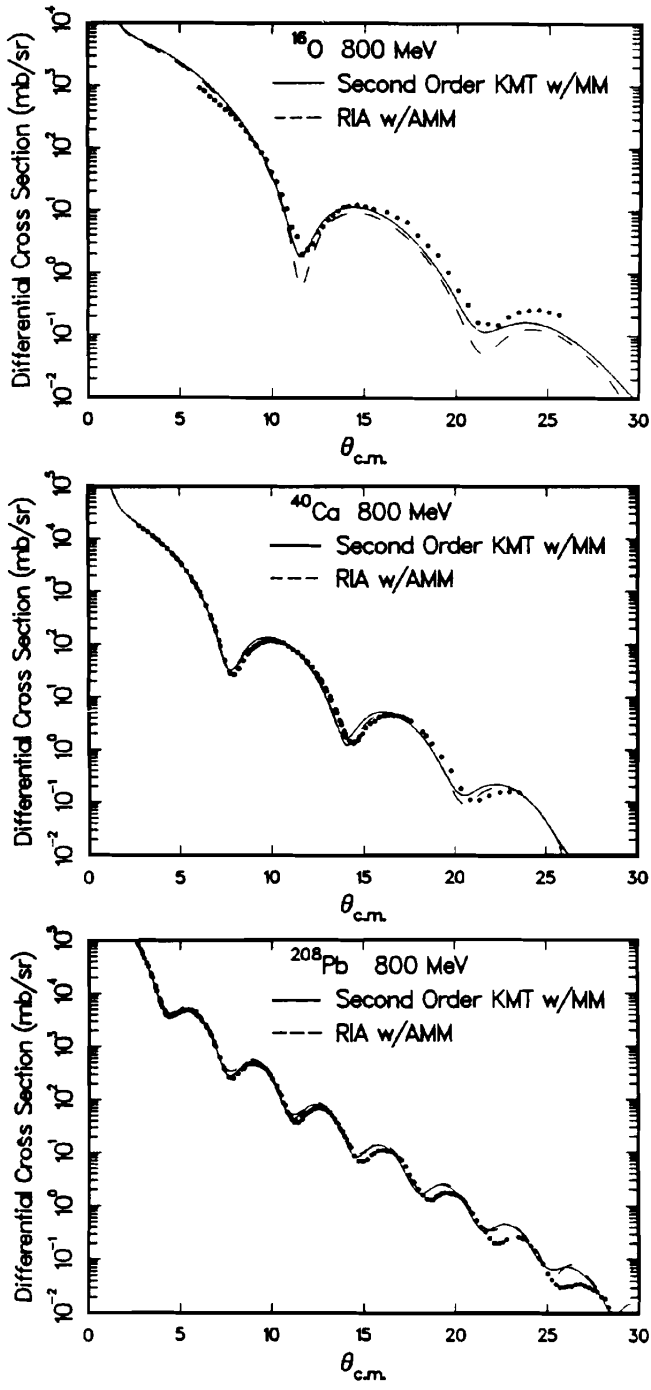

FIG. 3.2. The 800-MeV $\mathbf{p} + {}^{16}\mathbf{O}$, ^{40}Ca and ^{208}Pb elastic differential cross section compared to the nonrelativistic and relativistic predictions (RIA). MM refers to the magnetic moment correction. A in AMM stands for anomolous. [From Fergerson, Barlett, et al. (86).]

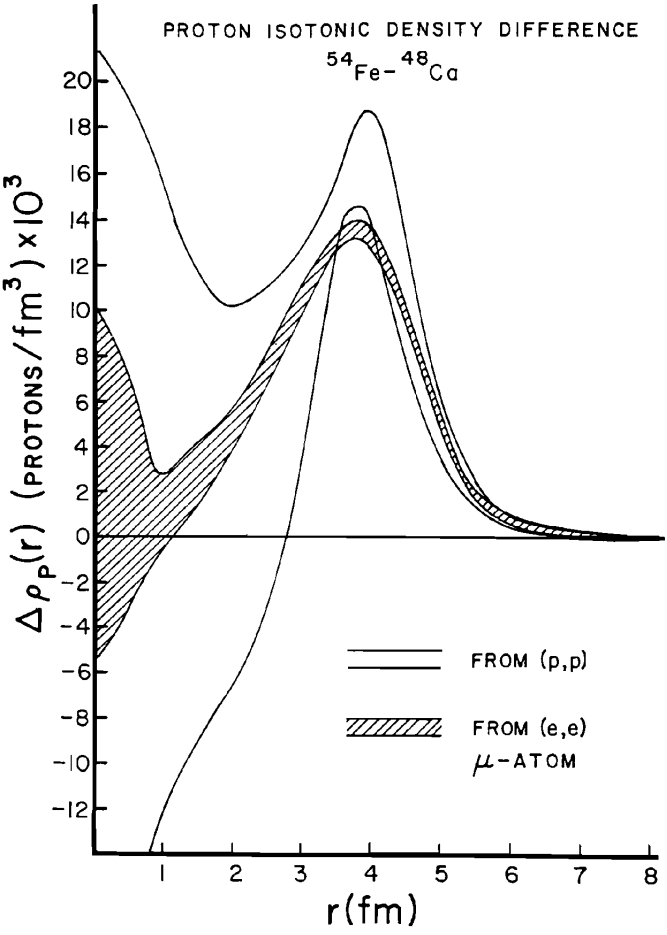

FIG. 3.3. Comparison of the proton density differences between Fe and Ca obtain by analysis of 800-MeV proton elastic scattering (outer band) with that obtained by electromagnetic measurements (inner shaded band). [From Ray and Hoffmann (83).]

We consider next the two independent polarization observables, Q, the spin rotation, and A_y, the analyzing power, which by time reversal equals P in (V.2.52). These provide a more subtle test of our understanding of the elastic scattering of protons by nuclei. In particular, they are more sensitive in the angular regions covered by the minima in the angular distributions. In Fig. 3.5 we present first-order KMT calculations of the analyzing power, the second-order KMT (i.e., including correlations), and finally, calculations that include the magnetic moment effect [Eq. (3.7)] designated by *MM*. The data points are obtained with polarized 800-MeV proton beams available at LAMPF. The target nuclei are ^{16}O, ^{40}Ca, and ^{208}Pb. We see that the correlation effects

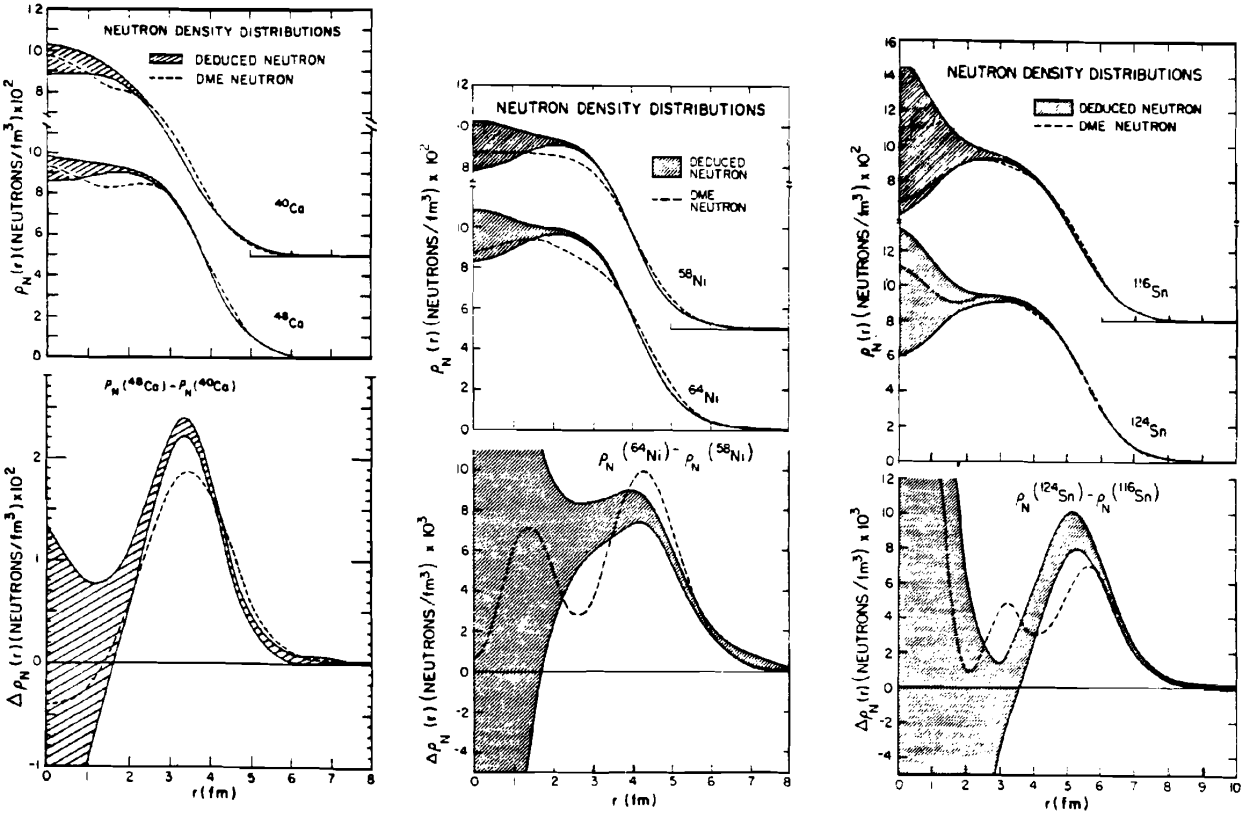

FIG. 3.4. Point neutron density distributions for ^{40}Ca, ^{48}Ca, ^{58}Ni, ^{64}Ni, ^{116}Sn, and ^{124}Sn deduced from second-order KMT analysis (shaded bands) and predicted by the density matrix approach (dashed curves DME) of Negele. [From Ray (79).]

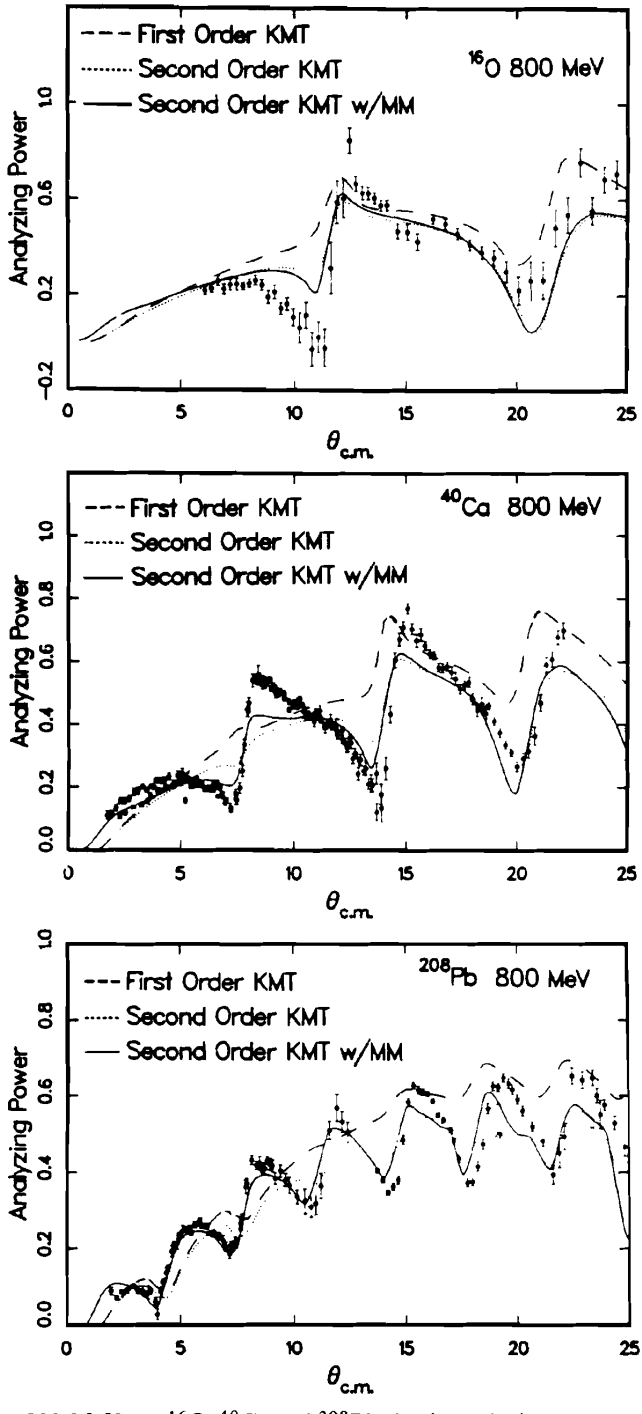

FIG. 3.5. The 800-MeV p + ^{16}O, ^{40}Ca and ^{208}Pb elastic analyzing power data compared to various nonrelativistic impulse approximation predictions. [From Fergerson, Barlett, et al. (86).]

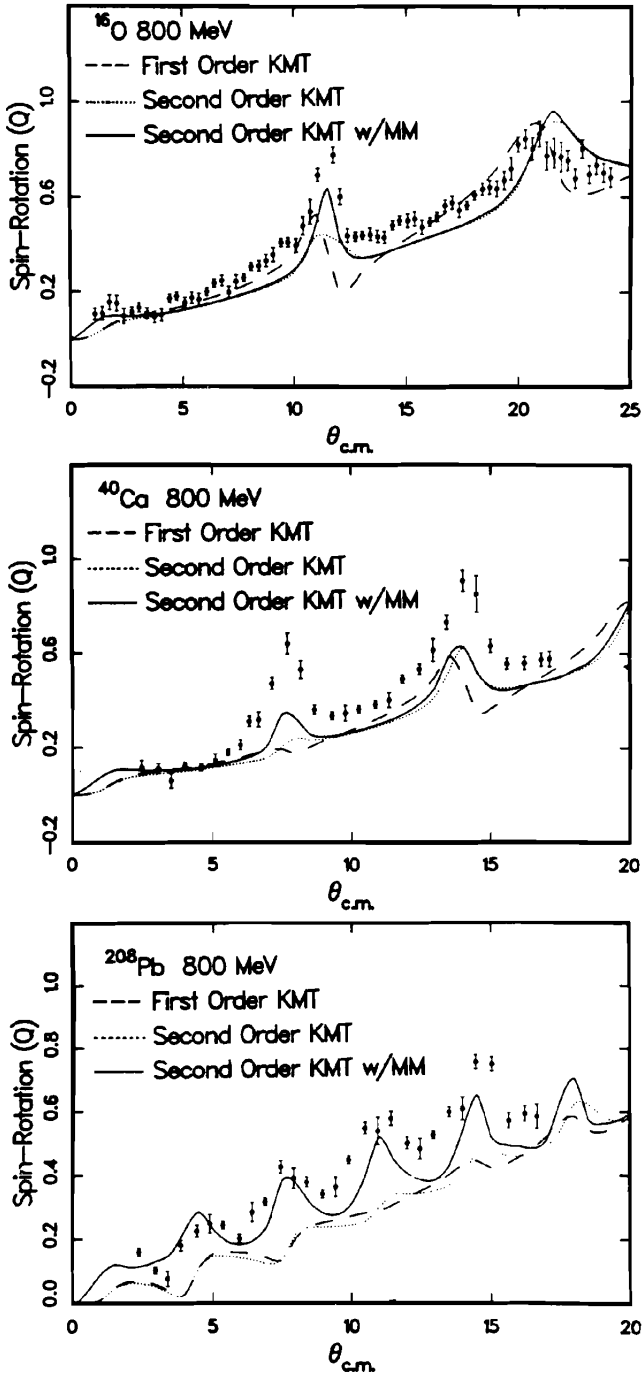

FIG. 3.6. The 800-MeV $\mathbf{p}$ + ^{16}O, ^{40}Ca and ^{208}Pb spin-rotation data compared to various nonrelativistic impulse approximation predictions. [From Fergerson, Barlett, et al. (86).]

are quite large and for the case of ^{16}O are sufficient to bring the calculation and experiment into substantial agreement. For ^{40}Ca and especially for ^{208}Pb, the magnetic moment effect plays an important role. Generally, the first-order KMT does not give sufficient structure; terms "proportional" to ρ^2 and the magnetic moment modification of the spin-orbit term are necessary. Both of these act to break the correlation between the numerator in the expression for the polarization and the angular distribution that is in the denominator. A similar story prevails for the spin-rotation parameter Q, as illustrated by Fig. 3.6. In these cases correlation effects are not significant; the improvement on KMT is largely carried by the magnetic moment interaction. The agreement with the data is quite good, although there are substantial deviations in the Q for the ^{40}Ca target.

These polarization tests of the KMT theory are incomplete, since the effects of the spin–spin terms in the t matrix may be appreciable [Feshbach (90)]. However, detailed calculations that would show how these effects affect the polarization observables are not available [except for a calculation of Q for ^4He by Parmentola and Feshbach (82)].

Another approach to nucleon–nucleus scattering is referred to as the *relativistic impulse approximation.* We shall only sketch this procedure. For more details and references, we refer the reader to a review by Wallace (87). Very briefly, a relativistic transition operator for the nucleon–nucleon interaction is taken to be

$$t_D = f_s + f_v \gamma_\mu^{(1)} \gamma_\mu^{(2)} + f_t \sigma_{\mu\nu}^{(1)} \sigma_{\mu\nu}^{(2)} + f_a \gamma_5^{(1)} \gamma_\mu^{(1)} \gamma_5^{(2)} \gamma_\mu^{(2)} + f_{ps} \gamma_5^{(1)} \gamma_5^{(2)} \tag{3.9}$$

The equivalent Schrödinger form, t_s, is obtained from the equation

$$\begin{aligned} &\bar{u}_1(\mathbf{k}'_1, s'_1)\bar{u}_2(\mathbf{k}'_2, s'_2) t_D \bar{u}_1(\mathbf{k}_1, s_1) u_2(\mathbf{k}_2, s_2) \\ &\quad = \chi_1^\dagger(\mathbf{k}'_1, s'_1)\chi_2^\dagger(\mathbf{k}'_2, s'_2) t_s(\mathbf{k}_1, \mathbf{s}_1)\chi_1(\mathbf{k}_1, s_1)\chi_2(\mathbf{k}_2, s_2) \end{aligned} \tag{3.10}$$

where $u(\mathbf{k}, s)$ is the four-component plane wave solution of the Dirac equation and $\chi(\mathbf{k}, s)$ is a two-component Pauli plane wave spinor. The process described by (3.10) is one in which particle 1 makes the transition from momentum $\mathbf{k}_1$, spin s, to momentum $\mathbf{k}_1$, spin s'_1 with a similarly indicated change for particle 2. For a detailed discussion of this transformation, see McNeil, Ray, and Wallace (83) and Ray and Hoffmann (85). The resulting amplitude must be folded into the appropriate nuclear density functions. These must be relativistic in origin and are obtained from relativistic theories of the nucleus such as those proposed by Walecka [Serot and Walecka (86) or Celenza and Shakin (86)]. The first of these is a σ(scalar)–ω (vector) model treated by a mean field approximation. The second is a relativistic Breuckner–Hartree–Fock approximation starting with a relativistic nucleon–nucleon force taken from a meson exchange model. The resulting one-body Dirac equation describing nucleon–nucleus scattering

is, according to Ray and Hoffmann (85),

$$\left\{c\boldsymbol{\alpha}\cdot\mathbf{p} + \beta(mc^2 + U_s(r)] + [U_V(r) + U_{\text{Coul}}(r)]\right.$$
$$\left. - i\beta\boldsymbol{\alpha}\cdot\hat{\mathbf{r}}\left[2U_T(r) + \frac{\kappa_p}{2m}\frac{\partial}{\partial r}U_{\text{Coul}}(r)\right]\right\}\phi = E\phi. \tag{3.11}$$

In this equation U_S, U_V, and U_T are the scalar, vector, and tensor potentials, κ_p is the proton anomalous magnetic moment, and E is the total relativistic energy of the proton in the proton–target nucleus center-of-mass frame. It is found that U_T has a small effect on the scattering so that it is omitted in the calculations reported below. Equation (3.11) is remarkably similar to the relativistic model discussed in Chapter V. The results obtained with the RIA agree with the empirical results of that model as demonstrated in Fig. 3.7. With these assumptions one obtains the angular distributions of Fig. 3.2, labeled RIAw/AMM. The agreement with experiment is better than KMT for the target nuclei ^{40}Ca and ^{208}Pb but not as good as KMT for target nucleus ^{16}O. In Fig. 3.8 we compare the predictions of the analyzing power, and Fig. 3.9, the spin rotation, is given for the relativistic theory. From Fig. 3.8 we see that

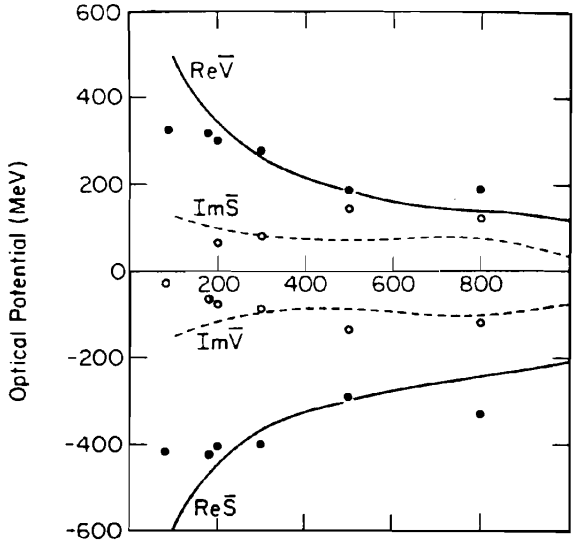

FIG. 3.7. Isospin averaged scalar vector ($\bar{V}$) potential at nuclear matter density as a function of the proton kinetic energy. Solid and dashed lines are the predictions of the relativistic impulse approximation. Filled and open circles are the phenomenological values for the real and imaginary potentials found by fitting proton scattering data using the Dirac equation. [From Wallace (87).]

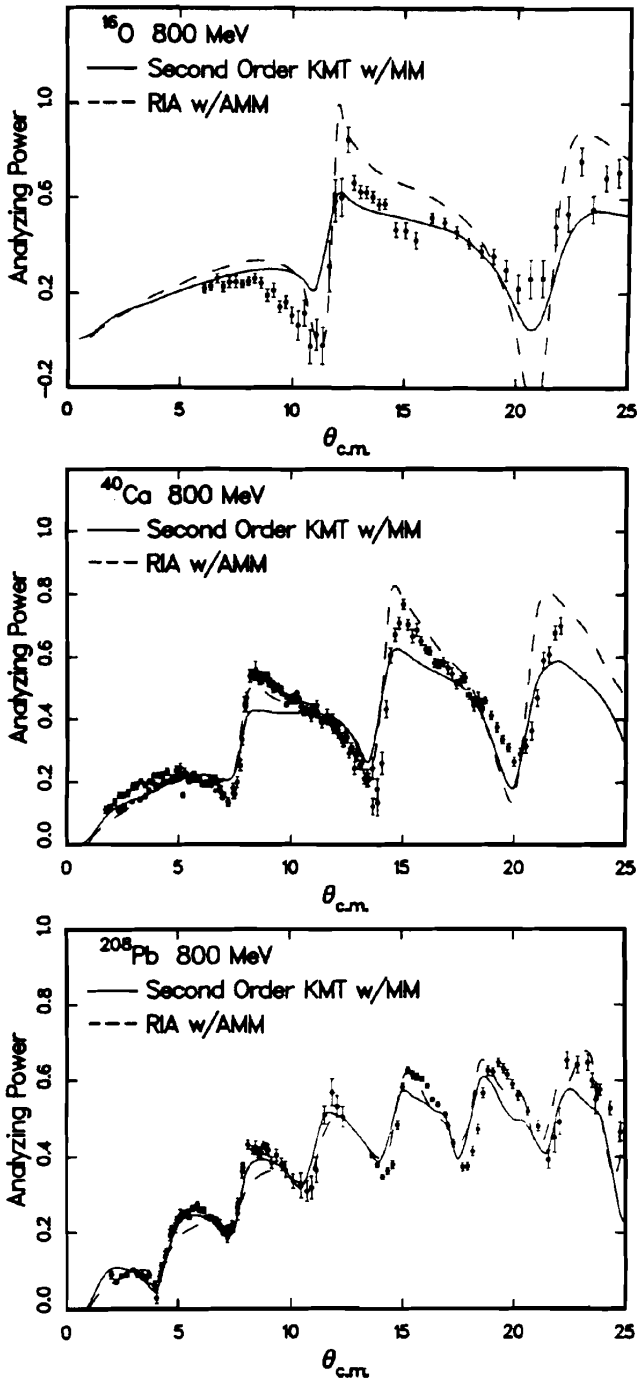

FIG. 3.8. The 800-Mev p + ^{16}O, ^{40}Ca and ^{208}Pb elastic analyzing power data compared to the nonrelativistic and relativistic impulse approximation predictions. [From Fergerson, Bartlett, et al. (86).]

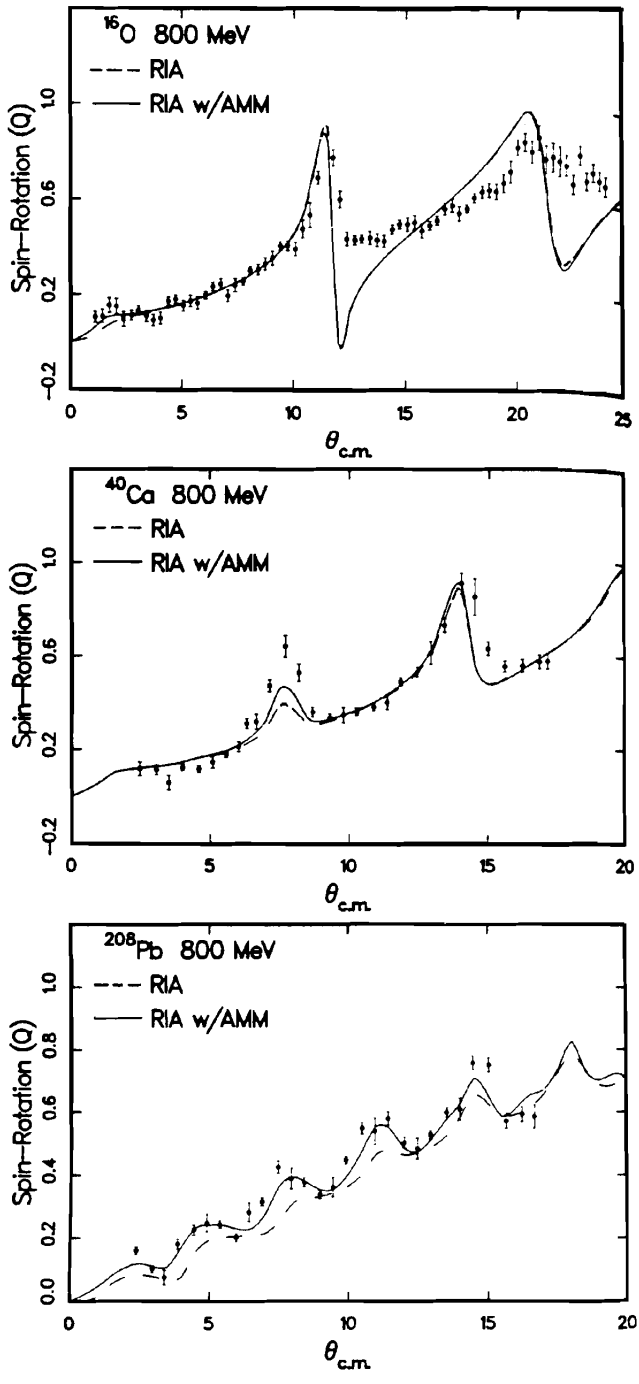

FIG. 3.9. The 800-Mev $\mathbf{p} + {}^{16}\mathrm{O}$, $^{40}\mathrm{Ca}$, and $^{208}\mathrm{Pb}$ spin-rotation data are compared to relativistic impulse approximation predictions. [From Fergerson, Bartlett et al. (86).]

RIA and KMT differ from experiment in differing ways, but it would be difficult on this basis to choose one above the other. In Fig. 3.9 the RIAW/AMM result differs considerably from the ^{16}O experiment, with which second-order KMT/MM is in substantial agreement (see Fig. 3.6). Agreement with ^{40}Ca and ^{208}Pb data is good. Overall the sharp difference in the ability of the KMT and RIA models to match the data, especially that of the rotation spin parameter, is not repeated at 800 MeV.

The second-order corrections to RIA are severe. This is because one can add many terms to t_D [Eq. (3.9)] that will not contribute to the positive energy projection, (3.10). As a consequence, t_s is ambiguous [Adams and Bleszynski (84)] since these additional terms can contribute to the second-order potential. No information on their strength is available from the nucleon–nucleon amplitude. According to Tjøn and Wallace (85, 87), t_D can contain 56 terms for each isospin. Tjon and Wallace reduce the number of independent terms by invoking relations obtained from a relativistic theory of the nucleon–nucleon interaction. They thus obtain a fit to nuclear forces as well as to medium-energy nucleon–nucleon scattering.

4. PROTON ^{4}He ELASTIC SCATTERING AND THE EFFECT OF ISOBAR EXCITATION[‡]

The angular distribution of 1-GeV protons scattered by ^{4}He is shown in Fig. I.15.2 in deShalit and Feshbach (74). The experimental points shown are not correct, as shown by subsequent experiments [Geaga et al. (77); Courant et al. (79)]. The strong diffraction minimum is filled in so that the angular distribution is flat in the neighborhood of 20° and then drops off quite rapidly. It is not possible to explain these results using only the first-order KMT potential. This is primarily because to that order the angular distribution is given by the Fourier transform of the density $\rho(\mathbf{q})$ for ^{4}He. But $\rho(\mathbf{q})$ is quite accurately determined by electron scattering. It is thus essential to consider the second-order term:

$$\begin{aligned}\langle \mathbf{k}|V^{(2)}|\mathbf{k}'\rangle = (A-1)^2 \int \frac{d\mathbf{k}''}{(2\pi)^3} \int \frac{d\mathbf{k}'''}{(2\pi)^2} \{ &\langle 0|\tilde{t}_1(\mathbf{k}-\mathbf{k}'')\tilde{t}_2(\mathbf{k}'''-\mathbf{k}')|0\rangle \\ &- \langle 0|\tilde{t}_1(\mathbf{k}-\mathbf{k}'')|0\rangle\langle 0|\tilde{t}_2(\mathbf{k}'''-\mathbf{k}')|0\rangle\} \\ &\times \langle \mathbf{k}''| \frac{1}{E-\bar{\varepsilon}-V^{(1)}-K} |\mathbf{k}'''\rangle \end{aligned} \tag{4.1}$$

Here $\tilde{t}_1(\mathbf{k}-\mathbf{k}'')$ is the t matrix for the scattering of the proton by the nuclear nucleon labeled by the subscript. Matrix elements are taken with respect to the

[‡]Wallace (80); Parmentola and Feshbach (82).

ground state, $|0\rangle$. In the propagator, E is the energy, $\bar{\varepsilon}$ an average excitation energy, $V^{(1)}$ the first-order potential, and K the kinetic energy operator for the incident proton in the nucleon–nucleus center-of-mass system. When the effect of $V^{(2)}$ is evaluated (as, indeed, one must because of the center-of-mass correlations), including dynamical and Pauli correlations and including the entire expression for the nucleon–nucleon matrix, (3.4), using the Wallace–Alexander parametrization (Table II.8.1) there are substantial changes but the diffraction minimum remains.

A possible remedy suggested by Ikeda (72) and exploited by Alexander and Wallace (72) is isobar excitation, which can also contribute to $V^{(2)}$. In this process the incident proton in scattering by a nucleon is transformed into a Δ and in its second scattering deexcited to a proton. Note that the second scattering must involve a second and different nucleon to avoid double counting. De-excitations by the nucleon that produced the excitation have already been included in the nucleon–nucleon transition. Thus in (4.1), $\tilde{t}_1\tilde{t}_2$ should be rewritten

$$\tilde{t}_1\tilde{t}_2 = \tilde{t}_1(NN_1 \to NN_1)\tilde{t}_2(NN_2 \to NN_2) + \tilde{t}_1(NN_1 \to \Delta N_1)\tilde{t}_2(\Delta N_2 \to NN_2) \quad (4.2)$$

The second term is new. The amplitude $f(NN_1 \to \Delta N_1)$ corresponding to $\tilde{t}(NN_1 \to \Delta N_1)$ in the nucleon–nucleon reference frame is parametrized by

$$f(NN_1 \to \Delta N_1) = f(0)e^{-\Delta q^2}\boldsymbol{\sigma}_1 \cdot \mathbf{S}\boldsymbol{\tau}_1 \cdot \mathbf{T} \quad (4.3)$$

where $\mathbf{S}$ and $\mathbf{T}$ are $\frac{3}{2}$ spin and isospin operators ($S^2 = \frac{15}{4}$). In principle, f should be chosen so as to yield the observed cross section for Δ production in nucleon–nucleon scattering. At 1 GeV the isobar production cross section is substantial ($\sim$22 mb). A fit to the data in the form given by (4.3) has been obtained by Chadwick et al. (62). Parmentola takes

$$f(0) = 7iD'_{pp}(0)$$

$$\Delta \simeq \delta_{pp}$$

with

$$B'_- = D'_- = E'_- = 0$$

that is, assuming that B', D' and E' do not depend on isospin yields (Fig. 4.1).

Two points should be noted. One is that a corollary of the isobar excitation is the existence of three-body forces in nuclei. The impact on our understanding of the binding energy of nuclei, especially the three-body systems, has not been calculated. Second, since the expectation value of (4.3) with respect to spin is zero for zero-spin nuclei, one will find that the isobar addition to $V^{(2)}$ for zero-spin nuclei will decrease like $1/A$ with increasing A. It thus will not be of importance for the angular distributions for proton–nucleus scattering for the heavier nuclei.

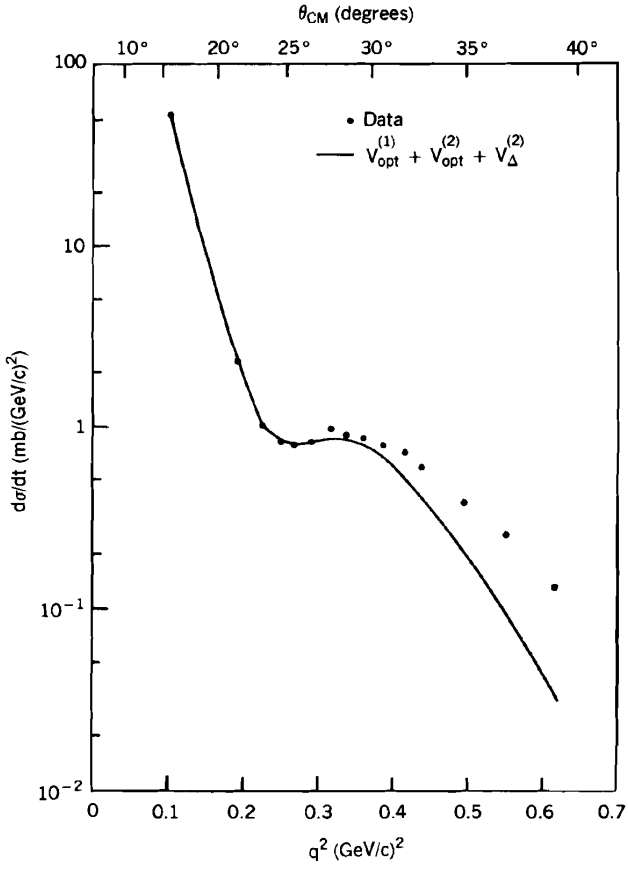

FIG. 4.1. Elastic differential p-^{4}He, $E(p) = 1.03\,\text{GeV}$ cross section compared to the predictions of multiple scattering theory including the effects of the isobar Δ. [From Parmentola and Feshbach (82).]

5. REACTIONS INDUCED BY MEDIUM-ENERGY PROTONS

Reactions, such as inelastic scattering, quasi-elastic scattering, and particle transfer, have all been treated theoretically using the DWA of Chapter V and VI. The matrix element between the initial $|a\rangle$ and $|b\rangle$ nuclear states is given by [see (3.1)]

$$\mathscr{V}_{ba} = \frac{A-1}{A}\langle b|\sum_i t_i|a\rangle \tag{5.1}$$

To obtain the $\mathscr{T}$ matrix for the reaction one calculates the matrix element $\mathscr{V}_{ba}$ between the initial state of the projectile and the final state of the emerging

system. The reader is referred back to Chapters V and VI for the details. There is one simplification: namely, for forward scattering and production one can neglect the Pauli principle between the projectile and target.

The DWA has been applied successfully to inelastic scattering leading to excitation of collective levels [see, for example, Chaumeaux, Layly, and Schaeffer (78) and Blanpied, Ritchie, et al. (88)]. The potential $\mathcal{V}_{ba}$ may be expressed in terms of the transition density:

$$\mathcal{V}_{ba} = \int d\mathbf{r}_1 \cdots d\mathbf{r}_A \, \psi_b^*(\mathbf{r}_1 \cdots \mathbf{r}_A) \frac{A-1}{A} \sum t_i(\mathbf{r}_i, \mathbf{r}_0) \psi_a(\mathbf{r}_1 \cdots \mathbf{r}_A)$$

$$= (A-1) \int d\mathbf{r}_1 \, \rho_{ba}(\mathbf{r}_1) t_1(\mathbf{r}_1, \mathbf{r}_0) \tag{5.1'}$$

where

$$\rho_{ba}(\mathbf{r}_1) = \int \psi_b^*(\mathbf{r}_1 \cdots \mathbf{r}_A) \psi_a(\mathbf{r}_1 \cdots \mathbf{r}_A) \, d\mathbf{r}_2 \cdots \tag{5.2}$$

If we employ only the component of t_1 independent of the proton spin, the angular momentum transfer in the reaction will be orbital. If the angular momentum transfer is l, the only component of the ρ_{ba} that will be effective is proportional to $Y_{lm}(\mathbf{r}_1)$, leading to the definition

$$\rho_{ba,l}(r_1) = \int Y_{lm}^*(\mathbf{r}_1) \rho_{ba}(\mathbf{r}_1) d\hat{\mathbf{r}}_1 \tag{5.3}$$

The quantities $\rho_{ba}(\mathbf{r}_1)$ and $\rho_{ba,l}(r_1)$ are referred to as transition densities. The proton transition density can be determined from inelastic electron scattering. High-energy proton scattering will permit the additional study of the neutron transition density. Ray and Hoffmann (83) use two forms for the transition density

$$\rho_{ba;l} = \xi_l f'(r) \tag{5.4}$$

where ξ_l is a parameter and f is given by the forms

$$f(r) = \frac{1}{1 + e^{(r-c)/z}} \qquad \text{two parameters} \tag{5.5}$$

or

$$f(r) = \frac{1 + wr^2/c^2}{1 + e^{(r^2 - c^2)/z^2}} \qquad \text{three parameters} \tag{5.6}$$

The parameters now include c, z, and w. The constants in each of these forms are chosen as to give a best fit to the data. The consequent $f_{ab,l}$ can then be

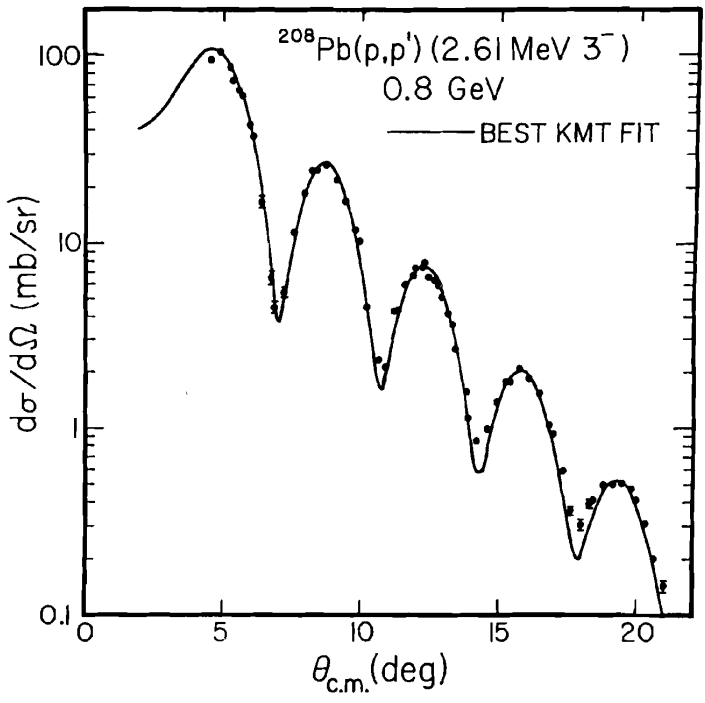

FIG. 5.1. Experimental data and best KMT fit for 800-MeV (p, p') to the 2.61-MeV 3^- state in ^{208}Pb. [From Ray and Hoffmann (83).]

compared with the results of a microscopic calculation. The best fit using the two-parameter form for the reaction ^{208}Pb(p, p') exciting the 2.6-MeV, 3^- level in lead is shown in Fig. 5.1. The fit is excellent. A similar fit is obtained with the three-parameter form. However, these do not give identical neutron transition densities, as one can see from Fig. 5.2. As one can anticipate, the two transition densities are identical in the surface region but differ substantially in the interior, indicating the insensitivity of the experimental data to the interior values. This insensitivity is a consequence of the absorption of the incident proton wave.

One can go beyond the DWA and use, for example, the method of coupled channels described in Chapter VII. Such a treatment is useful and practical when the excited levels are collective. It has been applied to such excitations in a series of papers by Blanpied et al. with moderate success. References to these articles are given in Blanpied (88). One noteworthy feature uncovered by these investigations is the need to increase the number of channels in the calculation as the angular range increases. Other methods make use of the Glauber representation and group properties of the exponential $\exp(-\int V dx)$. Bassichis, Feshbach, and Reading (11) treat the vibrational case, while Ginocchio

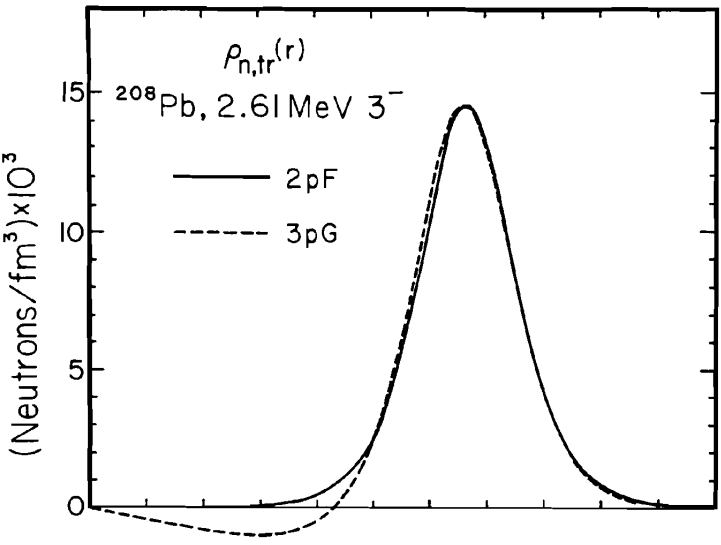

FIG. 5.2. Deduced neutron transition density for the 2.61 MeV 3^- state in ^{208}Pb. The two-parameter Fermi (2pF) and three-parameter (3pG) forms are shown. [From Ray and Hoffmann (83).]

et al [see the review by Ginocchio and Wenes (86)] generalize to deformed nuclei using the Hamiltonian of the interacting boson model.

It is expected that there is a close relation between the elastic and inelastic cross sections in high-energy reactions when the excited states are low-lying collective models. One should recall that connection established by Austern and Blair (65) at lower energies (see Chapter V). At the higher energies under consideration in this chapter it is again possible to express the inelastic scattering cross section for excitation of a collective state in terms of the elastic scattering cross section. Use is made of the eikonal approximation to the initial and final state projectile wave functions and of the Tassie (56) parametrization of the matrix element, which is appropriate for collective state excitation. That approximation yields [see (II.5.7)

$$\psi_f^* \psi_i = e^{i\mathbf{q}\cdot\mathbf{r}} e^{i\chi} \tag{5.7}$$

where

$$\chi = -\frac{i}{2K} \int_{-\infty}^{\infty} U(\mathbf{b}, z')\, dz' \tag{5.8}$$

But from (II.4.30.)

$$U = -4\pi(A-1)\rho(f(0))$$

where $f(0)$ is the scattering amplitude evaluated at 0°. From the optical theorem

$$\sigma_T = \frac{4\pi}{k} \operatorname{Im} f(0^\circ) \tag{5.9}$$

so that

$$f(0) = \frac{k}{4\pi} \sigma_T (r + i) \tag{5.10}$$

where r is the ratio of $\operatorname{Re} f$ to $\operatorname{Im} f$. Then

$$i\chi = -\frac{\sigma_T}{2}(1 - ir)(A - 1) \int_{-\infty}^{\infty} \rho(z, \mathbf{b})\, dz = -g(\mathbf{b}) = -\gamma t(b)$$

$$t(b) \equiv \int_{-\infty}^{\infty} \rho(z, \mathbf{b})\, dz \tag{5.11}$$

The amplitude for inelastic scattering exciting a level with spin L, z projection M, and parity π is

$$f_{\text{in}}(0^\pi, 0 \to I^\pi, M) = -\frac{1}{4\pi} \frac{E + mc^2}{\hbar^2 c^2} \int e^{i\mathbf{q}\cdot\mathbf{r} - g(\mathbf{b})} \langle I^\pi M | V | 0^\pi 0 \rangle\, d\mathbf{r} \tag{5.12}$$

Following the discussion of Amado, Lenz, McNeil, and Sparrow (80), one notes that because of the transformation properties of $|I^\pi, M\rangle$ and $|0^\dagger, 0\rangle$, it follows that

$$A \langle I^\pi M | t(\mathbf{r}, \mathbf{r}_1) | 0^+ 0 \rangle \equiv \langle I^\pi M | V | 0^+ 0 \rangle = f_I(r) P_{IM}(\vartheta) e^{iM\varphi} \tag{5.13}$$

where P_{IM} are the associated Legendre polynomials. In addition, Amado, Lenz, McNeil, and Sparrow (80) use the Tassie parametrization (56), where

$$f_I = \lambda_I r^{I-1} \frac{d\rho}{dr} \tag{5.14}$$

The parameter λ_I can be related to the transition probabilities (BEI) obtained from an analysis of inelastic electron scattering using the Tassie form [see, e.g., Heisenberg, McCarthy, and Sick (71)]. Substituting (5.13) and (5.14) in (5.12), replacing approximately $\mathbf{q}\cdot\mathbf{r}$ by $\mathbf{q}\cdot\mathbf{b}$, and integrating over φ yields

$$f_{\text{in}}(0^+, 0 \to I^\pi, M) = -\frac{1}{2} \lambda_I \frac{E + mc^2}{\hbar^2 c^2} i^{-M} \int_0^{\infty} J_M(qb) b\, db\, e^{-g(b)}$$

$$\times \int_{-\infty}^{\infty} dz \left(r^{I-1} \frac{d\rho}{dr} \right) P_{IM}(\vartheta) \tag{5.15}$$

Note that P_{IM} is a polynomial in $z^n b^{I-n}/r^I$; n is odd if $(I+M)$ is odd, even if $(I+M)$ is even. Multiplying by $r^{I-1}\,d\rho/dr$ yields $z^n b^{I-n}[(1/r)(d\rho/dr)]$. The integrand in the z integral of (5.15) is thus odd if n is odd and thus will vanish for odd $(I+M)$. This result was obtained earlier in (V.4.20). We shall now restrict the discussion to the $I=1$ case for illustrative purposes. The details for the general values of I are given in Amado, Lenz, McNeil, and Sparrow (80) and the review article by Amado (85). We are then concerned with only $f\,\text{in}(0^+, 0 \to 1^-, \pm 1)$. For $M=1$, we need $P_{11} = -(3/8\pi)^{1/2} b/r$, so that

$$f_{\text{in}}(0^+, 0 \to I^\pi, M) = \frac{1}{2i}\lambda_1 \frac{E+mc^2}{\hbar^2 c^2}\left(\frac{3}{8\pi}\right)^{1/2} \int_0^\infty J_1(qb) e^{-g(b)} b^2\, db \int_{-\infty}^{\infty} dz \frac{1}{r}\frac{d\rho}{dr}$$

The z integral can be reduced by noting that $(1/r)(d\rho/dr) = (1/z\,d\rho/dz)$ and

$$\frac{\partial}{\partial b}\int_{-\infty}^{\infty} dz\, \rho(\sqrt{z^2+b^2}) = b\int_{-\infty}^{\infty} dz \frac{1}{r}\frac{d\rho}{dr}$$

Therefore,

$$f_{\text{in}}(0^+, 0 \to 1^-, 1) = \frac{1}{2i}\lambda_1 \frac{E+mc^2}{\hbar^2 c^2}\left(\frac{3}{8\pi}\right)^{1/2} \frac{1}{\gamma}\int_0^\infty db\, J_1(qb) e^{-g(b)} b \frac{dg}{db}$$

$$f_{\text{in}}(0^+, 0 \to 1^-, 1) = \frac{1}{2i}\lambda_1 \frac{E+mc^2}{\hbar^2 c^2}\left(\frac{3}{8\pi}\right)^{1/2} \frac{1}{\gamma}\int_0^\infty b\, db J_1(qb) \frac{d}{db}(1 - e^{-g(b)})$$

Integrating by parts yields

$$f_{\text{in}}(0^+, 0 \to 1^-, 1) = \frac{i}{2}\lambda_1 \frac{E+mc^2}{\hbar^2 c^2}\left(\frac{3}{8\pi}\right)^{1/2} \frac{q}{\gamma}\int_0^\infty b\, db\, J_0(qb)(1 - e^{-g(b)})$$

But the elastic scattering amplitude is

$$f^{\text{el}} = ik\int_0^\infty J_0(qb)(1 - e^{-g(b)}) b\, db$$

so that

$$f_{\text{in}}(0^+, 0 \to 1^-, 1) = \frac{1}{2}\lambda_1 \left(\frac{3}{8\pi}\right)^{1/2} \frac{E+mc^2}{\hbar^2 c^2}\frac{q}{\gamma k} f^{(\text{el})}$$

Finally, adding in the $M=-1$ case, we obtain‡

$$\sigma_{\text{in}}(0^+ \to 1^-) = \frac{3}{16\pi}\frac{q^2}{k^2}\left(\frac{\lambda_1}{\gamma}\frac{E+mc^2}{\hbar^2 c^2}\right)^2 \sigma_{\text{el}} \tag{5.16}$$

‡This equation and (5.17) differ from the Amado et al. result because of differing normalizations.

Amado, Lenz, McNeil, and Sparrow (80) have derived the relationship between the elastic and inelastic cross section for arbitrary L. It is

$$\sigma_{\text{in}}(0^+ \to I^\pi) = \left(\frac{\lambda_I}{\gamma}\right)^2 \frac{2I+1}{4\pi} B_0^{2(I-1)} \left(\frac{q}{k}\right)^2 \left(\frac{E+mc^2}{\hbar^2 c^2}\right)^2 e^{2\pi a \Phi_I/R} \sigma_{\text{el}}\left(\theta + \frac{\Phi_I}{kR}\right) \tag{5.17}$$

where $R + i\pi a = B_0 e^{i\phi}$ and $\Phi_I = (I-1)\phi + \eta$, where $\eta = 0$ for odd L and $\pi/2$ for even L, where ρ is given by $\rho_0[1 + \exp((r-R)/a)]^{-1}$. Comparison of (5.17) with experiment is illustrated in Fig. 5.3. Excellent agreement is obtained. [See also Feshbach and Boridy (74) for the KMT result.] The success of Tassie expression (5.14) indicates that the interactions responsible for the inelastic scattering occur in the surface. This is not surprising since the central potential is so strongly absorptive (see Fig. II.8.1).

Amado (85) also discusses the properties of the polarization parameters for elastic scattering. These turn out to be sensitive to the radial dependence of the spin-orbit terms. A difference in the radial dependence given by the nuclear density results in substantial differences in the polarization. We have already observed this phenomena earlier in this chapter (see Section 3). There one found

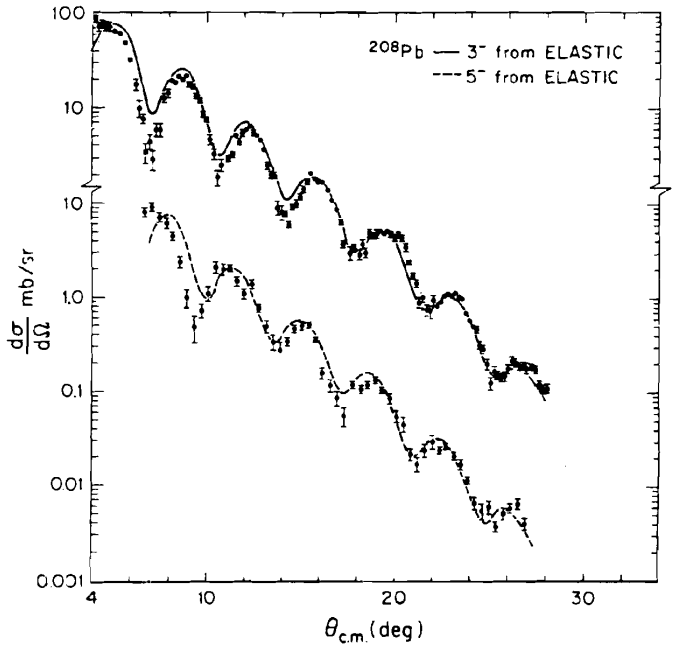

FIG. 5.3. Inelastic cross sections obtained from elastic scattering data (solid lines) compared with experiment. [From Amado (85).]

that adding in the interaction between the proton magnetic moment and the Coulomb field of the nucleus introduced oscillations into the asymmetry, for example, which brought the predictions in line with experiment. The reason for this sensitivity lies in the fact that the polarization parameters are ratios of various measured quantities to the differential cross section. For given interaction there can be correlations between the angular dependence of the numerator and that of the denominator. For example, at low energies there is the result obtained by Hüfner and de Shalit (65) that the polarization is proportional to the angular derivative of the angular distribution. At the higher energies, the nonoscillating behavior of the asymmetry (or Q) at the smaller angle must be a consequence of such a correlation. Adding in the magnetic moment Coulomb interaction or modifying the radial dependence in Amado's discussion destroyed the correlation since the angular distribution is not substantially modified by these changes. The oscillations of the numerator and the denominator are no longer in phase, so that new oscillations appear.

6. THE $(p, 2p)$ REACTION[‡]

The objectives of the studies of this process are similar to those of the study of the $(e, e'p)$ reaction—namely, to obtain information with regard to the hole state formed upon ejection of a target proton. In addition, one can hope to form some insight into the effect of the nuclear medium on the proton–proton interaction. There are substantial differences from the electron-induced reaction. Most important is the strong absorptive proton–nucleus interaction, which is to be compared with that of the relatively weak electron–nucleus interaction. In addition, the electron–proton interaction differs in character from that governing the proton–proton system.

The development to be presented here is suggested by the procedure used to discuss the $(e, e'p)$ reaction discussed earlier in this chapter. This is not the traditional procedure. I refer the reader to the reviews by Barrett and Jackson (77) and Kitching, McDonald, Maris, and Vasconcellos (85) for a description of that procedure. The model to be used is shown in Fig. 6.1 (compare with

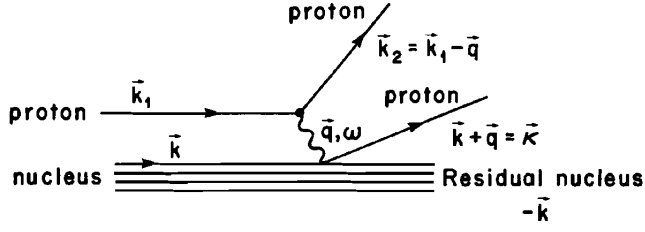

FIG. 6.1. The $(p, 2p)$ reaction.

[‡]Barrett and Jackson (77); Kitching, McDonald, Maris, Vasconcellos (85).

Fig. 2.17). The incident proton with momentum $\mathbf{k}_1$ interacts with a target proton with momentum $\mathbf{k}$ whose momentum and energy are increased by $\mathbf{q}$ and $\hbar\omega$, respectively. The scattered incident proton has the momentum $\mathbf{k}_2 = \mathbf{k}_1 - \mathbf{q}$. The residual nucleus will have a momentum of $-\mathbf{k}$ but may be excited to an energy ε. The model assumes that we are dealing with a single-step direct reaction. Conservation of energy requires that

$$\hbar\omega = \frac{\hbar^2}{2m}k_1^2 - \frac{\hbar^2}{2m}(\mathbf{k}_1 - \mathbf{q})^2 = \frac{\hbar^2}{m}(\mathbf{k}_1 \cdot \mathbf{q}) - \frac{\hbar^2}{2m}q^2 \tag{6.1}$$

and

$$\hbar\omega = \varepsilon + \frac{\hbar^2}{2m}(\mathbf{k} + \mathbf{q})^2 - \frac{\hbar^2 k^2}{2m} \tag{6.2}$$

By measuring $\mathbf{k}_2$ and $(\mathbf{k} + \mathbf{q})$, one can obtain ε. Figure 6.2 shows a plot of the cross section versus ε for the reaction $^{16}O(p, 2p)^{15}N$, for incident proton energy of 460 MeV. The hole states $s_{1/2}^{-1}$, $p_{1/2}^{-1}$, and $p_{3/2}^{-1}$ are clearly visible. A summary of the results obtained using a variety of targets is shown in Fig. 6.3.

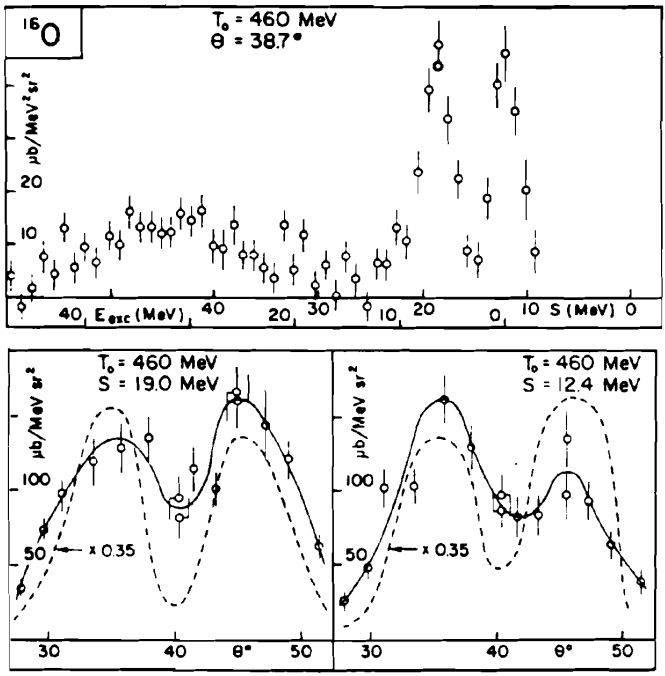

FIG. 6.2. Energy spectrum and angular correlations for the reaction $^{16}O(p, 2p)^{15}N$. The dashed lines are calculated results multiplied by the indicated factor. [From Kitching, McDonald, Maris, and Vasconcellos (85).]

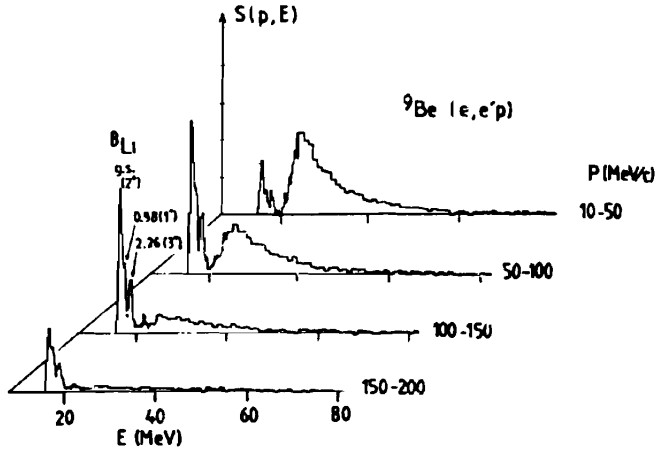

FIG. 6.3. Momentum distributions for the reaction $^9\text{Be}(e,e'p)^8\text{Li}$. The p and s states are at $E \simeq 15$ and 25 MeV, respectively. [From Kitching, McDonald, Maris, and Vasconcellos (85).]

The cross section for the inclusive $(p, 2p)$ process is

$$\frac{d^2\sigma}{dE_2\, d\Omega_2} = \left[\frac{\mathscr{E}^2 - m^2c^4}{2\pi\hbar^2c^2E_L^{(p)}}\right]^2 \times \sum_f |\langle \chi_f^{(-)}(\mathbf{k}_2)\phi^{(-)}(\boldsymbol{\kappa})\Psi_f | (A-1)\hat{\rho}(\mathbf{q})t(\mathbf{q})|\chi_i^{(+)}(\mathbf{k}_1)\Psi_i\rangle|^2 \times \delta(E_i - E_f) \tag{6.3}$$

where $\mathscr{E}$ is the energy of the incident proton $E_L^{(p)}$ plus the proton rest mass mc^2, $E_i - E_f = E_L^{(p)} - (\hbar^2/2m)k_2^2 - (\hbar^2/2m)\kappa^2 - \varepsilon$, neglecting the recoil kinetic energy of the residual nucleus. The initial and final nuclear wave functions are Ψ_i and Ψ_f, respectively. If we drop the spin-dependent terms in $t(\mathbf{q})$ and assume that $t(\mathbf{q})$ varies so slowly that it can be removed from the matrix element in (6.3), we have

$$\frac{d^2\sigma}{dE_2\, d\Omega_2} = \left[\frac{\mathscr{E}^2 - m^2c^4}{2\pi\hbar^2c^2E_L^{(p)}}\right]^2 |\langle \chi_f^{(-)} t(\mathbf{q}) \chi_i^{(+)}\rangle|^2 (A-1)^2 \times \sum |\langle \phi^{(-)}(\boldsymbol{\kappa})\Psi_f | \hat{\rho}\Psi_i\rangle|^2 \delta(E_i - E_f)$$

The first two factors can be combined to give an effective pp cross section, $d\sigma_{\text{eff}}^{(pp)}/dE_2\, d\Omega_2$. It is not identical to the free proton–proton cross section since χ_i and χ_f are distorted waves as a consequence of their interaction with the target and residual nuclei, respectively. The factor that remains is just R_L, the

longitudinal response function of (2.118*a*). Therefore,

$$\frac{d^2\sigma}{d\Omega_2\, dE_2} = \frac{d^2\sigma_{\text{eff}}^{(p,p)}}{d\Omega_2\, dE_2}(A-1)^2 R_L \tag{6.4}$$

relating the inclusive $(e,e'P)$ and $(p,2p)$ cross sections. If one includes the spin-dependent terms, one will obtain other response functions which are also present in the expression for $(e,e'p)$ polarization parameters.

7. RELATIVISTIC HEAVY IONS

In this section we consider the collision of heavy ions with nuclei with energies of the order of 1 GeV/A. These experiments have been for the most part performed at the Bevalac, the heavy-ion accelerator at the Lawrence Berkeley Laboratory, which produces beams of heavy ions with a maximum energy of 2.1 GeV/A. In Section 8 we briefly discuss collisions of protons and heavy ions with energies in the hundreds of GeV/A range. These are referred to as *ultra-relativistic heavy ions.*

Experimentally, two types of collisions could be differentiated, the *peripheral* and the *central.* In the first of these, the fragments move with nearly the same velocity as the incident projectile, and nearly in the forward direction in the laboratory reference frame. These fragments were ejected from the incident projectile by its interaction with the target nucleus. The impact parameter for these collisions are relatively large; the momentum transfer relatively small. The central collision is characterized by a high multiplicity, as one would intuitively expect. This is illustrated by Fig. 7.1, obtained by the internuclear cascade method. We see that high multiplicity is present for relatively small impact parameters, the nuclei "exploding" upon collision. This multiparticle final state involving many particles is a new feature that makes its appearance at relativistic energies (and at ultrarelativistic energies for even nucleon–nucleon collisions).

A. Peripheral Collisions

Peripheral collisions will be discussed first. As we shall see, this is essentially a low-energy phenomenon that can be understood rather directly in terms of small energy and momentum transfers to the projectile nucleus. Let us summarize the experimental facts obtained by experiments performed at the Bevalac facility. Experiments were performed with a beam of energetic projectiles (e.g., ^{16}O) at energies of 1.05 GeV/A and 2.1 GeV/A. Inclusive cross sections, that is, cross sections for the production of a particular nuclear fragment without a determination of the correlated production of other fragments, were measured. The results obtained are most simply expressed with respect to the projectile frame of reference defined as that frame in which the incident projectile is at rest and the target nuclei effectively form the incident beam.

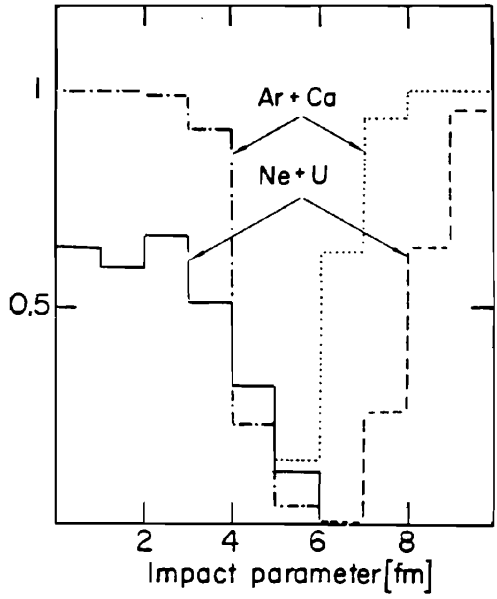

FIG. 7.1. Ratio of the multiplicity-selected proton inclusive cross section to the total proton inclusive cross section as a function of impact parameter. The solid line represents the $\sigma_{m\geq 20}/\sigma_{\text{tot}}$ ratio for $^{20}\text{Ne} + ^{238}\text{U}$ at $E/A = 400$ MeV and the dashed line represents the ratio $\sigma_{m\leq 8}/\sigma_{\text{tot}}$ for the same reaction. The dashed–dotted line represents the ratio $\sigma_{m\geq 20}/\sigma_{\text{tot}}$ for $^{40}\text{Ar} + ^{40}\text{Ca}$ at $E/A = 1050$ MeV and the dotted line represents the ratio $\sigma_{m\leq 5}/\sigma_{\text{tot}}$ for the same reaction. [From Yariv and Fraenkel (81).]

1. In the projectile frame, the momentum of a fragment is relatively small. For example, if the target nucleus is Pb, its momentum in the projectile frame is $208 \times 2.9 \sim 601$ GeV/c when the projectile has an energy of 2.1 GeV/A. The longitudinal-momentum, p_L, distribution of ^{10}Be fragments produced by fragmentation of the projectile, ^{12}C, in the projectile frame is shown in Fig. 7.2. We see that the ^{10}Be average longitudinal momentum is only about 50 MeV/c, while the dispersion of the p_L distribution is about 100 MeV/c, which should be compared with the 601,000 MeV/c carried by the Pb nucleus. Thus a very small fraction (10^{-4}) of the momentum of the lead nucleus is transferred to the projectile.
2. The distribution, $\omega(p_L, \mathbf{p}_T)$, in the longitudinal, p_L, and transverse, $\mathbf{p}_T$, components of the momentum is Gaussian in each. Empirically, one finds that

$$\omega(p_L, \mathbf{p}_T) \sim \exp\left\{-\left[\frac{1}{2\sigma_L^2}(p_L - \bar{p}_L)^2 + \frac{1}{2\sigma_T^2}p_T^2\right]\right\} \tag{7.1}$$

where as mentioned above, $\bar{p}_L$ is generally several tens of MeV/c.

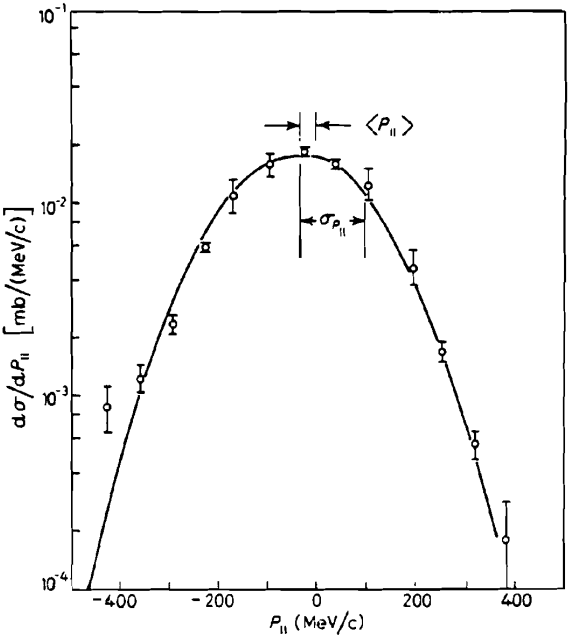

FIG. 7.2. Longitudinal-momentum distribution in the projectile frame of reference of the ^{10}Be fragments produced by the fragmentation of a ^{12}C projectile with an energy of 2.1 GeV/nucleon. [From Greiner, Lindstrom, et al. (75).]

3. The angular distribution is approximately isotropic, that is,

$$\sigma_L \simeq \sigma_T \tag{7.2}$$

However, because of the much greater experimental difficulty in the determination of the transverse momenta, (7.2) must be considered as approximate.

4. The dispersion, σ_L, is empirically independent of A_T (the target mass number), depending only on A_F (the fragment mass number) and A_P (the projectile mass number). This is a first example of independence of the projectile fragmentation of A_T.
5. A second is given by the fact that the branching ratio for the relative probability for the production of a fragment type is independent of the target nucleus. The cross section for the production of a fragment F, upon the collision of a target T with a projectile P, is found to be

$$\sigma_{PT}^{(F)} = \sigma_{PT} \frac{\gamma_P^{(F)}}{\gamma_P} \qquad \text{where } \sum_F \gamma_P^{(F)} = \gamma_P \tag{7.3}$$

The ratio multiplying σ_{PT} is the branching ratio for the production of fragment F.

6. The inclusive cross section σ_{incl} is proportional to the radius of the interaction. Empirically,

$$\sigma_{\text{incl}} \sim A_P^{1/3} + A_T^{1/3} - 0.8 \tag{7.4}$$

7. Cross sections and σ_L at 1.05 and 2.1 GeV/A are approximately the same, indicating within this energy range, independence with respect to the energy (see Fig. 7.3).
8. The momentum distribution of the emerging protons is not Gaussian. It is better described by an exponential, $\exp(-p/p_0)$, where $p_0 \sim 65$ MeV/c.

We shall now discuss the momentum distribution of the fragments.

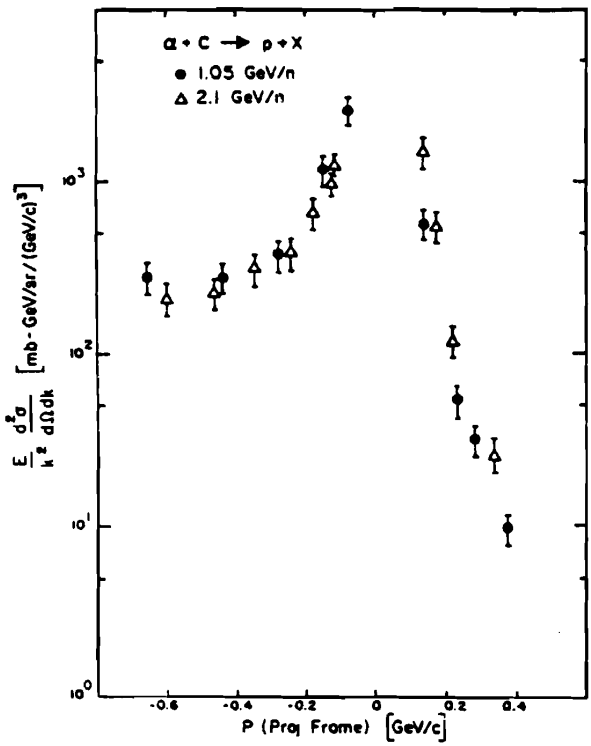

FIG. 7.3. Lorentz invariant cross section for an α beam of indicated energies fragmenting to protons versus the proton momentum in the projectile rest frame. [From Schroeder (76).]

Momentum Distribution of Projectile Fragments. The model we use was suggested by Feshbach and Huang (73). The derivation employed below follows essentially that of Goldhaber (74*b*). The model assumes that the fragment of mass number A_F is formed from the projectile of mass A_P by removing the binding of a group of A_F nucleons. The net momentum $\mathbf{P}_F$ of the fragment is then obtained by adding up the momentum of each of these nucleons. The value of $\mathbf{P}_F$ will vary according to which group of A_F nucleons is selected from the projectile giving rise to a distribution in $\mathbf{P}_F$. If the mean-square momentum of a nucleon in the projectile is $\langle p^2 \rangle$, the mean-square value of $\mathbf{P}_F$ is, according to a simple statistical consideration,[‡] given by $A_F \langle p^2 \rangle$. The distribution in $\mathbf{P}_F$, following again from statistical considerations, is Gaussian[§] at least in the neighborhood of the maximum of the distribution. This occurs near $P_F = 0$, since the average momentum of the fragments is so close to zero. Note that this model automatically assumes that the projectile fragment distribution does not depend on the nature of the target.

Suppose then that the projectiles breaks up into fragments of mass number A_i, so that

$$\sum A_i = A_P \tag{7.5}$$

Let the momentum of each fragment be $\mathbf{P}_i$. Assume that the distribution of momenta for the ith fragment depends only on $\mathbf{P}_i$, and is Gaussian. Then the momentum distribution, ω, for a given set of A_i, is

$$\omega(\mathbf{P}_1, \mathbf{P}_2, \ldots) \sim \prod_i \exp\left[-\frac{\frac{2}{3} P_i^2}{A_i \langle p^2 \rangle} \right] \tag{7.6}$$

To obtain the observed inclusive momentum distribution, we must integrate over all momenta except that of the observed fragment, say A_1, subject to the condition

$$\sum_i \mathbf{P}_i = 0 \tag{7.7}$$

As shown by experiment, the average momentum of a projectile fragment in the projectile frame of reference is very small, justifying (7.7) to some extent.

[‡]Assume that $\mathbf{P}_F = \sum \mathbf{p}_\mu$, where $\mathbf{p}_\mu$ are the momenta of the nucleons making up the fragment. Then $P_F^2 = \sum p_\mu^2 + \sum_{\mu \neq \nu} \mathbf{p}_\mu \cdot \mathbf{p}_\nu$. Averaging over the momentum distribution of the projectile nucleons, we find that $\langle \sum_{\mu \neq \nu} \mathbf{p}_\mu \cdot \mathbf{p}_\nu \rangle = 0$. Hence

$$\langle P_F^2 \rangle = \left\langle \sum_\mu p_\mu^2 \right\rangle = A_F \langle p^2 \rangle$$

[§]This result follows simply from the assumption that the momentum distribution is symmetric about the maximum.

Hence the single-fragment distribution, $\omega(\mathbf{P}_1)$, is given by

$$\omega(\mathbf{P}_1) = \int \omega(\mathbf{P}_1, \mathbf{P}_2, \ldots)\delta(\sum \mathbf{P}_i)\, d\mathbf{P}_2 \cdots \tag{7.8}$$

This integral may be easily performed to yield

$$\omega(\mathbf{P}_1) \sim \exp\left(-\frac{P_1^2}{2\sigma^2}\right) \tag{7.9}$$

where

$$\sigma^2 = \tfrac{1}{3}\langle p^2\rangle \frac{(A_P - A_F)}{A_P} A_F \tag{7.10}$$

If we adopt the Fermi-gas model as a description of the projectile nucleus,

$$\tfrac{1}{3}\langle p^2\rangle = \tfrac{1}{5}p_F^2 \tag{7.11}$$

where p_F is the Fermi momentum.

The experimental results are shown in Fig. 7.4. As can be seen from the figure, the dependence of σ^2 on A_P and A_F, given by (7.10), is verified by experimental data. However, those data yield a value for p_F [according to (7.10)] equal to 190 Mev/c, whereas the value of p_F determined from quasi-elastic electron scattering is, for ^{16}O, given by 225 MeV/c. As suggested by Hüfner, this discrepancy may occur because fragmentation occurs only after the emission of a number of nucleons. The fragmenting nucleus is not ^{16}O but a lighter nucleus with a correspondingly lower value of p_F.

The distribution given by (7.6) can also be used to calculate the angular correlation between two fragments, A_1 and A_2, which exists in virtue of (7.7). One obtains

$$\omega(\mathbf{P}_1, \mathbf{P}_2) \sim \exp\left[-\frac{2}{3\langle p^2\rangle}\frac{1}{A_P - A_1 - A_2}\left(P_1^2\frac{A_P - A_2}{A_1} + P_2^2\frac{A_P - A_1}{A_2} + 2\mathbf{P}_1\cdot\mathbf{P}_2\right)\right]$$

This implies a greater probability for the two fragments to go off in opposite directions. Determination of this angular correlation would provide a test of the independence hypothesis as formalized by (7.6). It appears, however, to be very difficult to carry out this experiment.

The Nuclear Weizsäcker–Williams Method [Feshbach and Zabek (77)]. The Weizsäcker–Williams method relates the reaction cross section induced by a charged particle to that induced by a distribution of photons. The electromagnetic field of a rapidly moving charged particle can be shown to be

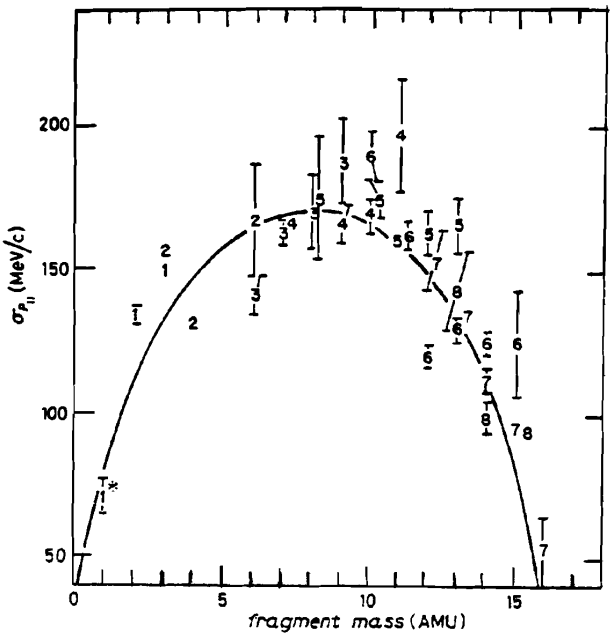

FIG. 7.4. Target averaged values of the dispersion σ of the longitudinal-momentum distribution in the projectile frame. The plotted numeral gives the charge of the fragment. The projectile is ^{16}O with an energy of 2.1 GeV/nucleon. The solid line is a best fit using (7.10). [From Greiner, Lindstrom, et al. (75).]

approximately equivalent to a beam of photons with the frequency distribution

$$n(\omega)\,d\omega = \frac{2}{\pi}(Z\alpha)^2\frac{d\omega}{\omega} \tag{7.12}$$

where Z is the charge of the particle and α is the fine-structure constant. The cross section for the reaction induced by a charged particle is then given in terms of the cross section $\sigma_\gamma(\omega)$ for the photon-induced reaction by

$$\sigma = \int n(\omega)\sigma_\gamma(\omega)\,d\omega = \frac{2}{\pi}(Z\alpha)^2\int\frac{\sigma_\gamma(\omega)}{\omega}d\omega \tag{7.13}$$

In this section a theory of the fragmentation of a relativistic heavy-ion projectile will be developed. The expression for the cross section which will be obtained will have a structure similar to that of (7.13), so that the theory will be referred to as the *nuclear Weizsäcker–Williams method.*

The projectile reference frame will be used. In that frame it will be assumed that the target nucleus travels without deviation and without internal excitation

in a straight line. This assumption is indicated by experimental result (1), which demonstrates that the momentum transferred to the projectile nucleus by the target nucleus is small. It is identical with the assumptions made in developing the electromagnetic Weiszäcker–Williams result. However, after the target nuclei have penetrated into the projectile a distance λ approximately equal to a nucleon mean free path, a strong collision with large momentum transfer will occur. This collision will not contribute to the process being considered, since the reaction products will fall outside the small forward cone where the fragments were detected. This competitive process is taken into account by assuming that the probability of finding the target nucleus intact attentuates during the collision with a scale measured by the mean free path λ.

It is assumed that the collision is peripheral. This result is implied very directly by experimental result 6, as given by (7.4). The mean free path λ used is the value valid on the surface region of the interacting nuclei.

A qualitative description of the consequences of these assumptions can be given. The projectile nucleon feel a pulse of force as the target nucleus passes by. The duration of the pulse, τ, is given by the scale, λ, Lorentz contracted to λ/γ, divided by the velocity of the projectile, v, which is very close to c, the velocity of light. Thus

$$\tau \sim \frac{\lambda}{\gamma v} \tag{7.14}$$

where

$$\gamma = \left(1 - \frac{v^2}{c^2}\right)^{-1/2} = \frac{E}{mA_T}$$

where v is the velocity of the target and E its energy. From the duration of the pulse one can calculate the maximum‡ energy transfer $\hbar\omega_c$ that can occur:

$$\hbar\omega_c \sim \frac{\hbar}{\tau} = \frac{\gamma\hbar v}{\lambda} \tag{7.15}$$

For a target energy of 2.1 GeV/A and $\lambda = 1.75$ fm, the maximum energy transfer is found from this equation to be 365 MeV. We see immediately that we are in fact dealing with a comparatively low-energy phenomenon. There will be other effects to be discussed below, which will reduce the maximum energy transfer to even considerably lower values.

Following an argument of Guet, Soyeur, Bowlein, and Brown (89), one can establish a relation between the energy transfer $\hbar\omega$ and the longitudinal momentum transfer $\hbar q_L$. Let E_i and p_i be the initial four-momentum of the

‡By "maximum" we shall mean the value of $\hbar\omega$ at which the cross section is $1/e$ of its value for very small values of $\hbar\omega$.

target and E_f and p_f its corresponding final four momentum, so that

$$\hbar\omega = E_i - E_f$$

and

$$\mathbf{q} = \mathbf{p}_i - \mathbf{p}_f$$

Then one can immediately obtain

$$\frac{\mathbf{p}_i \cdot \mathbf{q}}{E_i} - \hbar\omega = \frac{-(\hbar\omega)^2 + q^2 + (M_f^2 - M_i^2)}{E_i}$$

For sufficiently large E_i and small momentum and energy transfer, one can neglect the terms on the right-hand side of this equation so that

$$\frac{\mathbf{p}_i}{E_i} \cdot \mathbf{q} \simeq \hbar\omega$$

or

$$q_L \simeq \frac{\hbar\omega}{v} \tag{7.16}$$

The error in approximation leading to (7.16) is on the order of $\hbar\omega/E_i$ and therefore small.

The maximum value of transverse-momentum transfer, $\hbar q_T$, is determined by the transverse scale of the target density, namely a, the parameter measuring the thickness of the nuclear surface. The maximum transverse-momentum transfer is thus

$$\hbar q_{T,c} \sim \frac{\hbar}{a}$$

For $a \sim 0.6$ fm, $\hbar q_{T,c}$ is about 333 MeV/c.

In addition to these cutoffs in q_T and q_L, which come from the shape of the interacting nuclei, additional cutoffs that have a dynamic origin must be taken into account. The most obvious of these is the momentum transfer, which the nucleon–nucleon potential will allow before a substantial reduction in the amplitude will occur. From the empirical expression for the nucleon–nucleon amplitude, we find that the nucleon–nucleon potential produces a momentum cutoff, for both the transverse and longitudinal components, of 370 MeV/c.

The two factors so far described, the geometric factor and the potential factor, when combined, yield a momentum cutoff for both components of about 260 MeV/c.

Finally, it is necessary to consider the ability of the projectile nucleus to absorb the energy $\hbar\omega$ and the momentum $\hbar q$. If the energy is absorbed by a single nucleon, it will be very far off the energy shell. If it absorbs the full energy

$\hbar\omega$, it will have a momentum $\sqrt{2m\hbar\omega}$. This, however, is very much larger than the momentum transferred, which, as we have seen, is on the order of $\hbar\omega/c$, that is,

$$\sqrt{2m\hbar\omega} \gg \frac{\hbar\omega}{c}$$

or

$$\sqrt{\frac{\hbar\omega}{2mc^2}} \ll 1 \tag{7.17}$$

This inequality is satisfied by the $\hbar\omega$ of interest, that is, $\hbar\omega < 260$ MeV. The absorbing nucleon must therefore interact with a second nucleon in the projectile. This absorption by two nucleons can proceed because it is then possible to conserve both momentum and energy. The momenta of the two nucleons will be opposite and nearly equal, so that the total momentum is small, but the total energy will be a sum of the energies of each nucleon.

The probability for two-nucleon absorption will therefore depend critically on the correlation length r_c, the mean distance between the first nucleon and the second. From the uncertainty principle, the lifetime of the nucleon absorbing the momentum and energy is on the order of $1/\omega$. This nucleon moves with a velocity equal to $\sqrt{(2/m)\hbar\omega}$ and thus covers in the time $1/\omega$ the distance $\sqrt{2\hbar/m\omega}$. This distance must be of the order of or greater than r_c:

$$\left(\frac{2\hbar}{m\omega}\right)^{1/2} > r_c$$

or

$$\hbar\omega < \frac{2\hbar^2}{mr_c^2} \tag{7.18}$$

If we take r_c as $1/2(\hbar/m_\pi c)$, one-half of the pion Compton wavelength, this inequality becomes

$$\hbar\omega < 165 \text{ MeV} \tag{7.19}$$

Combining this result with the geometric and interaction potential gives a longitudinal-momentum cutoff of 139 MeV/c, of the same order as the experimental value. It also implies a maximum value of the energy that can be transferred to the projectile equal to 139 MeV. This energy is split between the two absorbing nucleons, so that the cutoff energy for one of these nucleons is approximately 70 MeV and the cutoff momentum on the order of 70 MeV/c.‡

‡It has been suggested by Goldhaber that in addition to the two-nucleon mechanism, there is the possibility of nucleon excitation to form a Δ. However, the momentum change would then be on the order of 300 MeV/c. This combined with the other factors would yield a cutoff of 190 MeV/c, which would be too large to explain the fragmentation data. However, as Guet, Soyeur, Bowlein, and Brown (89) have shown, it is an important mechanism for pion production.

The low value of the momentum transferred ($\sim \hbar\omega/c$) indicates that the angular distribution of the nucleons will be roughly isotropic in the projectile frame. In the collision of the two nucleons as discussed above, their final linear momentum is $\hbar\omega/c$, so that their angular momentum $l\hbar$ is on the order of $(\hbar\omega/c)r_c$. Hence

$$l \leqslant \frac{\hbar\omega r_c}{\hbar c} \tag{7.20}$$

Inserting a maximum value for $\hbar\omega$ of 139 MeV and $r_c = 0.7$ fm yields

$$l \leqslant 0.5 \tag{7.21}$$

demonstrating that for nearly all values of $\hbar\omega$ the angular distribution of the nucleon pair will be isotropic.[§]

These qualitative considerations provide a simple explanation of the projectile fragmentation as a consequence of the action of the "fringing field" of the target nucleus as it moves past the projectile. Our principal conclusion is that the process is essentially a low-energy phenomenon. The energy of the nucleon pairs produced is predicted to have the observed order of magnitude. These nucleons will deposit energy within the projectile nucleus and by that means fragmenting it. The net maximum momentum that can be transferred is calculated to be of the experimental order of magnitude. A rough isotropy is also predicted. Energy dependence in the GeV/A range is weak, since the energy occurs only in the geometric cutoff given by (7.15). As observed, the cutoff energy is changed by only a few percent when the heavy-ion energy is changed from 2.1 GeV/A to 1.05 GeV/A, since the dynamical conditions, (7.18), and the limits imposed by the nucleon–nucleon potential are energy independent in this range of energy. Finally, it should be observed that none of the cutoff conditions depend on the target nucleus. This does indicate that the width of the momentum distribution of the fragments is independent of the target. It is obviously a necessary condition for showing that the branching ratios are target nucleus independent. The quantitative calculation we report below shows that indeed the nucleon spectrum, and therefore the projectile fragmentation, are target independent.

We turn now to the nuclear Weizsäcker–Williams method. The projectile frame of reference will be used so that the incident system is the target nucleus. As in the Coulomb case, the target nucleus is assumed to continue to move in a straight line along the incident direction. It is also assumed that the interaction provided by the long-range component of the nuclear field, the *fringing field*, is weak. We may therefore use first-order perturbation theory.

[§]Actual calculation shows, in fact, that this estimate is overgenerous and that the maximum value of l is considerably smaller than that given by (7.21).

Let the coordinates of the target nucleus relative to its center of mass be given by ξ_T and its internal wave functions by $\chi(\xi_T)$. Similarly, the coordinates of the projectile nucleus relative to its center of mass are given by ξ_P and its internal wave functions by $\psi(\xi_P)$. The vector between the center of mass of each of the nuclei, $\mathbf{r}$, has components z and $\mathbf{b}$, where z is in the direction of motion of the target nucleus and $\mathbf{b}$ is transverse to that direction.

The wave function of the system has the following form:

$$\psi = \chi_0(\xi_T)\sum_\alpha \psi_a(\xi_P)\Phi_\alpha(\mathbf{r}, t)e^{-i/\hbar E_\alpha t} \tag{7.22}$$

where χ_0 is the ground-state target wave function, and ψ_α describes the internal states of the projectile and E_α their energies. The function Φ_α is the wave function for the relative motion of the target and projectile. Inserting (7.22) into the time-dependent Schrödinger equation yields an equation for Φ_β:

$$\frac{i\hbar\partial\Phi_\beta}{\partial t} = \sum_\alpha \langle\chi_0\psi_\beta|V|\psi_\alpha\chi_0\rangle\Phi_\alpha e^{i\omega_{\alpha\beta}t}$$

$$\omega_{\alpha\beta} \equiv E_\beta - E_\alpha \tag{7.23}$$

We now insert the assumption that the z component of the velocity of the target nucleus is unchanged during the course of the collision:

$$\Phi_\beta = u(z, t)\phi_\beta(\mathbf{b}, t) \tag{7.24}$$

with

$$|u|^2 = \delta(z - vt) \qquad \int |u|^2\, dz = 1 \tag{7.25}$$

Inserting (7.24) into (7.23) yields

$$\frac{i\hbar\partial\phi_\beta}{\partial t} = \sum_\alpha \langle\psi_\beta|(V\rho_T|u|^2)\psi_\alpha\rangle\phi_\alpha(\mathbf{b}, t)e^{i\omega_{\alpha\beta}t} \tag{7.26}$$

where

$$(V\rho_T|u|^2) = \int V|\chi_0|^2|u|^2 d\xi_T\, dz \tag{7.27}$$

We use first-order perturbation theory to solve (7.26), that in, we assume that ϕ_α on the right-hand side of (7.26) has its initial value

$$\phi_\alpha = \delta_{\alpha i} \tag{7.28}$$

The probability $P_{\beta i}$ that the projectile makes a transition from its initial state

ψ_i to a final state ψ_β is

$$P_{\beta i} = \frac{2\pi}{\hbar^2}|F_\beta(\omega_{\beta i})|^2 \tag{7.29}$$

where $\hbar\omega_{\beta i}$ is the energy transfer and

$$F_{\beta i}(\omega) = \langle \phi_\beta \psi_\beta | U | \phi_i \psi_i \rangle \tag{7.30}$$

The function U is

$$U(\mathbf{b}, \xi_P, \omega) = \frac{\gamma}{2\pi}\int dt\, e^{i\omega t}\int dz \int d\xi_T \rho_T(\mathbf{b}_T, \gamma z_T)|u|^2 V \tag{7.31}$$

where

$$\gamma = \frac{1}{\sqrt{1 - v^2/c^2}}$$

The factor γ in (7.31) takes into account the relativistic contraction of length. Inserting (7.25) for $|u|^2$ and integrating over time yields

$$U(\mathbf{b}, \xi_P, \omega) = \frac{\gamma}{2\pi v}\int dz\, e^{-i\omega z/v}\int d\xi_T \rho_T(\mathbf{b}_T, \gamma z_T) V \tag{7.32}$$

Taking V to be a central potential acting between a nucleon in the target and a nucleon in the projectile summed over all pairs, V has the general form

$$V = V(\mathbf{r} + \xi_T - \xi_P) \tag{7.33}$$

Let

$$\zeta = z + z_T - z_P$$

$$\boldsymbol{\beta} = \mathbf{b} + \mathbf{b}_T - \mathbf{b}_P$$

Then

$$U(\mathbf{b}, \xi_P, \omega) = \frac{\gamma}{2\pi v} e^{i\omega z_P/v}\int d\zeta \int d\xi_T e^{i\omega(\zeta - z_T)/v}\rho_T(\mathbf{b}_T, \gamma z_T) V(\zeta, \boldsymbol{\beta}) \tag{7.34}$$

demonstrating that the longitudinal momentum transferred to a projectile nucleon is $\hbar\omega/v$. Finally, from (7.30) it is necessary to evaluate $\langle \phi_\beta | U | \phi_i \rangle$. Taking ϕ_i from (7.28) and

$$\phi_\beta = e^{i\mathbf{k}\cdot\mathbf{b}} \tag{7.35}$$

where $\mathbf{k}$ is the transverse momentum transfer, one obtains

$$\langle \phi_\beta | U | \phi_i \rangle = \frac{1}{2\pi v} e^{i(\omega z/v - \mathbf{k}\cdot\mathbf{b}_P)}\tilde{\rho}_T\left(\mathbf{k}, -\frac{\omega}{\gamma v}\right)\tilde{V}\left(-\mathbf{k}, \frac{\omega}{v}\right) \tag{7.36}$$

where the tilde indicates the Fourier transform, so that

$$\tilde{V}\left(-\mathbf{k}, \frac{\omega}{v}\right) = \int V(\boldsymbol{\beta}, \zeta) e^{-i\mathbf{k}\cdot\boldsymbol{\beta} + i\omega\zeta/v} \, d\boldsymbol{\beta} \, d\zeta \tag{7.37}$$

As a consequence of these results the matrix element $F_{\beta i}$ factorizes into a product of two terms, one of which depends only on the properties of the projectile, the other on those of the target.

$$F_{\beta i} = F_{\beta i}^{(P)}\left(-\mathbf{k}, \frac{\omega}{v}\right) F^{(T)}\left(\mathbf{k}, \frac{\omega}{v}\right)$$

where

$$F^{(T)}\left(\mathbf{k}, \frac{\omega}{v}\right) \equiv \frac{1}{2\pi v} \tilde{\rho}_T\left(\mathbf{k}, -\frac{\omega}{\gamma v}\right) \tilde{V}\left(-\mathbf{k}, \frac{\omega}{v}\right) \tag{7.38}$$

$$F^{(P)}(\mathbf{q}) \equiv \langle \psi_\beta | e^{i\mathbf{q}\cdot\boldsymbol{\xi}_P} | \psi_i \rangle \qquad \mathbf{q} = \left(-\mathbf{k}, \frac{\omega}{v}\right) \tag{7.39}$$

The projectile factor involves a sum over the projectile nucleon coordinates and thus equals the projectiles transition density. $F^{(T)}$ is independent of the transition induced in the projectile. From the point of the projectile, the target acts as a source of "phonons" with momentum $\mathbf{q}$ and energy $\hbar\omega$. The total cross section is obtained by integrating the probability that a transition from ψ_i to ψ_β is induced by a phonon of momentum $\mathbf{q}$ over the number density of such phonons. Thus

$$\sigma_T = \frac{1}{\hbar^2} \int \rho_\beta \, dE_\beta \, d\mathbf{k} \, d\omega \left| F_{\beta i}^{(P)}\left(-\mathbf{k}, \frac{\omega}{v}\right) \right|^2 \left| F^{(T)}\left(\mathbf{k}, \frac{\omega}{v}\right) \right|^2 \delta(\omega - \omega_{\beta i}) \tag{7.40}$$

where ρ_β is the density of final states. We have therefore referred to this procedure as the nuclear Weiszäcker–Williams method.

We shall not develop this procedure further, as all that is required is the calculation of $F^{(T)}$ and $F^{(P)}$. For details the reader is referred to the original articles [Feshbach and Zabek (77); Feshbach (81)]. It is found that the anisotropy of the angular distribution is governed by a small parameter:

$$\frac{1}{4}\left(\frac{mc^2}{\hbar c}\right)\left(\frac{\hbar\omega r_c}{\hbar c}\right)^4$$

which equals 0.068 for $r_c = 0.7$ fm and $\hbar\omega = 140$ MeV. The cross section is proportional to $A_T^{1/3}$. It is sensitive to the value of the correlation length, r_c. Reasonable values are obtained for $r_c \sim 0.7$.

To obtain the partial cross sections, the two particles ejected by the phonon are followed using cascade theory. Finally, one must add the effect of a single particle ejection for the total branching ratio. Good agreement with experment is obtained [Feshbach (81)]. This process has also been treated as an "abrasion–ablation" process by Hüfner (75) and collaborators. The method described here has been generalized by Guet, Soyeur, Bowlein, and Brown (89) and used to discuss subthreshold pion production in ^{12}C–^{12}C collisions at a projectile energy of 95 MeV/A.

B. Central Collisions[‡]

A number of different theoretical descriptions of the central, high-multiplicity collisions have been proposed. Some of these such as the fireball–firestreak thermal models [Westfall, Gosset, et al. (76); Myers (78)] and the hydrodynamic models [Amsden, Harlow, and Niu (77); Amsden, Goldhaber, Harlow, and Niu (78); Stöcker and Greiner (86)] presume the existence of thermal equilibrium. Others, such as Koonin (77), have shown that a significant fraction of the observed cross section is a consequence of direct knockout of a preequilibrium nature. Classical or semiclassical procedures are employed by the models of Hüfner and Knoll (77), Wilets et al. (77), Bodmer and Panos (77), and finally the internucleon cascade mode of Yariv and Fraenkel (79, 81) and Cugnon (80, 81). We shall limit the discussion below to a description of the internuclear cascade model, an important technique that permits detailed calculation of many of the observed phenomena. None of the models are completely successful, but the internucleon cascade does quite well for many situations. Perhaps its most significant failure is the prediction of the directed flow momenta, which it underestimates by a factor of 2 while the hydrodynamic model errs by its overestimate of the flow by a factor of 2 [Stöcker and Greiner (86); Cugnon (82)].

The internuclear cascade (INC) follows the passage of a nucleon (or group of nucleons) through a target nucleus assuming two-body collisions. In one method [Chen et al. (68); Yariv and Fraenkel (79, 81)] the target nucleus is represented by a continuous fluid whose density is obtained, for example, from electron scattering. The probability that a target nucleon has a momentum $\mathbf{p}$ at a point $\mathbf{r}$ is given by the Fermi-gas distribution corresponding to the density $\rho(\mathbf{r})$. Attention is focused on the projectile motion during the time it could travel a distance $\bar{\lambda}/n$, where $\bar{\lambda}$ is an estimated mean free path and n is on the order of 20. The first step is randomly to select a nucleon from the Fermi gas, which is to interact with the projectile nucleon. The next step is to determine whether an interaction occurs within the distance $\bar{\lambda}/n$. Toward that end the probability of such a collision $P(\bar{\lambda}/n)$ is calculated and compared to a random number ζ. If ζ is less than P, an interaction is assumed to have occurred. If $\zeta > P$, no interaction is said to have occurred and the projectile is advanced by a distance $\bar{\lambda}/n$ and the process is repeated. If there has been an interaction, it will have

[‡]Cugnon (82).

taken place at a distance from the beginning of the interval given by $\zeta/\bar{\lambda}$. At this point the direction of travel of the particle is determined from the known nucleon–nucleon angular distribution by a technique similar to that described above for deciding if an interaction has taken place, that is, the probability for scattering through a given angle randomly selected is compared with a random number. The final energies of the colliding nucleons can then be calculated. If the energy of either of the particles is below the Fermi energy, the interaction is forbidden so that the momenum of the projectile is unchanged. One now repeats the process with another Fermi-sea nucleon to see if an interaction takes place in the remainder of the interval. If the energies of both particles are above the Fermi energy, the collision is allowed. Their momenta are determined from the selected scattering angle. The process is then repeated for each nucleon. As the cascade develops, the density in the Fermi seas is reduced. Yariv and Fraenkel (79) consider two possible consequent rearrangements. In the *fast rearrangement*, the density of the target is instantaneously reduced. In the *slow arrangement* a "hole" of volume $1/\rho$ is punched around the position of the collision. No more interactions are allowed within this volume. Empirically, slow arrangement yields results that are in better agreement with experiment. The entire procedure is repeated until statistical significance is obtained.

Several features are sometimes included in the calculation. Pion production and absorption proceeding through the Δ baryon resonance is one. In another, the nucleons are assumed to be traveling in a potential well so that the nucleon paths between collisions are no longer straight lines. Collisions among the cascade particles, as well as formation of composite systems, may (or may not) be included.

In the calculations by Cugnon (81), Stevenson (78), Bondorf et al. (76), and Halbert (81), the continuum distribution for the target is dropped. Each of the nucleons on the target and projectiles is positioned randomly within spheres, representing the target and projectile nuclei. Their momenta are chosen randomly using the Fermi gas model. The projectile is given the beam velocity. The projected nucleons are assumed to move in straight lines between collisions. When the minimum relative distance is smaller than $\sqrt{\sigma_{\text{tot}}/\pi}$, the nucleons are assumed to scatter. Here σ_{tot} is the total nucleon–nucleon cross section at their center-of-mass energy. It is evident that in both of these procedures the nucleon correlations in both the target and projectile are neglected.

The motion of the nucleons in the INC simulation is classical. A necessary condition for its validity is that the cascade and projectile nucleon wavelengths are much smaller than the internucleon distance r_{12}.

$$\frac{\hbar}{p_{\text{lab}}} \ll r_{12}$$

This condition will not be met by the low-energy cascade nucleons generated by the incident projectile. The calculation of the low-energy part of the spectrum

will thus be unreliable. A second condition requires that the mean free path must be large compared to the interaction range r_c:

$$\lambda \gg r_c$$

Here r_c is defined by $\sigma_{\text{tot}} = \pi r_c^2$. Since $\lambda = 1/\rho\sigma_{\text{tot}}$, this condition becomes

$$\pi r_c^3 \rho \ll 1$$

This condition is well satisfied for normal nucleon densities. Finally, nucleon correlations are reflected in nucleon momenta which exceed the limits of the Fermi gas. As a consequence, one may expect an inability to match the data at the high-energy end of the energy spectrum. A similar remark may be made with respect to the angular distribution.

The invariant nucleon cross section is related to the calculated one-body distribution function, f_1, by

$$E\frac{d^3\sigma}{dp^3} = \lim_{t\to\infty} \int_0^{b_{\max}} 2\pi b\, db \int d\mathbf{r}\, E f_1(\mathbf{r}, \mathbf{p}, b, t) \tag{7.41}$$

An example of a comparison with experiment is shown in Fig. 7.5. The agreement is very good except for the low-energy part of the spectrum, where INC underestimates the cross section for $E < 80$ MeV. Evaporation of the residual nuclei has not been included in the calculation. The effect of including the interaction between cascade particles is small.

Another example is provided by Cugnon and Vandermulen (85) as shown in Fig. 7.6. We see that at 800 MeV/A the angular distribution is far from isotropic. This is because a considerable fraction of the proton distribution is a consequence of a single collision. As the number of collisions increase, the angular distribution will become more isotropic. For the Ca + Ca case at 800 MeV/A, isotropy is achieved for $n \lesssim 6$. The probability distribution for the number n of collisions is shown in Fig. 7.7 for the Ca + Ca collision. The mean value is 3.24. Of course, the probability for a large n is very small for peripheral collisions.

A second observable is the correlation between two protons, as given by

$$C(\mathbf{p}_1, \mathbf{p}_2) = \lim_{t\to\infty} \frac{\int 2\pi b\, db \int\int d\mathbf{r}_1\, d\mathbf{r}_2 f_2(\mathbf{r}_1, \mathbf{p}_1; \mathbf{r}_2, \mathbf{p}_2; b, t)}{\int 2\pi b\, db \int d\mathbf{r}_1 d\mathbf{p}_1 f_1(\mathbf{r}_1, \mathbf{p}_1; b, t)} \tag{7.42}$$

where f_2 is the two-body distribution function. In the Nagamiya et al. (79) experiment, the correlation between a proton emitted at a "telescope" angle and an second particle in the angular range $35° < \theta < 45°$ is studied. The ratio C is defined to be the ratio of such in the scattering plane correlations for the azimuthal angle $\phi = 180° \pm \Delta\phi (\Delta\phi = 10°)$, to the out-of-plane correlations

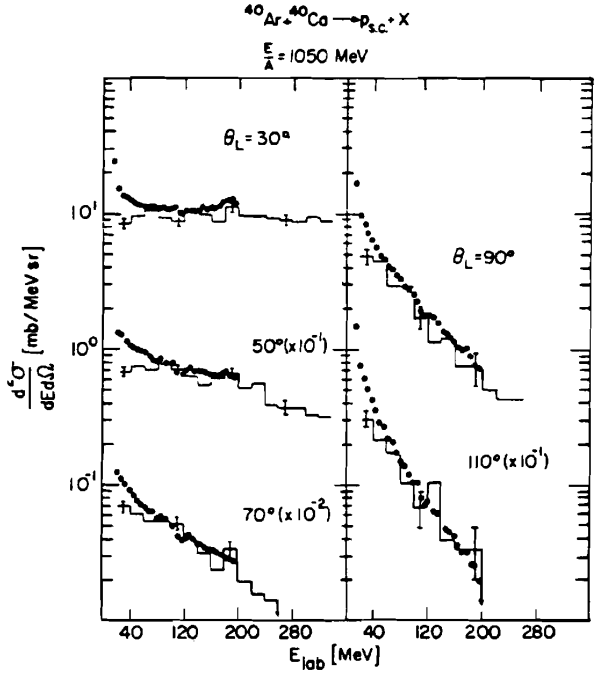

FIG. 7.5. Inclusive double-differential cross section for the emission of nucleon charges in the reaction $^{40}Ar + ^{40}Ca$ at a bombarding energy of $E/A = 1050$ MeV. The histograms show the calculated results, includeing the effects of interaction between the cascade particles. [From Yariv and Fraenkel (81).]

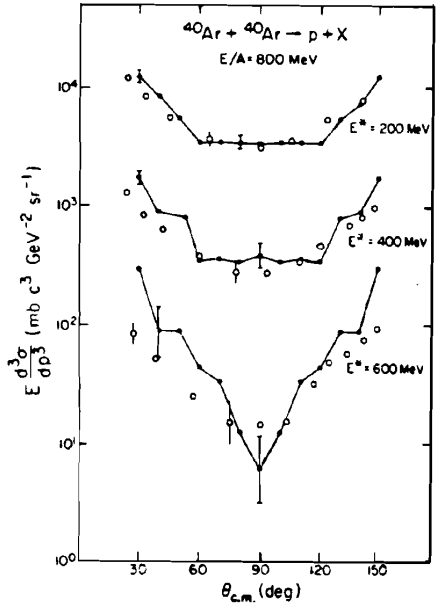

FIG. 7.6. Invariant inclusive proton cross section as a function of the center-of-mass angle for the $^{40}Ar + ^{40}Ar$ system at 800 MeV/nucleon. [From Cugnon and Vandermuelen (85).]

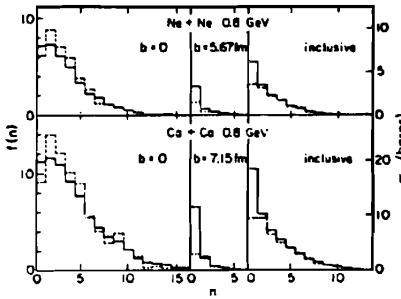

FIG. 7.7. Probability distribution for the number n of collisions that the particles have undergone. The full lines refer to the nucleons. Left, zero impact parameter; center, large impact parameter; right, average overall impact parameters. [From Cugnon and Vandermuelen (85).]

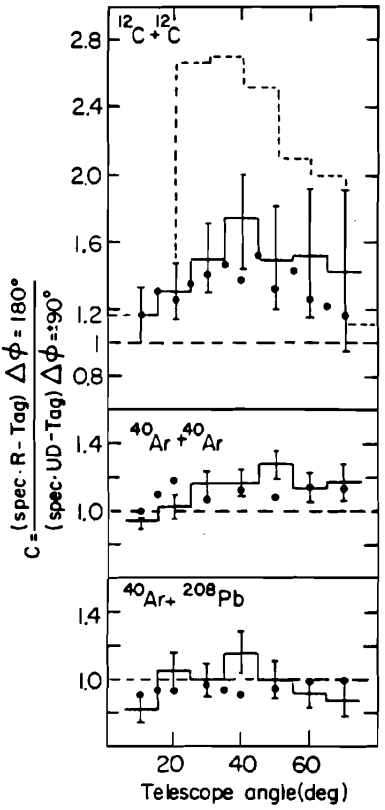

FIG. 7.8. Ratio, C, of "in-plane" ($\Delta\phi = 180°$) to "out-of-plane" ($\Delta\phi = \pm 90°$) tow-particle correlations as a function of the polar (telescope angle). The second particle is detected at a polar angle of $10 \pm 5°$, $\Delta\phi$ is the difference in the azimuthal angle of the two particles. The histograms are calculated. The solid-line ones include the effects of interaction betweeen the cascade particles, the dashed-line ones do not. [From Yariv and Fraenkel (81).]

($\phi = \pm 90° + \Delta\phi$). The results of the INC calculation and a comparison with experiment are shown in Fig. 7.8. The calculated results *when the interaction between cascade particles is included* are in good agreement with experiment. The ratio C is close to unity (except for the $^{12}C + {}^{12}C$ collision), indicating a degree of thermalization.

Other observables include the momentum tensor $Q_{\mu\nu}$ and the related quantity

the thrust, T. For an event, $Q_{\mu\nu}$ is given by

$$Q_{\mu\nu} = \sum_i \gamma(p_i) p_i^\mu p_i^\nu \tag{7.43}$$

where i runs over the fragments and μ, ν designate the Cartesian coordinates. The weights $\gamma(p_i)$ are to be chosen. When $\gamma(p_i)$ is taken to be $1/A_i$, where A_i is the mass number of the fragment, the resultant $Q_{\mu\nu}$ is independent of the degree of clusterization.

The thrust, T, is given by

$$T = \min_{\mathbf{n}} \frac{\sum |\mathbf{p}_i \cdot \mathbf{n}|}{\sum |\mathbf{p}_i|} \tag{7.44}$$

where the unit vector $\mathbf{n}$ is chosen to as to minimize this ratio. The direction of the thrust is given by $\mathbf{n}$. The values for the thrust angle (the calculated thrust lies in the reaction plane for collisions between equal nuclei) are given in Fig. 7.9 as calculated by INC [Bertsch and Cugnon (81)] and using hydrodynamics [Kapusta and Strottman (81)]. As expected, the INC calculation predicts a flow that is much more in the forward direction. Experimental indications of collective flow is given in the paper by Gustafson, Gutbrod, et al. (84). In Fig. 7.10 the frequency distribution $dN/d\cos\theta$ as a function of flow angle θ is plotted for various multiplicities for reactions involving heavy ions at 400 MeV/A. The flow angle is defined as the angle between the beam direction and the major axis of the ellipsoid given by $Q_{\mu\nu}$ of (7.43), with weights $\gamma(p_i) = 1/2A_i$, where A_i is the mass of the fragment. We observe that as the multiplicity increases (impact parameter decreases), the frequency distribution has a maximum at a finite angle, while the INC calculations have their maxima at 0°. The parallel component of the projectile momentum is reduced during the collision, and the momentum acquires a small perpendicular momentum on the order of 50 MeV/c. The origin of this discrepancy is not yet clear. Is it because of the approximation (e.g., the Fermi-gas description of the colliding nuclei) of the INC procedure, or is it because of the omission of collective modes of motion by the INC? For a recent discussion, see Aichelin, Cugnon, et al. (89).

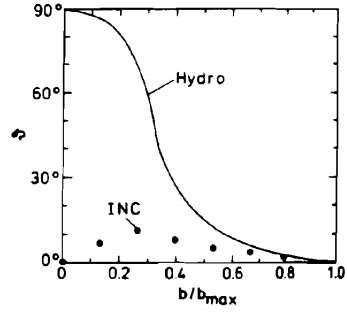

FIG. 7.9. Thrust angle as given by a hydrodynamic calculation (full line) and by the inter nuclear cascade (dots). [From Cugnon (82).]

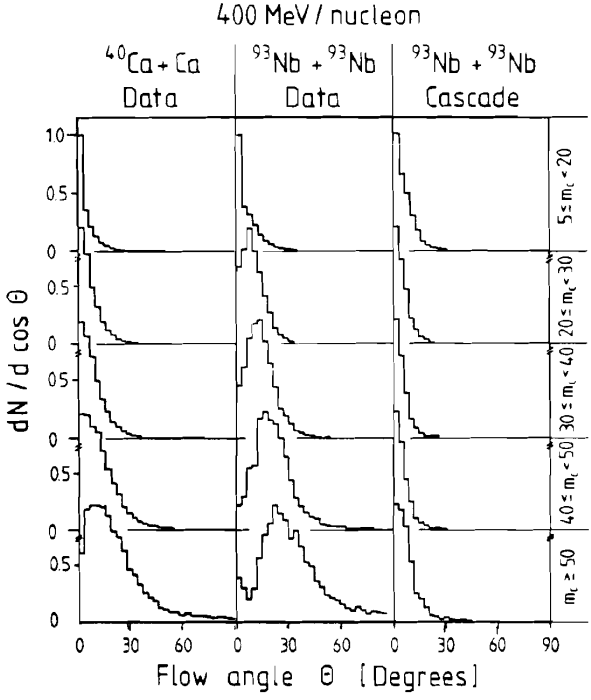

FIG. 7.10. Frequency distributions of the flow angle θ for two sets of data and a cascade calculation for different multiplicity bins. For the case of Ca the multiplicities are half the indicated values. [From Gustafsson, Gutbrod, et al. (84).]

8. COLLISIONS AT ULTRARELATIVISTIC ENERGIES

In this section the collision of ultrarelativistic projectiles, with energies greater than several GeV/nucleon, with nucleon is briefly considered. Experiments in which the projectile has an energy of up to several hundred GeV have been reported. This field is in its infancy. There are many results that are still not understood and much more experimentation and theoretical studies are needed.

A. Lorentz Transformation

In the relativistic regime, the Lorentz transformation is especially important. The Lorentz transformation to a frame moving with a velocity v (*we shall use units in which the velocity of light, c, is unity*) in the position z direction is [Morse and Feshbach (53 p. 94)]

$$z' = z\cosh\xi + t\sinh\xi$$
$$t' = z\sinh\xi + t\cosh\xi \tag{8.1}$$

where

$$\cosh \xi \equiv \frac{1}{\sqrt{1-v^2}} \qquad \sinh \xi = \frac{v}{\sqrt{1-v^2}} \qquad \xi = \frac{1}{2} \ln \frac{1+v}{1-v}. \tag{8.2}$$

Under a second boost with velocity v',

$$z'' = z' \cosh \xi' + t' \sinh \xi'$$
$$t'' = z' \sinh \xi' + t' \cosh \xi'$$

Substituting from (8.1) for z' and t', one finds, for example,

$$z'' = z \cosh(\xi + \xi') + t \sinh(\xi + \xi')$$

Thus the effect of two sequential boosts of v and v' can be obtained by addition of the corresponding ξ parameters.

This result is even more apparent if one introduces the *light cone variables*,

$$z_+ \equiv x + t \qquad z_- = x - t \tag{8.3}$$

Under a Lorentz transformation,

$$z'_+ = e^{\xi} z_+ \qquad z'_- = e^{-\xi} z_- \tag{8.4}$$

Finally, the trajectory of a free particle

$$z - ut = 0$$

can be written in terms of the light cone variables as

$$z_- = -\frac{1-u}{1+u} z_+ = -e^{-2\mu} z_+ \tag{8.5}$$

where

$$\mu = \frac{1}{2} \ln \frac{1+u}{1-u}$$

If we consider the motion in a moving frame of velocity v, (8.5) becomes

$$z'_- = -e^{-2(\mu - \xi)} z'_+ \tag{8.6}$$

B. Rapidity

Suppose that we have a particle of mass M_p and total energy (including rest mass) E_L incident on a target of mass M_T at rest. In the zero-momentum frame,

inaccurately referred to as the center-of-mass frame, the total energy $\sqrt{s}$, that is, the energy of the projectile and the target, is given by

$$s = 2E_L M_T + M_T^2 + M_P^2 \tag{8.7}$$

If E_L is sufficiently large,

$$\sqrt{s} \simeq \sqrt{2E_L M_T} \tag{8.8}$$

The result that the energy in the center-of-mass frame increases as the square root of the energy in the laboratory frame has led to the development of accelerators in which beams of opposite momenta collide.

The kinematics of the collisions can be treated most expeditiously through use of the rapidity variable, y, defined by [compare with (8.3)]

$$\begin{aligned} E + p_\parallel &= \mu e^y & E - p_\parallel &= \mu e^{-y} \\ E &= \mu \cosh y & p_\parallel &= \mu \sinh y \end{aligned} \tag{8.9}$$

The quantity $p_\parallel$ is the component of the momentum in the z direction. To obtain μ, note that $(E + p_\parallel)(E - p_\parallel) = \mu^2 = E^2 - p_\parallel^2 = m^2 + p_\perp^2$, where $p_\perp^2$ is the *transverse momentum*

$$p_\perp^2 = p^2 - p_\parallel^2$$

Therefore,

$$\mu = \sqrt{m^2 + p_\perp^2} \tag{8.10}$$

and μ is referred to as the *transverse mass*. From (8.9) one finds that

$$y = \frac{1}{2} \ln \frac{E + p_\parallel}{E - p_\parallel} = \ln \frac{E + p_\parallel}{\mu} \tag{8.11}$$

Under a Lorentz transformation in the z direction

$$\begin{aligned} p' &= p_\parallel \cosh \xi + E \sinh \xi \\ E' &= p_\parallel \sinh \xi + E \cosh \xi \end{aligned}$$

or

$$\begin{aligned} E' + p'_\parallel &= e^\xi (E + p) = \mu e^{(\xi + y)} \\ E' - p'_\parallel &= e^{-\xi} (E - p) = \mu e^{-(\xi + y)} \end{aligned}$$

Therefore, the rapidity in the new frame, y', is

$$y' = \xi + y \tag{8.12}$$

As a consequence, rapidity difference are invariant with respect to boosts in the z direction:

$$y'_2 - y'_1 = (y_2 + \xi) - (y_1 + \xi) = y_2 - y_1 \tag{8.13}$$

As an example, let us use these results to describe the transformation to the center of mass when a proton of energy E_L and momentum p_L is incident on a proton at rest. The center-of-mass system is defined as one in which the protons have equal but opposite momenta. We therefore require that

$$p'_{\text{cm}} = m \sinh(y - \xi) = m \sinh \xi$$

Therefore,

$$\xi = \frac{y}{2} \tag{8.14}$$

The total energy is then given by

$$\sqrt{s} = E = 2m \cosh \frac{y}{2} \tag{8.15}$$

and

$$s = 4m^2 \cosh^2 \frac{y}{2} = 2m^2(1 + \cosh y) = 2m(m + E_L) \tag{8.16}$$

which agrees with (8.7) for $M_T = M_L = m$.

The Lorentz invariant phase space volume $d\mathbf{p}/E$ has a simple form when expressed in terms of y:

$$\frac{d\mathbf{p}}{E} = d\mathbf{p}_\perp \frac{dp_\parallel}{E} = d\mathbf{p}_\perp \frac{\mu \cosh y \, dy}{E}$$

$$= d\mathbf{p}_\perp dy \tag{8.17}$$

The Lorentz invariant cross section is is thus

$$\frac{E \, d\sigma}{d\mathbf{p}} = \frac{d\sigma}{d\mathbf{p}_\perp dy} \tag{8.18}$$

In the laboratory frame the projectile will initially have a momentum $p = p_\parallel$, $p_\perp = 0$, while the target's initial momentum is zero. The corresponding rapidities in the limit in which the masses are very much smaller than the corresponding energies are

$$y_T = 0 \qquad y_P = \ln \frac{2p_L}{M_P}$$

In the center-of-mass frame,

$$y_T = -\frac{1}{2}\ln\frac{2p_L}{M_T} \qquad y_P = \frac{1}{2}\ln\frac{2M_T p_L}{M_P^2}$$

In the frame in which the projectile is at rest and the target is in motion

$$y_T = -\ln\frac{2p_L}{M_P} \qquad y_P = 0$$

It is often the case that measurements yield only the angle with respect to the incident direction, ϑ, along which a secondary particle is traveling. The relation of that angle with y will now be obtained. Consider the quantity

$$\frac{E - p_\parallel}{p_\perp} = \frac{\mu e^{-y}}{p_\perp}$$

The left-hand side of this equation can be written

$$\frac{1}{p_\perp}(\sqrt{p^2 + m^2} - p_\parallel) \simeq \frac{1}{p_\perp}\left(p - p_\parallel + \frac{1}{2}\frac{m^2}{p}\right)$$

The right-hand side to the same order is

$$\frac{1}{p_\perp}\sqrt{m^2 + p_\perp^2}\, e^{-y} \simeq e^{-y}\left(1 + \frac{1}{2}\frac{m^2}{p_\perp^2}\right)$$

Collecting terms and using $p_\parallel/p = \cos\vartheta$ and $p_\perp/p = \sin\vartheta$ yields

$$y \simeq -\ln\tan\frac{\vartheta}{2} + \frac{m^2}{p_\perp^2}\cos\vartheta \tag{8.19}$$

The pseudo-rapidity η is defined to be

$$\eta \equiv -\ln\tan\frac{\vartheta}{2} \tag{8.20}$$

The quantity η approximates y if $m^2/p_\perp^2$ is sufficiently small. The error is large for soft collisions when the secondary particles is a proton.

The rapidity, y, depends only upon the longitudinal velocity:

$$y = \frac{1}{2}\ln\frac{1 + v_\parallel}{1 - v_\parallel} \tag{8.21}$$

where

$$v_{\parallel} = \frac{p_{\parallel}}{E}$$

A change in y by 1 *unit* corresponds to a change in $v_{\parallel}$, for $v_{\parallel} \sim 1$, of

$$\delta v_{\parallel} = 6.4(1 - v_{\parallel}) \tag{8.22}$$

In a reaction, the peripheral collision will result in the fragmentation of the projectile (even if it is a proton!). The fragments will be traveling with approximately the same velocity as the projectile; that is, they will acquire relatively little transverse momentum. Experimentally, $\langle p_{\perp} \rangle \lesssim 350\,\text{MeV}/c$ (see the later discussion). The target will also fragment, contributing to the particle distribution for y close to the target rapidity. The region in y to which the proton fragmentation makes a contribution is experimentally on the order of 2 units, as ascertained from p–p ISR experiments at CERN. The corresponding Δy for nuclear fragmentation is on the order of 3 units. A clear separation of the fragments occurs only at sufficiently high energy. If, for example, the projectile is a 15-GeV proton, the value of y for the projectile is only 3.47. In this case the two contributions from target and projectile will overlap. When the energy is 200 GeV, the projectile y is 6.06, so that a central region which is a consequence of a more central collision will be visible.

C. Proton–Nucleus Collisions[‡]

A complete understanding of the interaction of multi-GeV protons with nuclei is very far from being achieved. The experimental attack on the problem is for the most part just beginning. Similarly, the theoretical concepts required still remain to be identified. However, a few features have emerged. These will be the subject of this subsection.

Before proceeding to this task, it would be useful to note two characteristics of the proton–proton collisions. The first is the multiplicity plotted in Fig. 8.1. We note that the multiplicity rises slowly with beam momentum, rising from about 3 at 20 GeV/c to about 10 at 10^3 GeV/c. Most of the particles observed are charged pions of both signs. To get the total multiplicity, including the neutral pions, one must multiply the charged pion multiplicity by $\frac{3}{2}$.

The second point of interest is the transverse momentum of the protons and pions produced in a p–p collision. The average value $\langle p_T \rangle$ of pions is shown in Fig. 8.2 as a function of rapidity. The $p + p \to \pi + X$ channel is the principal inelastic channel. The maximum transverse momentum of the pions produced in the reaction is about 350 MeV/c. More than one pion is produced, as one can see from Fig. 8.1. At $p = 100\,\text{GeV}/c$, the number of charged particles is

[‡]Busza and R. Ledoux (88); McCubbin (88); J. Hüfner and Klar (84); Klar and Hüfner (85).

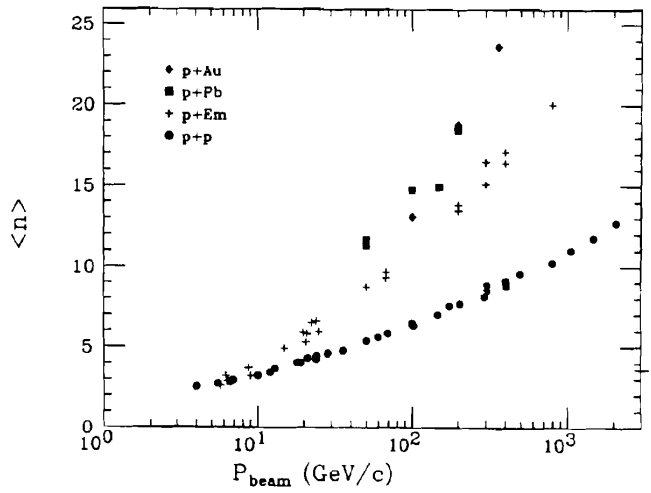

FIG. 8.1. The mean number of charged particles ($\langle n \rangle$) as a function of beam momentum. Em refers to an emulsion target. [From Busza and Ledoux (88).]

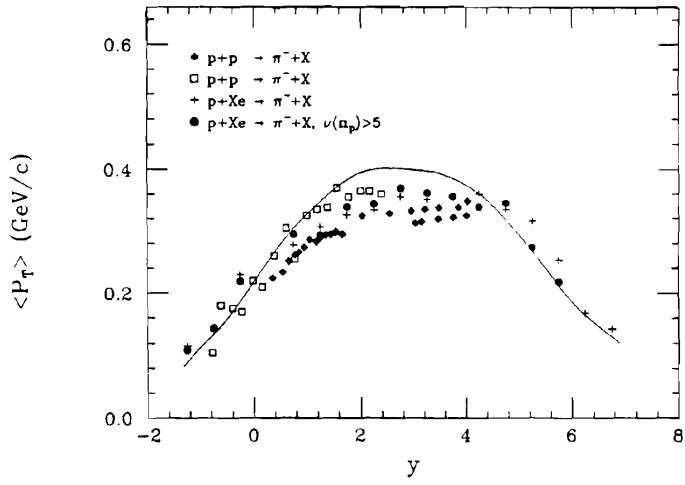

FIG. 8.2. The $\langle p_T \rangle$ of π^- as a function of y for $p + p$ and $p + \mathrm{Xe}$ collisions. [From Busza and Ledoux (88).]

6.37 ± 0.05, $v > 0.7$. These are thought to be mostly charged pions. To include π^0, we multiply the charged particle multiplicity by $\frac{3}{2}$ to obtain 9.6. Taking the mass of each pion to be 137 MeV with a momentum of 350 MeV/c (see Fig. 8.2), assuming that the angular distribution is roughly isotropic in the center-of-mass reference frame yields an average energy per pion of 376 MeV. The total excitation energy of the radiating projectile proton in the proton–proton center

of mass is 0.376 × (9.6) or 3.6 GeV at $p_L = 100\,\text{GeV}/c$ (or $E_{\text{cm}} = \frac{1}{2}\sqrt{s} = 6.9\,\text{GeV}$). More than one-half of the available kinetic energy is converted into nucleon excitation. The excited nucleon has total energy of 4.5 GeV.

For the most part, $p + p$ collisions are "soft." "Hard" collisions involve pion momenta much beyond 400 MeV/c. For these cases involving a close collision, one may expect hadron jets to be produced. However, the probability for such close collisions is relatively low, as one can see from Fig. 8.3.

What happens when a proton strikes a nucleus? Naively (and incorrectly), one might believe that the proton strikes several nucleons, producing about 10 relatively energetic pions in the target frame of reference per collision. These pions would also generate secondaries, and so on. On this basis one would expect a very large number of emerging charged particles per incident proton. Table 8.1 and Fig. 8.4, where the multiplicity of charged particles with $v > 0.7$ is tabulated, demonstrate that this is very far from the truth. Multiplicities are small, rising to a factor of about 2.5 for U relative to the multiplicity for a p–p collision. Note that the same result holds when the incident hadron is a kaon or a pion. Parenthetically, the variable $\bar{\nu}$ is defined as the average thickness of a nucleus in units of the mean free path (Fig. 8.4) for absorption of the incident proton:

$$\bar{\nu} = \frac{A\sigma_{\text{inel}}(p + \text{nucleon})}{\sigma_{\text{inel}}(p + \text{nucleus})} \tag{8.23}$$

Empirically, $\bar{\nu} = 0.7A^{0.31}$ for protons and $0.74A^{0.25}$ for pions. The variable $\bar{\nu}$ is a rough measure of the number of collisions made by the indicated hadron

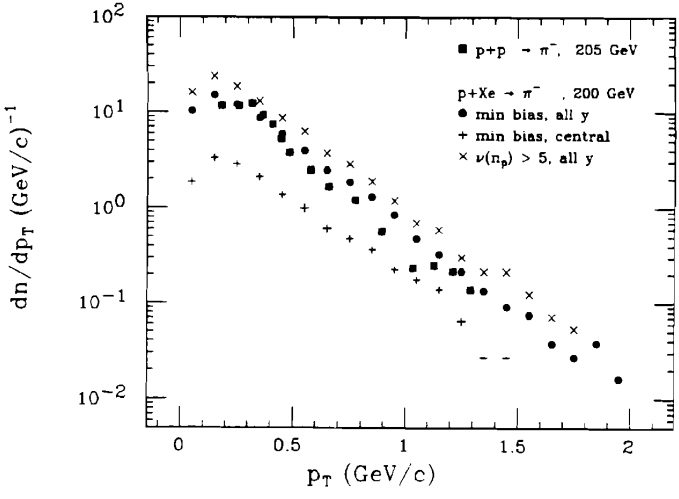

FIG. 8.3. The π^- transverse momentum distributions from $p + p$ and $p + \text{Xe}$ collisions. [From Busza and Ledoux (88).]

TABLE 8.1 Average Multiplicities of Relative Charged Particles Produced in 100-GeV/c Hadron–Nucleon Collisions

Target	Projectile	Average Multiplicity
C	π^+	7.86 ± 0.15
	K^+	6.92 ± 0.33
	p	7.72 ± 0.16
Cu	π^+	10.29 ± 0.26
	K^+	8.89 ± 1.10
	p	11.00 ± 0.32
Pb	π^+	13.21 ± 0.30
	K^+	12.92 ± 0.79
	p	14.75 ± 0.38
U	π^+	14.57 ± 0.39
	K^+	12.93 ± 1.33
	p	15.94 ± 0.50
Hydrogen (bubble chamber)	π^+	6.62 ± 0.07
	K^+	6.65 ± 0.31
	p	6.37 ± 0.06

Source: Elias, Busza, et al. (78).

in passing through the nucleus. As one can see from Fig. 8.4 for small laboratory angles, the ratio to hydrogen is unity for all elements. If one extends the laboratory angle to 100°, the ratio rises to values of less than 2. In Fig. 8.5 we show the ratio of the multiplicity in pA collisions to that in p–p collisions for 100-GeV/c protons. The ratio is a linear function ν:

$$\frac{\langle n_a \rangle}{\langle n_p \rangle} = 1 + 0.3(\nu - 1) \tag{8.24}$$

The absence of cascading can be understood as a relativistic effect [Goldhaber (74a)]. The incident proton on striking a nucleon of the target nucleus will form an excited system. Because of the relativistic time dilation its lifetime will be very much longer than its rest-frame lifetime, which is of the order of 1 fm/c. In fact, as we shall see, the mean distance it would travel before decaying is very much larger than the nuclear radius. It therefore will not decay before its collision with a second nucleon. This collision will change its excitation energy somewhat. This process continues until the proton leaves the nucleus and then decays. Cascading induced by the decay of the excited nucleon thus does not occur.

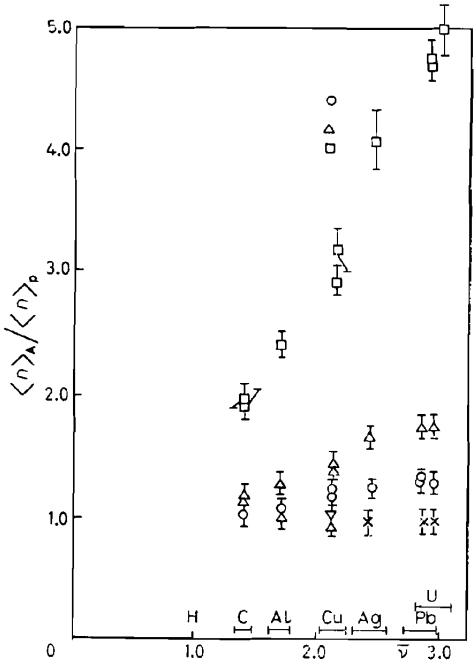

FIG. 8.4. Angular dependence of the ratio of the multiplicity for the indicated target nuclei with the multiplicity for a hydrogen target: × $0° < \theta_{lab} < 3.5°$, ○ $0° < \theta_{lab} < 26°$, △ $0° < \theta_{lab} < 110°$, □ $26° < \theta_{lab} < 110°$; MIT π–A data. [From Elias, Busza, et al. (78); Elias et al. (80).]

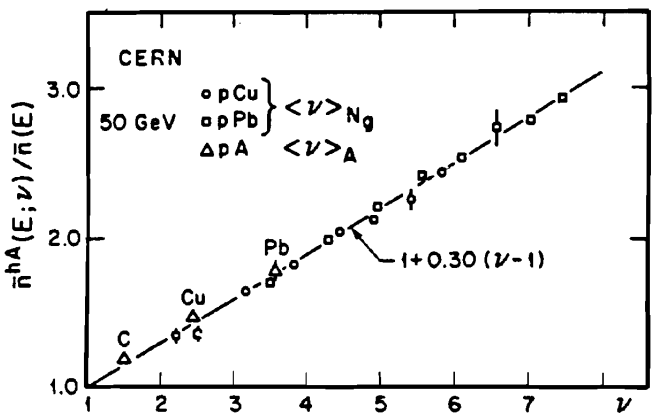

FIG. 8.5. Ratio of the multiplicity of produced particles in pA collisions divided by the multiplicity in pp collisions as a function of $\bar{\nu}$ and $\bar{\nu}(n_p)$. [From Ledoux, Bloomer, and Huang (86).]

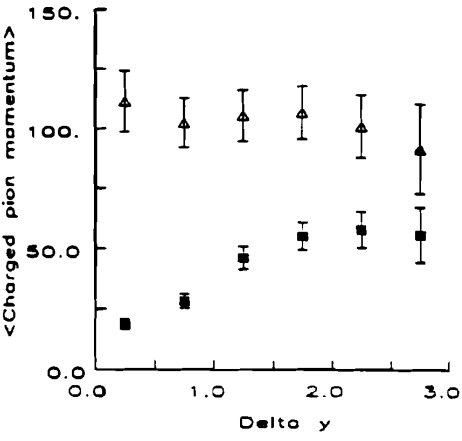

FIG. 8.6. Results from the reactions $p + A$ and $\bar{p} + A$ at 100 GeV/c, showing the momentum (in GeV/c) of charged pions (■) and the total momentum of the leading baryon plus 1.5 times the charged pion momentum (Δ). [From Busza and Ledoux (88).]

Let us look at this process in more detail. We make use of three experimental facts. The first is that in a proton–proton collision the incident proton in the rest frame loses 2 units of rapidity [Busza and Ledoux (88)]. The rapidity of a 100-GeV proton is 5.362, so that after the collision $y - 2 = 3.362$, corresponding to an energy loss of 86%. Second, as we have seen (Table 8.1), the numbers of charged pions emitted is 6.37. This is to be multiplied by 1.5 to take the neutral pion production into account, yielding 9.56 as the number of pions. Moreover, the secondaries produced by the proton fragmentation are mostly pions, as demonstrated by Fig. 8.6. The energy loss of the proton consists of the energies of these pions and the recoil energy transmitted to the target nucleon plus the pions emitted by it. We shall assume that the recoil energy is about 3.5% (this can be checked later and a correction calculated). Hence the energy per pion is 7.64 GeV, where the target nucleon pions have been assigned an energy of 1 GeV per pion. Finally, we recall that the average transverse pion momentum is 350 MeV/c, so that its transverse mass is 0.377 GeV.

Let a pion in the center-of-mass system have a rapidity σ. Note that proton and target nucleon have a rapidity of $y/2$ and $-y/2$, respectively, where $y = 5.362$. Then the pion energy, including the proton pion and a target nucleon pion energy in the laboratory frame, is

$$8.64 = \mu\left[\cosh\left(\sigma + \frac{y}{2}\right) + \cosh\left(\sigma - \frac{y}{2}\right)\right]$$

$$= 2\mu \cosh\sigma \cosh\frac{y}{2} \tag{8.25}$$

In this equation μ is the pion transverse mass. From (8.25) we find that

$$\sigma = 1.016 \tag{8.26}$$

The projectile pion rapidity in the laboratory frame is $y/2 + \sigma = 3.7$, close to rapidity of the final proton, 3.362. Its energy is 7.61 GeV. The target pion rapidity is $y/2 - \sigma = 1.66$, with an energy of 1.03 GeV. The corresponding longitudinal momenta are 7.60 GeV/c and 0.96 GeV. Since the transverse momentum is 0.350 GeV/c, the target nucleon pions are emitted at an average angle of 20°. They will thus not make a very significant contribution to the forward angle pion multiplicity but will affect the larger angle contributions. Finally, we calculate the difference in the velocities of the projectile pions and the nucleon assigning a rapidity of 3.362 to the proton and 3.7 to the pion.

$$v_p - v_\pi \equiv \delta v \simeq 2e^{-2y_p}(1 - e^{-2(y_\pi - y_p)}) = 1.2 \times 10^{-3}$$

In traveling the distance of a nuclear radius R, the separation of the projectile nucleon and the projectile pions will be $\delta v \times R$, which for a nucleus of radius of 6 fm is 7.2×10^{-16} fm. In order words, the pions will be "inside" the proton projectile. Thus the pions will not separate from projectile proton until the system is far outside the nucleus. The effect of only the first collision has been considered, but it is clear that subsequent collisions will not affect this result.

We have assumed that the system is on the energy shell after the collision and before the second collision. This is not at all obvious. If it is not, one must treat the collision with all the nucleons in the path of the projectile. A simple nonrelativistic calculation [Feshbach (83)] shows that this effect will not change the results above (i.e., the decay outside the nucleus), but there can be substantial quantitative differences. A more sophisticated theory has been published by Gottfried (74b), which yields (8.19) with the $\frac{1}{3}$ factor.

Empirically, the loss of rapidity of the projectile in colliding with a nucleus is of the order of 3 units [Busza and Ledoux (88)], so that a 1200-GeV proton has a final energy of 5 GeV. Most of that loss of energy is in pions emitted outside the nucleus. Most of the very energetic pions are generated by the first collision.

Another outstanding feature of the proton–nucleus interaction is the energy independence of the rapidity distributions in the target and projectile fragmentation regions. This is illustrated in Figs. 8.7 and 8.8. There are emulsion data, so that the target nuclei are Ag and Br. "Shower particles" correspond to single charged relativistic secondaries ($\beta > 0.7$). The incident protons have energies of 200, 400, and 800 GeV. The explanation is straightforward. As we have just described, most of these secondaries are generated in the first proton–nucleon collision (see Table 8.1). Combine this with the experimental result that such energy independence is observed in proton–proton collisions and we have the result of energy independence for proton–nucleus collisions. This behavior is referred to as *limiting fragmentation.* It is interesting to note that the projectile fragmentation in nucleus–nucleus collisions at a few GeV/A discussed in Section 7 is also energy independent.

One final comment is suggested by the rapidity distributions for different targets as shown in Fig. 8.9. We see a strong target dependence. Let $dn/d\eta \sim A^{\alpha}(\eta)$. From the data one finds $\alpha(\eta) > 0.3$ for $\eta \leqq 1.5$ [Elias *et al.* (80)]. Second,

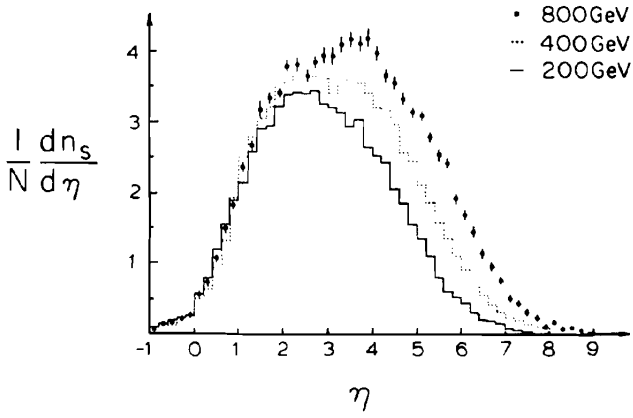

FIG. 8.7. Inclusive pseudorapidity distribution of shower particles in the laboratory frame at 200, 400, and 800 GeV. [From Abduzhamilov et al. (87).]

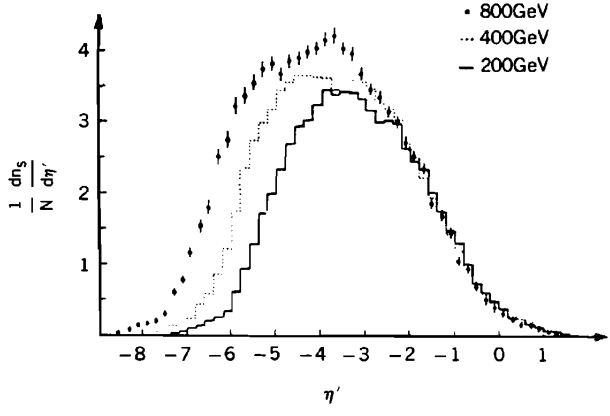

FIG. 8.8. Inclusive pseudorapidity distribution of shower particles in the projectile rest frame at 200, 400, and 800 GeV. [From Abduzhamilov et al. (87).]

we note that

$$\frac{dn}{d\eta} = \frac{1}{\sigma_{\text{inel}}}\frac{d\sigma}{d\eta} \tag{8.27}$$

where σ is the cross section for producing n secondaries. Since $\sigma_{\text{inel}} \sim A^{0.7}$,

$$\frac{d\sigma}{d\eta} = A^{0.7+\alpha}$$

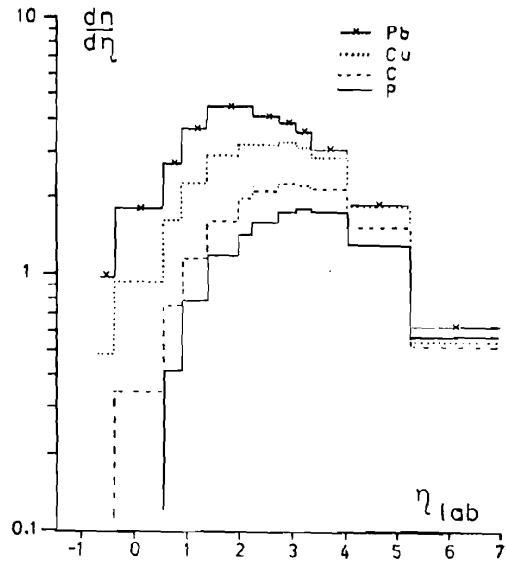

FIG. 8.9. $dn/d\eta$ versus η at 200 GeV on four different targets. [From McCubbin (89).]

The exponent is greater than unity, which indicates the presence of multiple scattering with associated cascading. The effect of such multiple scattering is larger for the larger nuclei.

D. Nucleus–Nucleus Collision[‡]

Interest in the collision of ultrarelativistic particles (protons and nuclei) has been motivated by the prediction of QCD (quantum chromodynamics) lattice gauge calculations that a quark–gluon plasma will be formed when the temperature of nuclear matter exceeds roughly 200 MeV. Above that temperature nuclear matter "melts" into quarks and gluons. More accurately, there is a combination of density and temperature at which such a transition occurs, as illustrated in Fig. 8.10. It is hoped that such densities and temperatures can be obtained through the collision of very energetic nuclei. Experiments are now being conducted at BNL (~ 15 GeV/A) and at CERN (~ 200 GeV/A) with fixed targets and beams as heavy as Si. BNL will soon be able to provide Au beams and CERN is planning a Pb injector. For the more distant future, a collider, RHIC (relativistic heavy ion collider), providing 100-GeV/A beams, has been proposed by BNL. The study of a new form of matter, the quark–gluon plasma, would not only test QCD but it would be of great importance for cosmology as well. Soon after the "big bang," before hadronization, the matter in the

[‡]Satz (88).

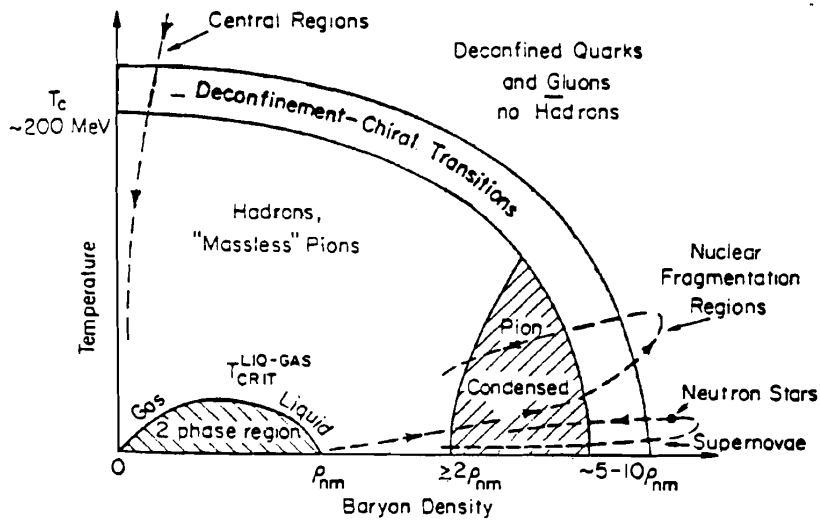

FIG. 8.10. Phase diagram of nuclear matter in the baryon density, temperature plane showing regions of hadronic and deconfined matter. Normal nuclear matter density ρ_{nm} is $0.16\,\mathrm{fm}^{-3}$. [From Baym (87).]

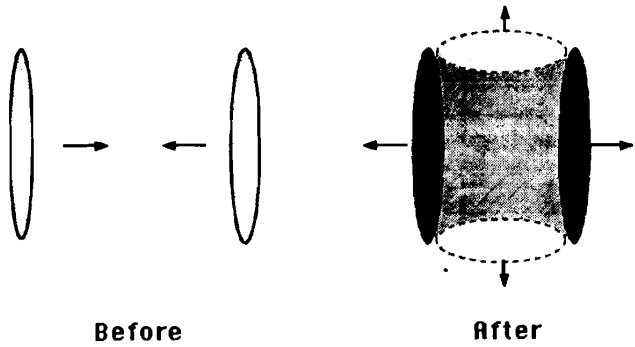

FIG. 8.11. Collision of two nuclei with relativistic energies. [From Matsui (88).]

universe would form a quark–gluon plasma, which as the universe cools would condense into nucleons and nuclei.

The collision of two nuclei is pictured as follows. In the center-of-mass system, because of the Lorentz contraction, the nuclei will be disks approaching each other at a velocity close to the velocity of light. As they pass through each other, energy will be deposited in each of the nuclei as a consequence of nucleon–nucleon collisions. In addition, the volume between the nuclei will contain mostly pions and will be for the most part baryon free (see Fig. 8.11). Each of these domains, the baryon-rich nuclear volumes or the baryon-free one, is a candidate for the formation of the quark–gluon plasma. The questions, whose

answer is uncertain, include: Are the density and the temperature big enough, and will that condition last for a long enough time? Will enough energy be deposited in either domain to raise the temperature to a large enough value?

The formulations of a reaction theory that describes the collision and development of the quark–gluon plasma and its equilibration is a major challenge to the theorists. One badly needs accurate evaluations of the phenomena which would signal the formation of the plasma. Several such phenomena have been proposed, such as the anomalous K/π ratio relative to its value in p–p collisions and the suppression of the formation of J/ψ particles. For an introductory review of the present situation, see Matsui (88).